Quasioptical Imaging Systems at THz Frequencies

Quasioptical Imaging Systems at THz Frequencies

PROEFSCHRIFT

ter verkrijging van de graad van doctor
aan de Technische Universiteit Delft,
op gezag van de Rector Magnificus, Prof. Ir. K.Ch.A.M. Luyben,
voorzitter van het College voor Promoties,
in het openbaar te verdedigen op
vrijdag 12 juni 2015 om 12.30 uur

door

Beatriz Blázquez Valles

geboren te Madrid, Spanje

This dissertation has been approved by:

Promotor: Prof. dr. A. Neto
Copromotor: Dr. N. Llombart Juan

Composition of the doctoral committee:

Rector Magnificus,	Chairman
Prof. dr. A. Neto,	Promotor
Dr. N. Llombart Juan,	Copromotor

Independent members:

Prof. dr. A. Garcia Pino,	University of Vigo, Spain
Prof. S. Maci,	University of Siena, Italy
Prof. dr. O. Yarovoy,	Delft University of Technology, Netherlands
Prof. dr. G. Gerini,	Eindhoven University of Technology, Netherlands
Dr. ir. J.J.A. Baselmans,	SRON Netherlands Institute for Space Research, Netherlands

Substitute member:

Prof. dr. ir. G.J.T. Leus,	Delft University of Technology, Netherlands

Foreword

This thesis is the result from two working periods in two different universities in Spain and the Netherlands.

The initial period, from April 2011 to September 2012, was developed at Universidad Complutense de Madrid, in Spain. The supervisor during this period was Nuria Llombart. The work done during these months was co-financed by two projects, a first one funded by the Spanish Ministry of Science and Innovation, “Study of advanced mechanisms for the coupling of far infrared radiation with superconducting detectors for the instrument SAFARI/SPICA”, and a second project funded by JPL/NASA, USA, “Optical system design of a time-delay multiplexed two-pixel and zoomed Terahertz imaging radar”. In both projects, Nuria Llombart was the principal investigator.

The second period of this thesis, from October 2012 to February 2015, was carried out at Delft University of Technology, in the Netherlands. The work was co-guided by Prof. Andrea Neto and Nuria Llombart. It has been supported by a collaborative project, SPACEKIDs “Kinetic Inductance Detectors: A new imaging technology for observations in and from space”, funded via grant 313320 provided by the European Commission under Theme SPA.2012.2.2-01 of Framework Programme 7.

Summary

The Terahertz gap is the portion of the spectrum lying between 300 GHz and 3 THz. The initial development of Terahertz technology was driven by Space-based instruments for astrophysics, planetary, cometary and Earth science. However, in recent years, the interest of Terahertz science has been rapidly expanded due to the emergence of new applications as secure screening of concealed weapons for military and civil purposes, biological screening, medical imaging, industrial process control and communication technology, to mention some of them. A common characteristic of THz systems is that all of them use quasioptical elements to focus the beams and achieve sufficient signal-to-noise ratios.

This doctoral thesis has focus on the analysis and development of quasioptical systems for two different types of THz applications: direct detection for space and heterodyne imaging for security. In the first part, THz absorbers-based detectors for space applications are studied. As this type of detectors can only be studied in reception, their analysis, when located under focusing systems, is usually done by full wave simulations under normal incidence illumination. This method does not describe well the actual coupling to the focusing element when the F/D ratio of the system is relatively small. An spectral model based on Fourier optics has been developed for an accurate and efficient analysis of linear absorbers under THz focusing systems for both small and large F/D ratios. The second part of this thesis is devoted to the optical system of a THz imaging radar for security screening. The goal in this part was to provide an existing THz imaging radar with new capabilities by using quasioptical solutions that do not modify the scanning mechanism and the back-end electronics. On one hand, the radar has been provided with an all-quasioptical waveguide that performs time-delay multiplexing of the beams, reducing the image acquisition time a factor of two by only adding some extra optical elements to the system. Furthermore, the feasibility of this technique to be applied to large linear arrays of transceivers is proven. On the other hand, the radar was provided with refocusing capabilities by implementing the classical optical solution of translating the transceiver.

Samenvatting

De Terahertz band is dat gedeelte van het spectrum liggend tussen 300 GHz en 3 THz. De eerste ontwikkelingen binnen Terahertz technologie werden aangedreven door ruimtevaartinstrumenten voor astrofysica, planetaire-, kometen- en aardwetenschappen. Echter heeft de interesse in Terahertz wetenschap zich in de afgelopen jaren snel uitgebreid door de opkomst van nieuwe toepassingen. Dit zijn toepassingen zoals beeldvorming van verborgen wapens voor militaire en civiele doeleinden, biologische en medische beeldvorming, controle van industrile processen en communicatie technologie, om maar enkele voorbeelden te noemen. Een gemeenschappelijk kenmerk van Terahertz systemen is dat ze allemaal gebruikmaken van quasi-optische elementen om de bundels te focussen en de vereiste signaal-ruisverhoudingen te behalen.

Dit proefschrift focust zich op de analyse en ontwikkeling van quasi-optische systemen voor twee verschillende types van THz applicaties: directe detectie voor ruimtetoepassingen en heterodyne beeldvorming voor beveiligings-toepassingen. In het eerste gedeelte worden op absorptie gebaseerde THz detectoren voor ruimtetoepassingen bestudeerd. Aangezien dit type detectoren alleen kan worden bestudeerd in ontvangstmodus, wordt dit vooral gedaan door middel van full-wave simulaties onder loodrechte incidentie, mits de detectoren zich onder een focusing systeem bevinden. Echter beschrijft deze methode de werkelijke koppeling tot het focusing element niet goed wanneer de F/D ratio van het systeem relatief klein is. Een spectraal model, gebaseerd op Fourier-optica, is ontwikkeld voor een accurate en efficinte analyse van lineare absorbers onder THz focusing systemen voor zowel kleine als grote F/D ratios. Het tweede gedeelte van dit proefschrift is toegewijd aan het optische systeem van een THz imaging radar voor beveiligings-beeldvorming. Het doel van dit tweede gedeelte is om een bestaande imaging radar te voorzien van nieuwe capaciteiten. Dit wordt gedaan door gebruik te maken van quasi-optische oplossingen die de scan-mechanismes en back-end elektronica niet veranderen. Allereerst is de radar voorzien van een volledig quasi-optische golfgeleider die time-delay multiplexing uitvoert op de bundels. Dit reduceert de beeld-acquisitie tijd met een factor twee doormiddel van

het toevoegen van enkele optische elementen aan het systeem. Verder is de haalbaarheid van deze techniek op grote lineare arrays van transceivers bewezen. Ten tweede is de radar voorzien van herfocussing mogelijkheden door middel van het implementeren van de klassieke optische oplossing, het verplaatsen van de transceiver.

Contents

Chapter 1

Introduction

1.1 The Terahertz Gap

The portion of the electromagnetic (EM) spectrum known as the Terahertz (THz) Gap covers the region between 300 GHz and 3 THz (also called submillimeter wave range, 100 - 1000 μm), although some authors enlarge these limits to 100 GHz - 10 THz, [1]. It occupies an intermediate region between two mature and highly technologically developed spectral bands, the microwave and optical regimes. Compared to those two bands, terahertz technology has been investigated to a lesser extent, [2]. There are two general approaches adopted to fill in THz Gap: one is up-scaling the technology developed in microwaves, where the main goal is to detect EM fields by means of using antennas, and, the other one, down-scaling the technology developed in optics, where the power of the radiation is measured. The up-scaling of the microwave technology is not easily achievable because of the inefficiency of frequency multipliers and the difficulties, and the extremely high costs, in the mechanization and manufacturing of guides and other components. Similarly, the down-scaling of photonics is also not straightforward, due to the absence of, naturally occurring, energy band-gap. Molecular absorption in gases, which is good for spectrometry at THz to characterize materials, is another drawback in the development of this technology applied to wireless sensing. However, there have been numerous recent breakthroughs in this field, which has experienced rapidly growth, reducing this gap, [3].

Space-based instruments for astrophysics, planetary, cometary and Earth science missions were the initial points for the development of terahertz sources, sensors and systems over the past several decades. However, in recent years, the interest in Terahertz science has been rapidly expanded due to the fast emergence of new terrestrial applications that motivates the development of new terahertz technology. This explosion is stimulated by the promising properties of this frequency band in terms of small wavelength, penetrating capabilities, and the possibility of using it for future high-speed communications. Examples of these relatively new applications include secure screening (concealed weapons, explosives, and drugs detection) for military and civil purposes [4, 5], biological and non biological screening and medical imaging [6], spectroscopy at submillimeter waves [7–9], industrial process control [10] and information and communication technology [11, 12].

1.1.1 Submillimeter-Wave Sensors

The sensors at submillimeter wavelengths can be classified into two different groups: *coherent* and *incoherent* (or direct) detectors, [13]. At submillimeter wavelengths, coherent detection is mostly done using heterodyne receivers due to the lack of low-noise THz amplifiers. The signal is received at THz frequency and down-converted to an intermediate frequency by combining it with the output of a local oscillator using mixers. The resulting signal, with an intermediate frequency, can then be further down-converted or demodulated. Coherent sensors at submillimeter waves include: the superconductor-insulator-superconductor (SIS) tunnel junction mixers [14, 15] and hot-electron bolometer (HEB) mixers [16] at shorter wavelengths; and Schottky diode mixers [17, 18] that can be used for the entire submillimeter-wave spectral range. On the other hand, direct detectors operating principle is absorbing EM radiation in a material and sensing the resulting change in a physical property of that material. This second type of detection provides only information about the amplitude of the signal. A broad classification of direct sensors could be: semiconductor detectors, that make use of the excitation of electrons in the valence band when radiation with energy greater than the energy gap of the material is absorbed [19]; bolometers, specifically superconducting bolometers, like Transition Edge Sensors (TES) [20, 21], that exploit the transition between the superconducting and normal state of the metal; and superconducting detectors, which operates below the critical temperature of the superconducting material, like Kinetic Inductance Detectors (KID) [22] or Superconducting Tunnel Junction (STJ) detectors [23].

1.2 THz Direct Detection for Space

Although the original motivation for the development of Terahertz science was the spectroscopy, the main driving force has been the Space science advancement. Most of the radiation in the universe emitted since the Big Bang falls into the submillimeter and far-infrared range. By studying the EM waves coming from the distant stars and galaxies at terahertz frequencies, one can study how stars are formed, galaxies evolved, and how planetary systems come about. Terahertz emission is also associated with the atmospheric behavior and components track in planets, moons, and comets. Even for the Earth, terahertz radiation can be an indicator of global warming. Instruments at submillimeter waves have, therefore, the capability to uncover a lot of information for astronomy, Earth and planetary sciences.

In astronomy, the challenge lies in finding out signals from the remote starts and galaxies embedded in the noise of interstellar background and the one generated by the sensors themselves, [13]. Submillimeter astronomical instruments operate in a regime where the signal to noise ratio (SNR) is exceptionally low. That lead to the need of developing extremely high sensitive sensors.

In the new generation of THz instruments for Space applications, arrays of thousands of detectors are required to image large portions of the sky. Among the direct detectors, the ones based on superconductors are the most sensitive ones. Throughout the last decade, instruments using hundreds of individual bolometers have beem dominating submillimiter and millimeter astronomy [24, 25]. Fully sampling arrays of up to thousands of pixels are now reaching maturity [26]. However, even with these great advances, further array scaling is strongly limited by the multiplexing factor of the readout electronics. A promising alternative to traditional bolometers are kinetic inductance detectors. KIDs are being seriously considered for such purposes due to the extreme ease of integration in array configurations that they offer. Indeed, arrays with more than 20K elements using KIDs have been recently demonstrated, [27].

1.2.1 Kinetic Inductance Detectors

Kinetic Inductance Detectors, [22,28], can relate THz power to changes in the resonance frequency of a microwave resonator. The energy required to break down a Cooper pair in a superconductor into two unbound electrons (quasi-particles) is two times the energy gap (Δ). This energy is of the order of $k_B T_c$ where T_c is the superconducting transition temperature. KIDs measure changes in the quasi-particle population that occur within the volume of a superconducting film when an EM wave of frequency higher than $2\Delta/h$ is absorbed. As a result of the increment in the quasi-particles population, there is an alteration in the complex impedance of the film related with the increase of the kinetic inductance (L_k). In practice, this variance in L_k is very small so, in order to be possible to sense it, the film has to be fabricated into a very high quality factor (Q factor) microwave resonance circuit. Generally, to create high Q microwave resonators from superconducting films for the detection of EM radiation, distributed half-wave or quarter-wave resonators using coplanar-waveguide (CPW) geometries are used. A meandering line is designed to resonate at a specific low GHz frequency (usually around 8 GHz) for which it has the length of a half or quarter wavelength. The resonator is then coupled to a CPW readout line. The transmittance S_{21} of this line shows a sharp dip in correspondence of the resonance frequency. When the THz radiation is coupled to the superconductor resonator, it breaks Cooper pairs changing the density of quasi-particles. This fact is linked to changes in the propagation constant and the characteristic impedance of the line that are translated to changes in the resonance frequency of the resonator. This variation can be easily read as a shift in the S_{21} parameter of the readout CPW line, whose dip moves to lower frequencies and becomes shallower and broader.

KIDs have the very attractive features of having a theoretical background limited sensitivity, high optical efficiency and ease of frequency multiplexing. By fabricating many resonant elements of different resonant frequencies (slightly changing the length of the resonators), it is possible to multiplex many resonators easily onto a single readout line. In figure 1.1, an image of a kinetic inductance detector and an array of them multiplexed with the same readout line is depicted.

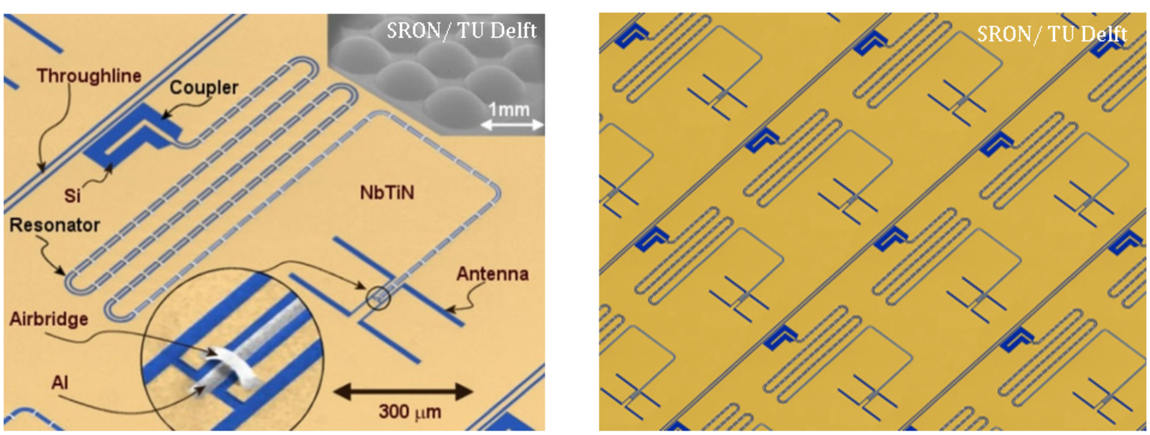

Figure 1.1: (Left) Artificially colored image of a KID, [29]. (Right) Array of KIDs with the same readout line, [30].

1.2.2 THz Power Coupling Mechanism

The coupling of the terahertz radiation onto the KID resonator line is crucial when dealing with such low SNR as the ones in astronomy. There are two different approaches to accomplish this coupling: using antennas [31–33] or using absorbers (commonly known as Lumped Element Kinetic Inductance Detector or LEKID, [34]), see figure 1.2. In the first coupling method, an antenna is connected to the CPW resonator launching the radiation received through the line. This approach allows a more simple implementation since one can design and optimized separately the antenna and the resonator. In the second scenario, the coupling is achieved directly in the resonator meander lines. By making the meander lines such that it forms an impedance matched with the incoming signal, the absorption is achieved. Therefore, the implementation becomes more complicated since the geometry optimization has to be done together with the resonator design. For both methods, detection is achieved in the same manner once the incident radiation has been absorbed. Only absorber-coupled KIDs will be discussed in this thesis.

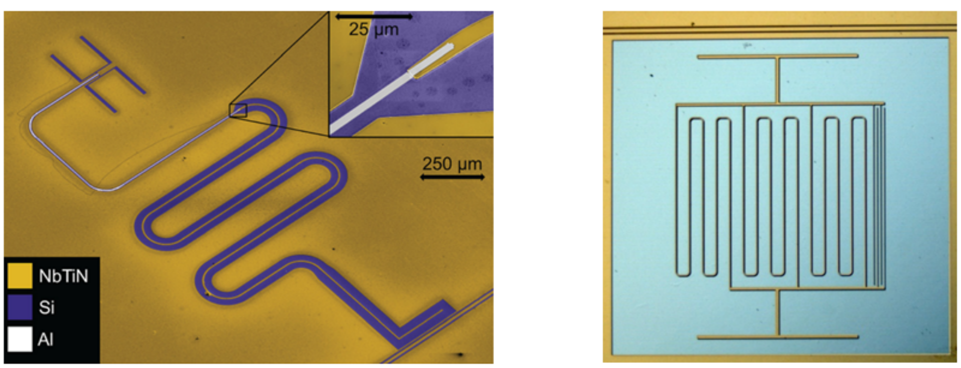

Figure 1.2: (Left) Antenna-coupled KID, [35] (Right) Absorber-coupled KID, courtesy of SRON

In real scenarios, the large arrays of KIDs would be placed in the focal plane of a telescope for the initial coupling of the radiation. A large number of elements imply that the Focal Distance to Diameter (F/D) effective ratio desired telescope have to be quite large to avoid degradation of the off focus beams. Initially, absorber-based KIDs have been used directly as free-standing arrays in the focal plane of the telescope, [34, 36]. However, the sampling and optical efficiency, as well as the mutual coupling between the elements of the array, can be improved by using an extra external coupling system as silicon lenses [37], see figure 1.3. Moreover, as it is explained in chapter 3, the operating frequency band can also be improved if the absorbers are placed in the interface between silicon and air. Despite

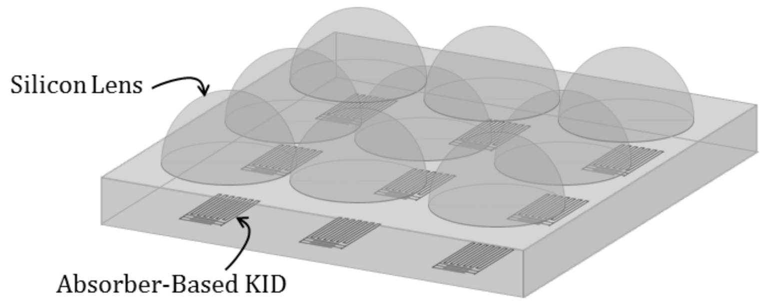

Figure 1.3: Array of absorber-based KIDs coupled to silicon lenses. One lens is used to couple the radiation onto each absorber.

the advantages of using focusing systems to couple the radiation onto the absorbers, it also complicates their analysis, design and optimization since it has to be done together with the silicon lenses. It typically requires full-wave time-consuming simulations.

1.3 THz Heterodyne Imaging for Security

During the last years, there has been a significant interest in the use of terahertz detection for imaging of concealed weapons, explosives, drugs and chemical and biological agents. The allure of terahertz detection for security imaging applications lies mainly on three characteristics of these wavelengths as explained in [4]: it is easily transmitted through most non-metallic and non-polar mediums (packaging, corrugated cardboard, some clothing and shoes depending on the material, etc.) in order to detect potentially hazardous materials contained within; those materials of interest for security reasons present characteristic THz spectra that could be used to identify them; and the fact that THz radiation is non-ionizing so it provides minimal health risks. Furthermore, while millimeter wave imaging systems [38–40] penetrate better through some materials compare to THz systems, spatial resolution and spectroscopic signatures are important considerations that favour THz scanning for security applications.

Most of the current systems for detecting weapons and other objects concealed under clothing are portal-based where the sensor and target have to be in close proximity. However, remote detection of concealed objects would add operational flexibility. Imaging of targets located at long distances requires operating at high frequencies so that portable antennas can be effectively large enough in order to maintain the spatial resolution. Over last years, the NASA Jet Propulsion Laboratory (JPL) has developed an ultra wideband 675

GHz radar, that enables sub-centimeter resolution for a static nominal standoff distance of 25 m with an aperture of 1 m and frame rates of about 1 Hz, [5]. The signal attenuation is overcome by using heterodyne transceiver architecture (i.e. active illumination), which achieves enough output power and SNR to obtain good quality images. The frequency band around 675 GHz was chosen because it lies in a trough of an atmospheric attenuation window, while providing sufficiently high spatial resolution for a favorable tradeoff between antenna size and standoff range. Besides JPL, other research groups are also making rapid progress in THz imaging radar both in the 675 GHz transmission window, [41, 42], and in the next-lower one at 350 GHz, [43].

Back to the THz imaging radar developed at the JPL, after the initial system concept was demonstrated in 2008 [44], almost all the effort has been made to reduce the acquisition time without degrading the image quality [45–47]. Increasing the radar's imaging speed is important to handle targets in motion and to image over a larger field of view (FoV). Moreover, in realistic scenarios, the target will not remain in the same position and the system will need to refocus to different distances in order to maintain a similar quality in the images. Both enhancements can be done extremely fast by using arrays. However, as a consequence of the small market for THz components, there is a very limited number of suppliers for sources and detectors and the commercial components that do exist are very expensive even compared to specialized millimeter-wave components. The high component cost is also driven by the tighter mechanical tolerances needed for devices, waveguides structures, and antennas, [48]. As an alternative, there is the option of using classical optical solutions applied for multiplexing beams and refocusing.

1.4 Thesis Goal

In previous sections, some of the limitations in THz imaging systems and their design process for outer space and security applications have been identified. Those limitations currently reduce the potential performance of the systems. The scope of this thesis is to improve the performance of THz absorbers and THz imaging radars by exploiting the use of external *quasioptical* systems. The terms quasioptics concerns to the propagation of EM radiation when the wavelength is moderate smaller or comparable to the size of the optical components (e.g. lenses, mirrors, and apertures) [49]. Quasioptics is so named because it represents an intermediate regime between conventional optics and full wave electromagnetic solutions, and is relevant to description of signals in the terahertz region. All operating THz systems make use of quasioptical elements to focus the beams and achieve sufficient SNR.

The goals of this doctoral thesis are mainly divided into two parts, both of them leaning on the study and analysis of quasioptical systems for THz imaging applications. In the first part, the main goal has been to improve the performance, in terms of optical efficiency, sampling and mutual coupling, of THz absorbers by using external quasioptical coupling systems. In the second part, the goal has been to improve the performance, in terms of acquisition time and dynamic range, of an existing THz imaging radar for security, by also using quasioptical elements.

1.4.1 Absorbers under THz Focusing Systems

While the properties of antenna-coupled KIDs can be studied in transmission or in reception, due to reciprocity, the absorber configuration can only be studied in reception. In view of this, the analysis of the absorbed-based detectors under the illumination of THz focusing systems is typically carried out, by full wave simulations, under normal plane wave incidence [34, 50]. However, resorting to a single plane wave incidence, the actual coupling to the focusing system, that occurs via a finite spectrum of plane waves (see figure 1.4), is typically not well described. The single plane wave procedure is accurate for large F/D systems (i.e. focusing systems where the focal field is the results of a small angular spectrum) typical scenario for instruments with free-standing absorbers in the focal plane of a telescope. However, in case of coupling through lenses, which are characterized by smaller F/D ratios, the standard normal plane wave incidence is not appropriate any more. In this thesis, the coupling between focusing systems and linearly polarized absorbers, embedded in a generic multilayer dielectric structure, is investigated by developing an analytical spectral model based on Fourier Optics (FO). This model is used in combination with a rigorous and analytical equivalent network representation of the absorber itself, also developed within this work. The proposed method is able to analytically and efficiently characterize the power captured by distributed absorbers located under focusing systems, also with small F/D ratios, printed on a multilayer dielectric structure, avoiding the need of full-wave time-consuming simulations. Furthermore, it explicitly highlights the physical mechanism occurring in the coupling of the plane waves with the absorbers lines. An effort has been made to highlight the absorber minimum dimension for which the mentioned method provides accurate results.

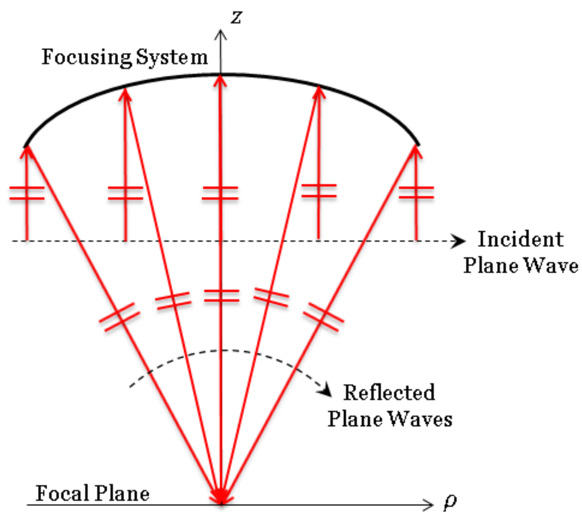

Figure 1.4: Field in the focal plane of a focusing system as a superposition of plane waves.

1.4.2 New Capabilities for a THz Imaging Radar

The JPL's 675 GHz imaging radar has demonstrated to effectively detect concealed person-borne threats with frame rates of about 1 Hz, [44]. However, the final goal for the radar is to achieve near-video rate imaging. The radar's current speed could be increased using faster beam scanning motors, but this approach is infeasible because the motor's size and power requirements increase rapidly with the FoV and frame rate. Another option to shorten the acquisition time, while minimizing the number of transceivers is to implement quasioptical time-delay multiplexing of the radar beam. This technique does not introduce any modifications in the scanning mechanism or back-end electronics hardware, while reducing the imaging time by a factor of two. In a first approach described in [46], the multiplexing was achieved using waveguide structures, leading to high ohmic losses and decreased sensitivity from transmit/receive signal leakage. A low-loss alternative is using an all-quasioptical multiplexing approach initially proposed in [45] and implemented successfully in [5] to avoid these problems while still doubling the imaging frame rate. However, to reach the desired near-video imaging speed, multiplexing a single beam into two is still not enough; a THz transceiver array will be necessary. The next generation of heterodyne arrays at submillimeter wavelengths is likely to be in the format of linear arrays, [47, 51]. In this thesis we present a study of how time-delay beam multiplexing using a quasioptical system could work for a linear array of multiple beams simultaneously.

Besides the efforts to demonstrate the feasibility of the time-delay multiplexing applied to large arrays, another goal of this thesis has been to provide the current radar with refocusing capabilities. The narrow beams needed for high resolution imaging only exist around the focal location of the antenna system. Outside this region the signal-to-noise ratio decreases and image blurring increases due to the defocusing effects resulting in gain loss and beam broadening of the antenna beam. Therefore, when objects located away from the nominal standoff distance are imaged, refocusing becomes necessary. To implement a refocusing system, the image focal plane must be displaced. Such displacement could be done extremely fast electronically by using phased arrays [52]. Although possible in theory, it is not practically achievable with the currently available THz technology. The conventional optical option, as an alternative to the phased array, to design a refocusing system by mechanically translating components has also been a goal of the present work.

1.5 Thesis Outline

The thesis is divided in seven chapters including the introductory and the concluding ones. Chapter 2 includes an overview of the different analysis methods for focusing systems along the EM spectrum and acts as a link for the following chapters. Chapters 3 and 4 are devoted to direct detection for space applications while 5 and 6 to the quasioptical system of a THz imaging radar for security use.

In *Chapter* 2[1], the representation of the focusing systems across the different frequency domains is reviewed. Besides, a technique used in the optical domain, Fourier optics, is applied to focusing systems in the THz regime to obtain a representation of the focal field as a plane wave expansion. In this chapter, the limits of applicability of this technique as a specific dimension of the focal plane are also established.

In *Chapter* 3[2], a rigorous equivalent network representing linearly polarized THz absorbers under a single plane wave incidence, is developed. The network includes, on one hand, the vectorial representation of the general propagation and scattering of the dominant EM waves and, on the other hand, details of the absorber geometry.

In *Chapter* 4, results obtained in chapters 2 and 3 are linked to obtain an complete analytical model able to accurately and efficiently characterize absorbers distributed in the focal plane of THz focusing systems. The tool derived from the model is used for designing several THz lens-coupled absorbers to be used as kinetic inductance detectors showing

[1]Part of the content of Chapter 2 and Chapter 4 is published in [J3] (see page 143)
[2]The content of this chapter is published in [J4] (see page 143)

broadband absorption efficiencies.

In *Chapter* 5[3], an all quasioptical time-delay multiplexing technique applied to linear arrays of transceivers is used to further reduce the acquisition time of a THz imaging radar. The technique is first demonstrated with measurements in a two elements transceiver, and later applied to a six elements linear array. The chapter shows that multiplexing of large arrays is not trivial since aberrations and spillover of the system come into play as the number of elements increases.

In *Chapter* 6[4], a practical implementation of a refocusing optical system that allows displacing the standoff distance of a THz imaging radar is presented. Measurements of the refocusing performance are also shown.

Finally, *Chapter* 7 summarizes the main results and conclusions obtained in this work.

[3]The content of this chapter is published in [J2] (see page 143)
[4]The content of this chapter is published in [J1] (see page 143)

Chapter 2

Analysis of Focusing Systems Throughout the EM Spectrum

Focusing systems play a fundamental role in many of the receiving and transmitting antenna systems used in a very wide range of applications. They maximize the density of radiation available in a small area, at a certain focal distance. It is thus crucial having proper methods that efficiently analyze and describe the interaction of EM fields with these elements. There is a large number of techniques to model the interaction of EM fields with focusing systems. The applicability of these techniques depends, basically, on the electrical dimensions of the object. In the following sections, a broad description of these techniques throughout the EM spectrum is done. Along this thesis, several of the techniques, methods and commercial software described in this chapter are used, depending on their suitability to the specific problem to be addressed in each case.

2.1 Low Frequency: Numerical Techniques

At low frequencies, the dimensions of the analyzed objects are usually comparable to the wavelength. It is common at these regimes to use numerical methods to solve EM problems. Numerical solution of EM problems started with the availability of modern high-speed digital computers. Since then, considerable efforts have been expended to solve practical complex problems for which close analytical solutions are unsolvable or do not exist.

The analytical starting point for electromagnetics are Maxwell's Equations, which can be expressed in two different ways: differential form, maybe the most familiar one, and source-integral form using the appropriate Green's function. Both of this forms can be written in the time-domain or in the frequency-domain. Numerical models can be developed using either form of the equations and either domain. However, the majority of finite techniques operate in the time domain while the majority of integral equation methods operate in the frequency domain, usually as a result of computational requirements.

The most common methods derived from the differential form of Maxwell's equations are the finite methods and, within them, mainly the finite-difference time-domain (FDTD), [53, 54], and the finite-elements method (FEM), [55–57]. The unknowns are distributed throughout the whole volume occupied by the fields. The numerical analysis of finite problems usually involves four basics steps: discretizing the solution region into a finite number of sub-regions or elements, deriving governing equations for a typical element, assembling of all elements in the solution region, and solving the system of equations obtained. In FDTD, the time-dependent Maxwell's equations, in partial differential form, are discretized. The electric field vector components in a volume of space are solved at a given instant in time, then the magnetic field vector components in the same spatial volume are solved at the next instant in time, and the process is repeated until the desired time or steady-state electromagnetic field behavior is observed. FEM and FDTD are both relatively straightforward to program, and they can handle highly inhomogeneous and even nonlinear media. However, they usually require large number of spatial and temporal samples to provide a satisfactory accuracy, and, therefore, they demand large computer resources.

On the other hand, a second group of numerical methods use the integral form of Maxwell's equations and are commonly known as method of moments (MoM) or boundary element methods (BEM). Harrington was the first to use the term MoM in electromagnetics in his book, [58], which remains as a fundamental reference. Since then, there has been a explosion of research and engineering involving the application of MoM to a broad variety of EM radiation and scattering problems, [59–62]. These methods employ surface elements and represent the field solution in space by the superposition of suitably chosen basis functions. The result is a dense matrix equation because, in principle, every surface element interacts with every other surface element. As it requires calculating boundaries values only, rather than values throughout the space, it is efficient in terms of computational resources for problems with a small surface/volume ratio.

It is also possible using combinations of the two groups of methods. They are called hybrid methods, and can benefit from the respective advantages of each group. In this way, one can apply differential equation formulation to very inhomogeneous (and possibly anisotropic and nonlinear) regions, and the integral equation formulation for the remaining space.

There are numerous commercial tools, but also non-commercial or academic solvers, that implement these techniques. To name some of the more widely used ones: Momentum, an integral Equation (IE) MoM solver integrated within the ADS system of Keysight Technologies [63]; FEKO, based also on the IE-MoM method but which can combine other high frequency techniques [64]; HFSS one of the first tools in the market and one of the most heavily used in industrial design enviroments, based on a 3D FEM solution of the electromagnetic topology under consideration [65]; or CST Microwave Studio (CST MWS) based on the finite integration techniques [66]. In the following chapters, CST is extensively used to analyze the electromagnetic problems addressed and also to validate the analytical method developed.

Despite the effectiveness of numerical methods, when the operation frequencies are sufficiently high (short wavelengths), these techniques become poorly convergent and inefficient. The reason is that numerical solutions are based on exact formulations that must satisfy the field consistency over the large radiating object. Therefore, the need of memory and CPU computational time rapidly grow with the size of the objects in terms of wavelengths. It becomes necessary to employ asymptotical high frequency techniques to analyze electrically large radiating objects in a manageable manner.

2.2 High Frequency Techniques

Asymptotic high frequency techniques, [67], are a set of very effective and accurate tools used to characterize the scattering from objects large in terms of wavelengths and to estimate the EM field in arbitrary complex configurations. This group of methods have been applied to a large number of EM problems such as analysis and design of parabolic reflectors, modeling of antennas and mutual coupling on complex platforms, propagation in urban environments and other complex backgrounds, indoor wireless network channels, prediction of the radar cross section of large objects, etc.

At frequencies high enough, EM wave radiation, propagation, scattering and diffraction present a very localized behavior. This local representation of EM waves is expressed in terms of rays and their associated fields. Therefore, the total high frequency field at a certain observation point is given by the superposition of the ray directly arriving from the source (known as incident ray) and the rays coming from reflection and diffraction. The incident and reflected rays follow Fermat's principle and are associated to the geometrical optics (GO) incident and reflected fields, [68]. If there is transmitted rays, there also exist GO transmitted field. This simplification of the high frequency EM waves is in high contrast with their description at low frequencies. The diffracted rays are related with geometrical and electrical discontinuities, and with points of grazing incidence on smooth convex portions of the radiating object. The presence of these diffracted rays was postulated by Keller extending Fermat's principle giving rise to the geometrical theory of diffraction (GTD), [69]. GTD exhibits singularities at GO ray shadow boundaries and ray caustics caused by the sharp edges of the structure, [70]. Uniform versions of the GTD, as the uniform theory of diffraction (UTD) [71], and the uniform asymptotic theory (UAT) [72], were developed to patch up GTD in such regions.

Apart from the ray optical methods mentioned above, also incremental theories exist within high frequency techniques. Ray optical methods require ray tracing. Incremental methods, like physical optics (PO), require numerical integration on the large object. PO approach requires, to calculate the field, an integration over the sources of the scattered field. The sources or induced currents in PO are approximated by those that would exist on an infinite plane surface which is tangent to the scattering surface at that point. The calculation of the field radiated by these currents involves no further approximations since the radiation integrals of the surface currents can be calculated by numerical integration with high precision. PO include incomplete diffraction effects because the currents at the GO shadow boundaries of the obstacle are truncated. To improve the accuracy of PO fields, it is necessary to improve the accuracy of the currents, especially in the regions where diffraction effects are important. Physical theory of diffraction (PTD), developed by Ufimtsev [73, 74], is an extension to PO where the induced surface current is improved by including a correction term that accounts for diffraction effects (as equivalently GTD completes GO).

As for the case of numerical analysis software, there are several commercial tools available for the modeling of reflector antennas using high frequency techniques. One of the most used programs is GRASP from TICRA, [75]. GRASP uses highly efficient PO/PTD and GO/GTD algorithms (and optional moment-method solver) in complex systems. Is a widely used software since it provides accurate results for complex configurations, easy definition of the geometries, near-field and far-field calculation, and is relatively fast and versatile. GRASP is considered as an industry standard for precise modeling of reflector antennas.

Throughout this thesis, PO has been used in the validation of dielectric lens fields, via in-house developed analysis tools, but also in the design and optimization of reflector systems by means of GRASP.

2.3 Optical Regime

In the optical regime, as in the rest of the spectrum, a complete electromagnetic analysis of light is often difficult to apply in most practical cases. Simplified models are commonly used. One of the most extended models used is scalar GO, where the effects of the polarization of the fields is not considered. In this model the light is represented as a set of rays, traveling in straight lines, which modify their path when they interact with a certain surface, as explained in previous section. Ray tracing can be very useful for an initial design of an optical system. However, if a more comprehensive analysis is required, usually PO approach is applied, which includes wave effects. In optical systems, where the diffraction of the field is important, Gaussian beam models are often used. They play an important role in lasers systems since many of them emit beams that can be approximate by a Gaussian profile. The mathematical function that describes the Gaussian beam is a solution to the paraxial form of the Helmholtz equation [49].

Geometrical optics is frequently further simplify, in the optical regime, by making the paraxial approximation, [76]. This approximation considers that the angles formed by the rays, respect the optical axis, are small. It is a linearization of the trigonometric functions used in the description of the optical system, that allows optical components and systems to be described by simple matrices. Related to this approximation, a way of defining the quality of an optical system is by studying its optical aberrations, [77]. Optical aberrations are defined as a deviation of the performance of the system from the predictions of paraxial optics. A well focused field is obtained when all the rays emanating from the source arrive in phase to the target. The optical path length difference is an indication of the antenna aberration (phase errors). Some of the standard analysis tools based on ray tracing are spot diagrams, that represent the rays intersecting the image plane, and ray fans, which shows ray aberrations as a function of certain coordinate.

The design of optical system requires the use of appropriate software. Also for this regime one can find several commercial programs. There exist sequential tools, that define and analyze one surface after the other in a certain order. They realize a sequential ray-tracing and geometrical calculations are applied to evaluate the system quality. Some examples are Zemax [78], OLSO [79] or CODE V [80]. One can also find non-sequential software. In this case a set of objects and light sources are defined. The paths of the reflected, refracted and scattered rays are analyzed without imposing an specific order of the elements of the system. Examples of non-sequential software are ASAP [81], LightTools [82] or TracePro [83]. Some of them, also provide a field propagation analysis, or include more than one function as CODE V. CODE V is probably the most complete and used optical software. It is recognized as international standard. Zemax is also widely used because it provides a relatively ease of use. It can model simple lenses and some diffractive optical elements, and produce very useful analysis results such as spot diagrams and ray-fan plots.

As for EM analysis techniques and commercial software described in previous sections, along this work, some of the models applied in the optical regime are used to the different THz range problems addressed, depending on the intended purpose. Thus, Zemax is used in Chapter 6 as a first step in the design of a refocusing system for a THz imaging radar. Also in this chapter, a Gaussian beam analysis is performed in order to evaluate the quality of the system.

2.4 Plane Wave Spectrum Representation

A plane wave spectrum (PWS) is a continuous superposition of uniform plane waves, so that, for each tangent point on the far-field wavefront, there is a plane wave component in the spectrum. A plane wave spectral representation of EM fields can be obtained by the free space Green's function expressed in terms of a Fourier transform, [84], as follows:

$$\frac{e^{-jk|\vec{r}-\vec{r}'|}}{4\pi|\vec{r}-\vec{r}'|} = \frac{-j}{8\pi^2}\int_{-\infty}^{+\infty}\int_{-\infty}^{+\infty}\frac{e^{-j\sqrt{k^2-k_x^2-k_y^2}|z-z'|}}{\sqrt{k^2-k_x^2-k_y^2}}e^{-jk_x(x-x')}e^{-jk_y(y-y')}dk_xdk_y \tag{2.1}$$

Equation (2.1) represents the total radiated fields as emerging from a source localized at (x', y', z') and arriving to an observation point at (x, y, z), see figure 2.1. The Green's function is the integral superposition of plane waves since the dependence from space variables is only at the exponent. The integrand represents a set of plane waves propagating in the plane x-y with propagation constant (k_x, k_y), where both k_x and k_y ranges are from $-\infty$ to $+\infty$.

High sensitivity scientific instruments typically host receivers in the focal plane of focusing systems. This implies that for each plane wave incident on the focusing system, a

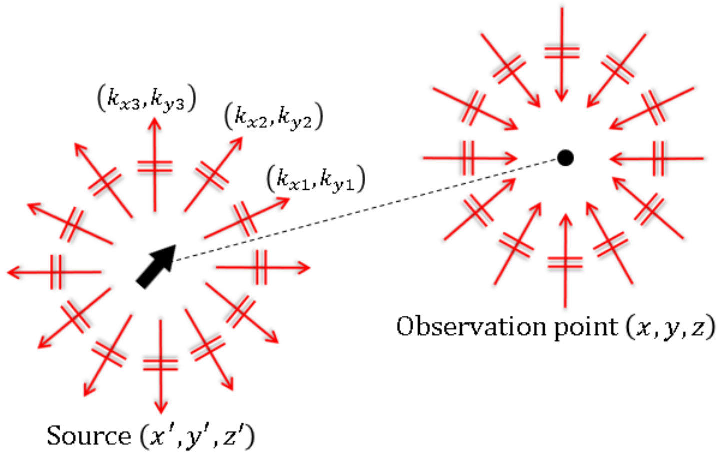

Figure 2.1: Scheme of the total radiated field emerging from a source placed at (x', y', z') and arriving to the observation point at (x, y, z), represented as a plane wave spectrum.

set of plane waves are refocused on the receivers from different directions. The complex amplitude of these plane waves (the spectrum) is, in principle, not known. However, it can be extremely useful in the synthesis of the focal plane feeds to have a plane wave representation of the focal field as in (2.1). While for large F/D focusing systems, a plane wave spectrum can be simply evaluated, its evaluation is less obvious for small or moderate F/D.

A rigorous procedure, based on asymptotic high frequency techniques, to evaluate the plane wave spectrum of the field in a focusing system, was proposed by Pathak in [85]. In this procedure, the dominant contribution to the focal field is found by transforming the PO integral over the object surface into a PWS integral with a known closed form integrand (or spectrum). This PWS integral with a known integrand could thus be evaluated using a Fast Fourier transform (FFT) algorithm. Although effective, this method is not straightforward since it requires to develop complex transitions functions.

2.5 Fourier Optics Plane Wave Spectrum at THz

In the optical domain, a common approach used in the analysis of EM waves is called Fourier optics (FO). FO is the study of classical optics using Fourier transforms, and is based in the concept of plane wave spectrum. This approach could be considered a much simpler procedure than the one developed by Pathak to represent a focal field as a plane wave expansion. This method, was introduce by E. Wolf in [86], and relies in the further approximation that the observation points would always be at a very large distance in terms of the wavelength from the focalizing lens or reflector. This approximation is very widely used in optics where the focusing systems commonly used are typically thousands of wavelength in dimension. An advantage of this representation is that it provides the PWS analytically and without the use of elaborate transition functions as in [85]. The power and wide distribution of FO derives from neglecting the phase term, since this allows to characterize the power spectrum distribution using Fourier transform techniques directly.

In microwaves, FO is simply not used because the typical dimensions of the main apertures in terms of the wavelength are too small. However, when one tries to extend the use of FO to the millimeter and submillimeter regime, with lenses and reflectors of few or tens of wavelengths in diameter, the limits of validity of these useful approximations remains to be established. As consequence people would tend to resort to techniques equivalent to the one in [85].

In this section, we present a third method to derive the PWS of focal plane fields. The method is analytical, as the one in [86] and the results are essentially equivalent. However, since a Green's function representation of the field is initially adopted and then simplified, the final results are given together with a clarification on the region of applicability of the approximate expressions. The method is similar to the one in [85] in its exploitation of the PO current approximation, nevertheless, thanks to the choice of performing the equivalent current integration on a sphere surrounding the focus, a plane wave amplitude is directly associated to every point in the surface parametrization of the PO integral.

2.5.1 Formulation

Plane Wave Spectrum Representation from PO

The field focused by any focusing system can be represented by equivalent currents distributed over an equivalent spherical surface S, of radius R, centered in the origin, see figure 2.2. Considering that there are no sources inside S, the focal electric field in an observation point, $\vec{\rho}_f = (x_f, y_f) = \rho_f \hat{\rho}_f$, can be approximated as a radiation integral starting from the equivalent currents representation. Moreover, it can be demonstrated that, if the plane wave impinges on the focusing system from broadside, the radiation integral can be expressed in terms of magnetic currents, $\vec{m}(\vec{r})$, only. In this situation the electric field along the focal region can be expressed as:

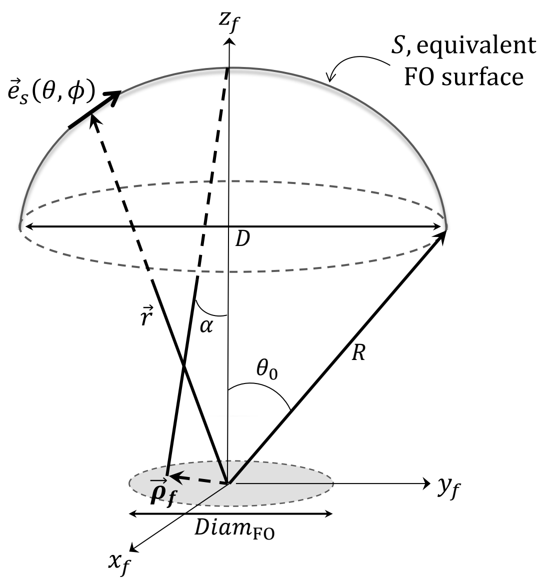

Figure 2.2: Geometry of the equivalent FO surface of a generic focusing system.

$$\vec{e}_f(\vec{\rho}_f) = \int_S j\vec{k} \times \vec{m}(\vec{r}) \frac{e^{-jk|\vec{\rho}_f - \vec{r}|}}{4\pi|\vec{\rho}_f - \vec{r}|} d\vec{r} \tag{2.2}$$

where $\vec{r} = R\hat{r}$ represent a point over the spherical surface, $\vec{m}(\vec{r}) = 2\vec{e}_s(\vec{r}) \times \hat{n}$, $\hat{n} = -\hat{r}$, $\hat{k} = (\vec{\rho}_f - \vec{r})/|\vec{\rho}_f - \vec{r}|$, k is the propagation constant inside the focusing system medium (dielectric in the case of lenses), $\vec{k} = k\hat{k}$ and $\vec{e}_s$ is the PO aperture field. The actual expression of this aperture field depends on the nature of the focusing system. A typical simplifying assumption that is used in quasioptical systems, also in the microwave domain, is that the total field incident in the focusing system can be approximated using GO. Thus, for each point on the equivalent sphere, figure 2.2, a ray is associated to the incident plane wave. In the radiation integral

$$|\vec{\rho}_f - \vec{r}| = \sqrt{(\vec{\rho}_f - \vec{r})(\vec{\rho}_f - \vec{r})} = R\sqrt{1 - \frac{2\rho_f}{R}(\hat{\rho}_f \cdot \hat{r}) + \frac{\rho_f^2}{R^2}} \tag{2.3}$$

The radiation integral in (2.2) can be simplified by assuming that the radius R is the dominant dimension involved in the distances and thus, expanding the square root for small argument to the second order on (2.3) as $\sqrt{1+x} = 1 + x/2 - x^2/8 + ...$ will lead to

$$|\vec{\rho}_f - \vec{r}| \approx R - \vec{\rho}_f \cdot \hat{r} + \frac{\rho_f^2}{2R}[1 - (\hat{\rho}_f \cdot \hat{r})^2], \tag{2.4}$$

where $\vec{\rho}_f \cdot \hat{r} = x_f \sin\theta \cos\phi + y_f \sin\theta \sin\phi$ and $\hat{\rho}_f \cdot \hat{r} = \cos\phi_f \sin\theta \cos\phi + \sin\phi_f \sin\theta \sin\phi$. Consequently, the quadratic phase term in (2.4) can be simplified as

$$\frac{\rho_f^2}{2R}[1 - (\hat{\rho}_f \cdot \hat{r})^2] = \frac{\rho_f^2}{2R}[1 - \sin^2\theta \cos^2(\phi_f - \phi)] \tag{2.5}$$

When this simplifications are introduced in (2.2), the original integral becomes

$$\vec{e}(\vec{\rho}_f) \approx \frac{jkRe^{-jkR}e^{-jk\frac{\rho_f^2}{2R}}}{4\pi} \int_\Omega \hat{k} \times (\hat{r} \times 2\vec{e}_s(\vec{r}))e^{jk\vec{\rho}_f \cdot \hat{r}} e^{jk\frac{\rho_f^2}{2R}\sin^2\theta \cos^2(\phi_f - \phi)} d\Omega \tag{2.6}$$

where $d\Omega = \sin\theta d\theta d\phi$.

Spherical PWS

The integration appearing in (2.6) is relatively complex as both observation and source points are part of the integrand. The integral can be further simplified to obtain the FO representation, as follows

$$\vec{e}_f(\vec{\rho}_f) \approx \frac{jkRe^{-jkR}e^{-jk\frac{\rho_f^2}{2R}}}{2\pi} \int_0^{2\pi} \int_0^{\theta_0} \vec{e}_s(\theta, \phi) e^{jk\vec{\rho}_f \cdot \hat{r}} \sin\theta d\theta d\phi \tag{2.7}$$

where the integration domain is extended over the solid angle subtended by the focusing system (for the case of figure 2.2, $\theta \in (0, \theta_0)$, $\phi \in (0, 2\pi)$). The electric field tangent to the equivalent sphere, $\vec{e}_s(\vec{r}) = \vec{e}_s(\theta, \phi)$, is the GO propagation of the field impinging on the focusing system to the equivalent FO sphere. The explicit expression of $\vec{e}_s(\vec{r})$ as a function of E_0^{PW}, amplitude of an external plane wave normally incident with respect to the focusing system, will be given in Chapter 4 for two cases of interest: parabolic reflector and elliptical dielectric lens.

The following simplifying hypothesis have been made in order to arrive to (2.7):

A. $\hat{k} = \frac{\vec{\rho}_f - \vec{r}}{|\vec{\rho}_f - \vec{r}|} \approx -\hat{r}$

B. $\frac{1}{|\vec{\rho}_f - \vec{r}|} \approx \frac{1}{R}$

C. $e^{jk\frac{\rho_f^2}{2R}\sin^2\theta \cos^2(\phi_f - \phi)} \approx 1.$

The points $\vec{\rho}_f$ in the focal plane where all three assumption are verified will be indicated as the FO Domain.

Cylindrical PWS

An alternative representation in terms of cylindrical waves can be obtained by a simple change of variables. In fact, writing $k_\rho = k \sin\theta$ leads to $d\theta = dk_\rho/\sqrt{k^2 - k_\rho^2}$ and, as a consequence,

$$\vec{e}_f(\vec{\rho}_f) \approx \frac{jkRe^{-jkR}}{2\pi} \int_0^{k_{\rho 0}} \int_0^{2\pi} \vec{e}_s \left(\sin^{-1}\left(\frac{k_\rho}{k}\right), \phi \right) \frac{e^{jk_\rho \rho_f \cos(\phi_f - \phi)}}{\sqrt{k^2 - k_\rho^2}} k_\rho dk_\rho d\phi. \tag{2.8}$$

where $\phi_f = \tan^{-1}(\frac{y_f}{x_f})$.

Accordingly the cylindrical spectrum is limited to $k_\rho \in (0, k_{\rho 0})$.

Cartesian PWS

In some instances a more standard Fourier Transform representation may be convenient. This representation can be applied by using the following change of variable: $k_x = k_\rho \cos\phi$ and $k_y = k_\rho \sin\phi$:

$$\vec{e}_f(\vec{\rho}_f) \approx \frac{1}{4\pi^2} \int_{-\infty}^{+\infty} \int_{-\infty}^{+\infty} \vec{E}_f(k_x, k_y) e^{jk_x x_f} e^{jk_y y_f} dk_x dk_y, \tag{2.9}$$

where $x_f = \rho_f \cos\phi_f$ and $y_f = \rho_f \sin\phi_f$ and

$$\vec{E}_f(k_x, k_y) = \frac{j2\pi Re^{-jkR}}{\sqrt{k^2 - k_\rho^2}} \vec{e}_s \left(\sin^{-1}\left(\frac{k_\rho}{k}\right), \tan^{-1}\left(\frac{k_y}{k_x}\right) \right) circ(k_\rho, k_{\rho 0}), \tag{2.10}$$

where $circ(k_\rho, k_{\rho 0})$ equals 1 for $|k_\rho| \leq k_{\rho 0}/2$ and 0 elsewhere.

2.5.2 Validity of the FO Approximations

As mention before, the domain of validity of the FO needs to be stablished since, to the best of our knowledge, such discussion is still missing and is significant at THz frequencies. As it is explained bellow, it results that, for normal incidence, the FO applicability domain is defined by a circle in the focal plane (see figure 2.2) with diameter

$$Diam_{FO} = f_{\#} min(0.4D, \sqrt{2f_{\#}D\lambda}), \tag{2.11}$$

where the integrand in (2.7) approximates the relevant PO integrand, (2.2), with an error smaller than 20% in amplitude or $\pi/8$ in phase. These limits are commonly used to define the far field of an antenna. Note that $f_{\#} = R/D$. When the conditions in (2.11) are met, the focal field in (2.7) is expressed as the sum of incremental contributions in which the observation point, $\vec{\rho}_f$, appears only at the exponent: i.e. the field is represented as a plane wave expansion if the quadratic term in front of the integral is neglected. This approximation is clearly valid for absorbers placed close to the focal point (on-focus).

Approximation on the Vector

Approximation A simply corresponds to neglecting a field contribution that, relative to the one retained in the evaluation, is proportional to $\rho_f/R = \tan\alpha$. Here, α indicates the angle subtended from the focusing system to the observation point in the focal plane, see figure 2.2. Assuming that a 20% error on the field is tolerable, $\tan\alpha < 0.2$ corresponds to an angular limitation to $\alpha < 11°$. Therefore, it is useful to define the diameter $Diam^A_{FO} = 2\rho_f$ that limits the focal plane region, S^A_{FO}, where approximation A is valid. This limit is defined, considering $R = f_{\#}D$, as

- $\rho_f/R = \tan\alpha < 0.2 \quad \rightarrow \quad \rho_f < 0.2 f_{\#}D$

Therefore

$$Diam^A_{FO} = 0.4 f_{\#}D \tag{2.12}$$

Accordingly, $\vec{\rho}_f \in S^A_{FO}$ corresponds to $|\vec{\rho}_f| < Diam^A_{FO}/2$.

Approximation on the Amplitude

Approximation B is standard in the evaluation of the far fields radiated by aperture distributions. In the present case, since the observation point is always in the near field, it is worth noticing what impact this approximation has on the relative error (ε_{rel}) for different observation points:

$$\varepsilon_{rel} = \frac{\frac{1}{|\vec{\rho}_f - \vec{r}|} - \frac{1}{R}}{\frac{1}{|\vec{\rho}_f - \vec{r}|}} \approx \frac{R - R + \vec{\rho}_f \cdot \hat{r} - \frac{\rho_f^2}{2R}[1 - (\hat{\rho}_f \cdot \hat{r})^2]}{R} \tag{2.13}$$

Essentially the error committed is zero for the observation point in the focus ($\rho_f = 0$), but for every other point there is an relative error that grows with the displacement of the observation point. The maximum error is committed considering observation points in the focal plane ($\sin\theta_f = 1$)

$$\varepsilon_{rel} \approx \frac{\rho_f}{R}\left(\sin\theta\cos(\phi_f-\phi) - \frac{\rho_f}{2R}\left[1-\sin^2\theta\cos^2(\phi_f-\phi)\right]\right) \tag{2.14}$$

To estimate this error one can focus separately in $\varepsilon_{rel} < \frac{\rho_f^2}{2R^2}$ and $\varepsilon_{rel} < \frac{\rho_f}{R}|\sin\theta|$, since the conditions are pertinent for systems characterized by large or small R/D respectively. Assuming again a 20% field error:

- $\varepsilon_{rel} = \frac{\rho_f}{R}\sin\theta = \frac{\rho_f}{R}\frac{1}{2f_\#} = \frac{\rho_f}{2f_\#^2 D} < 0.2 \quad \rightarrow \quad \rho_f < 0.4 f_\#^2 D$

  considering $\sin\theta = 1/(2f_\#)$ for large R/D.
- $\varepsilon_{rel} = \frac{\rho_f^2}{2R^2} = \frac{\rho_f^2}{2f_\#^2 D^2} < 0.2 \quad \rightarrow \quad \rho_f < \sqrt{0.4} f_\# D = 0.63 f_\# D$

The first condition implies that $S_{FO}^A \in S_{FO}^B$, except for $f_\# \leq 0.5$. The second condition is less restrictive than the one obtained by the approximation A. Thus, in practice, the conditions imposed by approximation B can be neglected in all practical cases except for low frequency reflectors (typically used in radio astronomy).

Approximation on the Phase

A third domain of applicability for the FO, S_{FO}^C, emerges from approximation C. Imposing phase errors smaller than $\pi/8$, the approximation is valid when

- $k\frac{\rho_f^2}{2R}\sin^2\theta = \frac{\pi}{\lambda}\frac{\rho_f^2}{R}\frac{1}{4f_\#^2} < \frac{\pi}{8} \quad \rightarrow \quad \rho_f < f_\#\sqrt{2f_\# D\lambda}$

This results that

$$Diam_{FO}^C = f_\#\sqrt{2f_\# D\lambda} \tag{2.15}$$

This condition has an explicit dependency on the wavelength and leads to the smallest domain for focusing system characterized by very large diameters since it does not grow linearly but with the square root of D.

The overall applicability domain of the FO is, for the study cases, the smallest of the two: $S_{FO} = min(S_{FO}^A, S_{FO}^C)$.

Figure 2.3 shows the $Diam_{FO}^{A,C}$ for $R/D = 0.6$ and $R/D = 3$. For small diameters, approximation A is the most restricting one. This same approximation remains dominant also for relatively large diameters as the R/D number increases since the quadratic phase

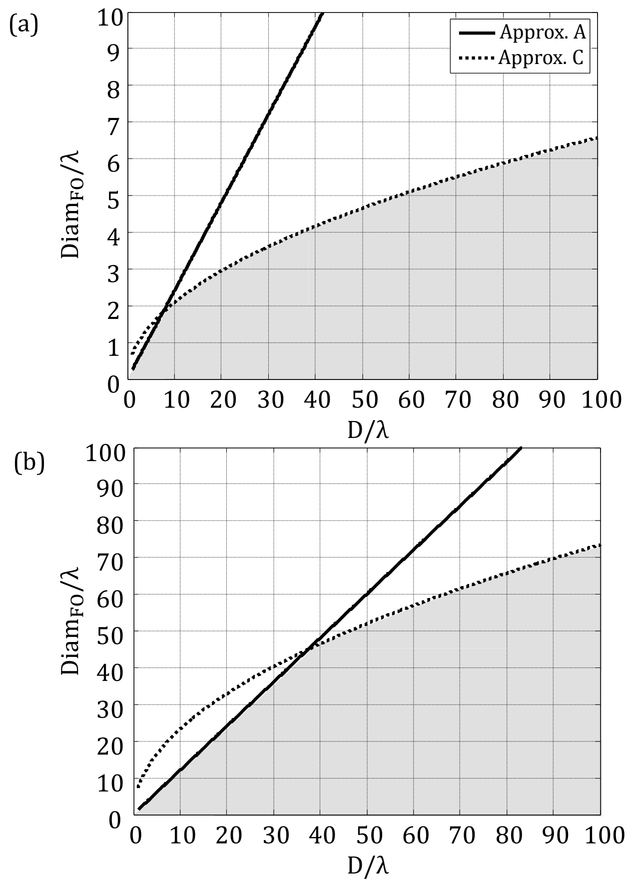

Figure 2.3: Limits of applicability of the FO expression for (a) $R/D = 0.6$ and (b) $R/D = 3$. The gray area is the region where all the approximations are full-filled.

plays a smaller role. For large R/D and large diameters in terms of the wavelength (as in the optical domain), approximation C is the dominant one.

In Chapter 4, practical examples of the application of these approximations, for a dielectric elliptical lens and a parabolic reflector, are shown.

2.6 Conclusions

In this chapter, a brief summary of the representation of focusing systems across the different frequency domains has been presented. Furthermore, Fourier Optics, a technique used in the optical domain, has been applied to focusing systems in the THz domain to obtain a representation of the focusing field as a plane wave expansion. The limits of applicability of this technique seemed to be unestablished. Therefore, an effort has been made in order to obtain the applicability limits of Fourier Optics as a specific dimension of the focal plane.

Chapter 3

THz Linearly Polarized Absorbers

3.1 Introduction

Electromagnetic absorbers play a fundamental role in high frequency direct detection systems. In particular, they are the key point in absorber-coupled KIDs. The upper right inset of figure 3.1 shows an sketch of such detector. In these instruments, the absorber is essentially the only component limiting the frequency bandwidth of operation. Accordingly, it is useful to design it as efficient as possible over a broad band. Different absorbed-based KID detector configurations are currently being investigated for future THz space instruments, such as SAFARI (SpicA FAR-infrared Instrument), [87].

The absorber is an integral part of the microwave resonator. Indeed, the microwave current has to flow along the whole geometry of the absorber. The inductive meander of the resonator (see figure 3.1) constitutes typically the absorbing area. Therefore, the absorber is made of parallel absorbing strips. This geometry basically resembles the so called Salisbury screen [88] (i.e., a lossy continuous screen, of appropriate thickness h, placed at a quarter wavelength from a backing reflector [89]), where parallel absorbing strips can be used to match the wave impedance to a low sheet resistance, Ω/sq, which is typical of superconducting materials [90]. A typical structure investigated in this chapter is represented in figure 3.1. Strips are periodically and tightly arranged to guarantee that the fundamental Floquet Wave (FW), which represents the average field over the space, experiences an approximate resistive boundary condition. The absorber is represented here as an infinite array of strips in order to calculate analytically the current flowing along them. The absorbed power would be instead evaluated over a finite area. This is possible because the current can be assumed unperturbed by the finiteness of the absorber due to the high losses.

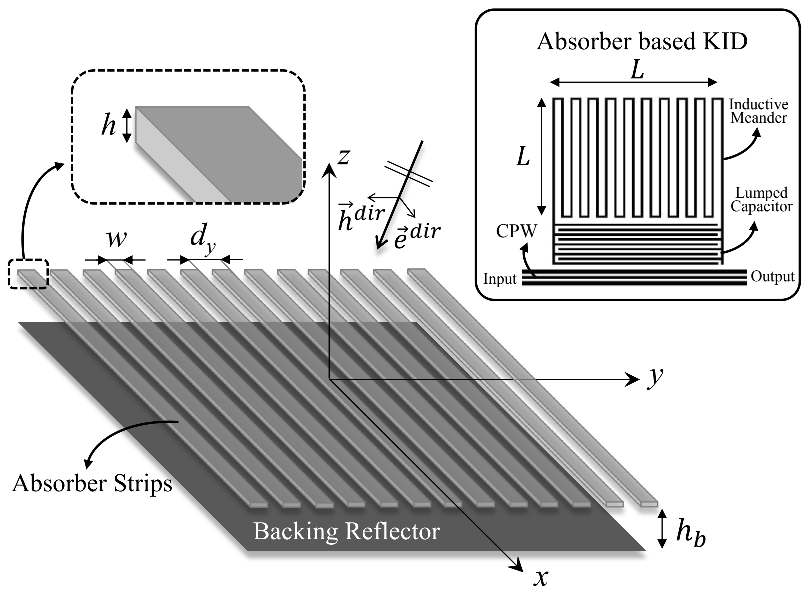

Figure 3.1: Geometry of a linearly polarize absorber with backing reflecor. Upper right inset shows a sketch of an absorber-based KID detector.

Absorbers have manufacturing limitations imposed by the available superconducting materials used. Aluminum (Al) is a well characterized and widely used material [91], but unfortunately provides very low resistivity. This in turns leads to very thin strips, which not only behave as absorbers, but also introduce important inductive loading that makes achieving high absorption efficiency very difficult. Titanium Nitride (TiN) is emerging as a possible alternative [90] and, thanks to its large resistivity, it allows for wider strips reducing the inductance loading and enabling fabrication at higher frequencies. However, its use as superconducting material is still in an experimental phase [92]. Thus, both configurations are still being investigated.

As mention in previous chapters, the detectors would be located in the focal plane of the space instrument focusing system (parabolic reflector or elliptical lens). For moderate Focal Distance to Diameter ratios (F/D), not only plane waves coming from broadside will arrive to the absorber, but also plane waves coming from directions significantly different from broadside will be impinging on it. In these cases, a significant mismatch between the incoming waves and the absorber can reduce significantly the sensitivity of the detectors. Moreover, significant cross-polarization problems can occur due to the coupling between TE (E-field has no longitudinal component, along z-axis) and TM (H-field has no longitudinal component, along z-axis) waves.

It is therefore convenient to have an equivalent network spectral representation that provides analytically the current flowing along the strips, to calculate the absorber performance for very large frequency bands and a wide range of plane wave incidence angles. Moreover, such analytical network representation is used in Chapter 4 to characterize absorbers in the presence of focusing systems by using the plane wave expansion representation of the field in a focal plane derived in Chapter 2.

In this chapter, we present a rigorous and analytical equivalent network suitable for the analysis of these structures. Its use allows us to derive the optimal geometrical absorber parameters for achieving a broadband absorption in the order of one octave. This bandwidth is basically the same that the one obtained in a standard Salisbury absorber configuration (i.e., by using a lossy continuous screen). It turns out that the absorbers should be printed on extremely thin dielectric layers to obtain such bandwidths. Moreover we show that high absorption efficiency bandwidths of the order of 2.6 octaves can be achieved when the plane wave is incident from a dense medium with basically the same backshort distance. The geometries presented in this chapter are within the physical limits of general absorbers [93]. In fact, the optimization of the KIDs absorbing geometry does not aim to reduce its physical thickness since these detectors are operating in the THz regime.

3.2 State of the Art in the Analysis of Absorbers

Several authors have investigated gridded structures in the past for the optimization of microwave absorbing and scattering, mostly for Radar applications [94–100]. The main objectives for the absorber designs were the thickness reduction and the enlargement of the frequency band. To achieve wider frequency response, circuit analog absorbers were introduced in [95], where resistive periodic patterns (i.e. resistive FSS) were employed instead of plain lossy continuous screens. The design procedure of these absorbers is basically done by first synthesizing RLC circuits and then using full-wave simulations for the resistive FSS [98, 99]. All these previous works use FSS geometries (rings, patches, crosses, etc.) that are not appropriate for a KID based detectors since they do not allow a continuous current flow necessary to implement the microwave read out mechanism. KID based detectors are then realized by using resistive wire grids.

The milestone in the analysis of wire grids excited by plane waves was established by Kontorovich [101] who developed the first analytical model to extract the currents on the

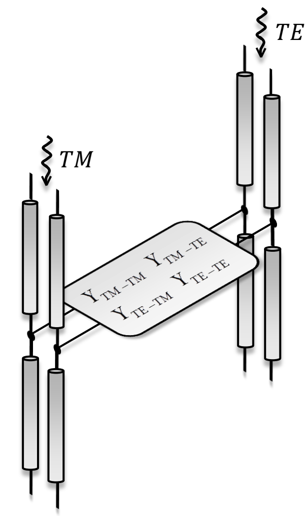

Figure 3.2: Equivalent network for the fundamental Floquet wave, with a shunt two-port network that represents the metallic grid.

strips and the scattering parameters of a lossless grid. In [102], the group of Tretyakov, building on the original works from Kontorovich, developed analytical models to evaluate the currents and the scattering from these wire grids, enlarging the range of validity of the formulas in [101]. A similar work [103], again extending the work of Kontorovich [104], proposed an analytical representation of the scattering from crossing wire grids. It included an equivalent network that represents the loads of the crossing wires as shunt loads on the equivalent transmission lines that represent the fundamental FW. Also Agranovich in [105] analyzed the interaction of electromagnetic plane waves with metallic strips. Since then, many other works aimed at characterizing general FSS like configurations on a ground plane, have been presented. All these works resort to numerical simulations to extract lumped components corrections to the plane wave equivalent networks, as the one shown in [99] for resistive FSS. A complete review of the recent research in this domain is presented in [106]. A general procedure to evaluate numerically equivalent networks of lossless FSS was proposed in [107], where the explicit coupling of TE and TM modes was introduced as a dedicated two-port network as shown in figure 3.2.

To our knowledge, all previous works characterize the network loading of the absorbers as components directly in parallel with the equivalent transmission line of the fundamental FW. The shunt components propagate electric currents proportional to the magnetic field associated with the fundamental FW (TE or TM). Overall, it appears that linearly polarized FSS have been widely analyzed. However, two areas of improvement seem to remain.

A first *technical* problem with existing mono-modal analytical networks arises, as shown in [108–110], for the cases in which the grids are printed on extremely thin dielectric stratifications, when backing reflectors are close to the grids or when the period is large compare to the wavelength. In these cases the interaction of the higher order FW cannot be represented easily. In only a few simple cases dedicated extensions have been presented: for instance, for normal incidence and free space in [108].

A second problem with the existing networks is that they give information on the scattering parameters but they do not provide any explicit relationship between the impinging waves and the electric currents on the strips. This limits the applicability of these networks to design absorbers since they rely only on scattering analysis, i.e., on an indirect parameter rather than on a direct relationship between the absorbed power and the geometrical parameters.

3.2.1 Analytical Equivalent Network

This work presents for the first time a rigorous, completely analytical, equivalent network for the analysis of linearly polarized absorbers that explicitly highlights all major physical mechanisms occurring in the coupling of plane waves with the strip currents: see figure 3.3. The starting point for this work is the equivalent network in [111], that can characterize analytically doubly periodic connected arrays, including the feeding details of the antenna, by using the Green's functions of linearly polarized structures developed in [112] and [113].

The elegance of the network introduced here stems from its *zooming* property. It allows the fundamental FW plane wave fields, in the surrounding of the absorber, to be treated separately from the electric currents flowing in the strips. This separation is achieved via two sets of transformers. A first set of transformers (1:$\cos\phi$ and 1:$-\sin\phi$, being ϕ the azimuthal angle) accounts for the superposition on the absorber plane of the two, otherwise independent, TE and TM propagating FW. A second transformer (n) accounts for the coupling between the dominant FW magnetic field (now TE+TM) and the electric currents in the strips. This new aspect is especially useful to relate the absorbed power with the geometrical parameters. Moreover it is very suitable when one wants to load the absorber strip with lumped components, i.e. resistors or capacitors or inductors, for instance to fine tune absorber frequency behaviors, possibly with active devices [114]. Apart from the elegance, the eventual equivalent network does not suffer for small thickness stratifications, because it presents an explicit term, Z_{rem}, which will account for all higher order mode interactions.

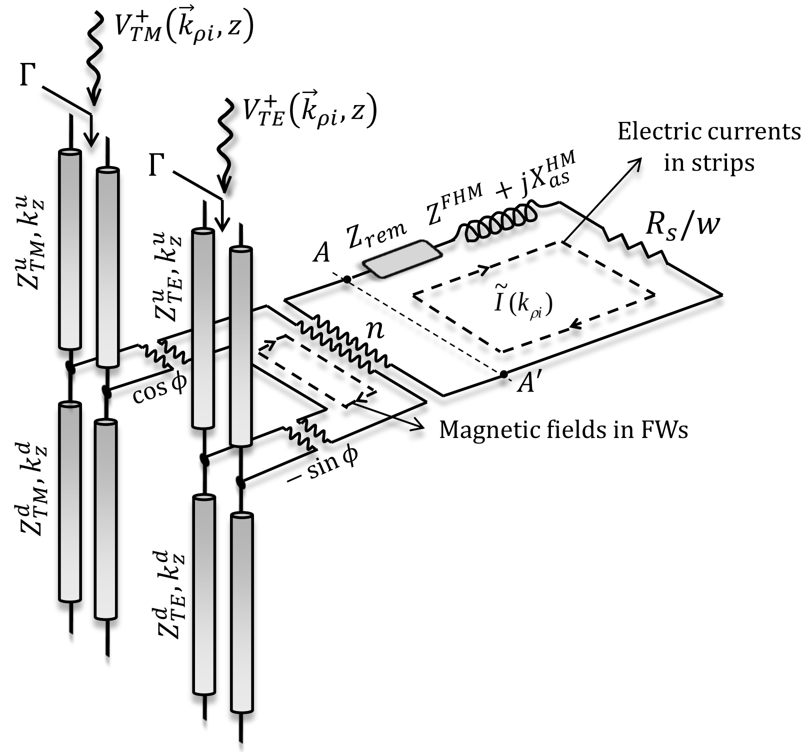

Figure 3.3: Equivalent network for the fundamental FW with explicit shunt two-port network representing an absorber placed between two infinite dielectric media.

3.3 Derivation of the Strip Current and Impedance

The currents induced on a linearly polarized absorber under plane wave incidence are evaluated in this section, by extending the work in [111]. In the present context, the periodicity is only along the y-direction (d_y) and the ohmic losses are distributed over the entire length of the strips. With reference to figure 3.1, the strip array is illuminated by a plane wave polarized along $\vec{e}^{\,dir}$ (this field is referred as direct field in the rest of the chapter). This plane wave can be expressed as the superposition of two waves polarized along the spherical unit vectors, i.e. $\vec{e}^{\,dir} = e^{-j\vec{k}_{\rho i}\cdot\vec{\rho}}e^{jk_{zi}z}(e_{\theta}^{dir}\hat{\theta} + e_{\phi}^{dir}\hat{\phi})$. The direct plane wave, arriving from the direction (θ,ϕ) is characterized by a wave vector $\vec{k} = \vec{k}_{\rho i} + k_{zi}\hat{z}$, where $\vec{k}_{\rho i} = k_{xi}\hat{x} + k_{yi}\hat{y}$ with $k_{xi} = k\sin\theta\cos\phi$, $k_{yi} = k\sin\theta\sin\phi$ and $k_{zi} = k\cos\theta$.

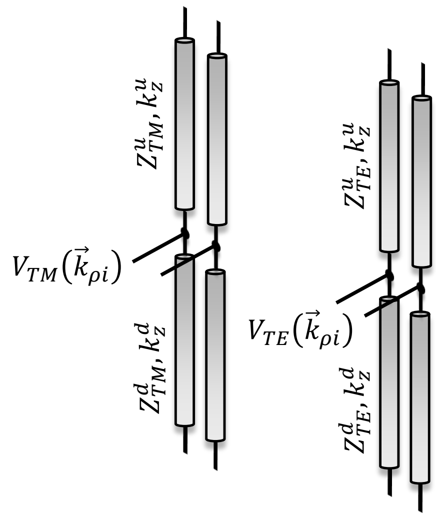

Figure 3.4: Equivalent transmission line to calculate the expressions of the voltages V_{TM} and V_{TE}. This case represents the absorber placed between two semi-infinite dielectric media. It is clear that, in case of more stratifications, several sections of transmission lines would be cascaded.

3.3.1 Integral Equation

For the specific application under analysis, the thickness h of the strips that compose the absorber is much smaller than both the wavelength of the impinging wave and the skin depth of the metal of which the strips are made. Thus, the effect of the current flowing in each strip can be equivalently taken into account by a surface electric current $\vec{J}_s(x, y)$ distributed on the media interface (see figure 3.5) that satisfies the following relation

$$\vec{E}(x, y, z = 0) = \vec{J}_s(x, y) R_s \tag{3.1}$$

where $R_s = 1/(\sigma h)$ is the sheet resistance, Ω/sq. Furthermore, the width of the strips being much smaller that the wavelength, the surface current on the array can be approximated as

$$\vec{J}_s(x, y) = i(x, \vec{k}_{\rho i}) \sum_{n=-\infty}^{+\infty} e^{-jk_{yi} n d_y} \frac{\text{rect}(y - n d_y)}{w} \hat{x} \tag{3.2}$$

where $\text{rect}(y)$ equals 1 for $|y| \leq w/2$ and 0 elsewhere. A flat transverse profile is used instead of the common edge singular one because of the high losses. The total electric field on the absorbing strips can be expressed as the superposition of the incident, $\vec{e}^{\,i}(x, y)$, and the scattered, $\vec{e}^{\,s}(x, y)$, fields, i.e. $\vec{J}_s(x, y) R_s = \vec{e}^{\,i}(x, y) + \vec{e}^{\,s}(x, y)$. An integral equation is then obtained expressing the scattered electric field as the convolution of the (unknown) surface current and the relevant Green's function:

$$\vec{J}_s(x,y)R_s - \int_{Array} \underline{\underline{g}}(\vec{r},\vec{r}\,') \cdot \vec{J}_s(x,y) d\vec{r}\,' = \vec{e}\,^i(x,y). \tag{3.3}$$

Eventually, the integral equation can be imposed on the x-component of the electric field only. It requires the evaluation of $\vec{e}\,^i \cdot \hat{x}$. This latter can be expressed as

$$\vec{e}\,^i(\vec{k}_{\rho i}, \vec{\rho}, z=0) \cdot \hat{x} = e^{-j\vec{k}_{\rho i}\cdot\vec{\rho}} E_{ix}(\vec{k}_{\rho i}) \tag{3.4}$$

Let us impose the average validity of this equation over the $n = 0$ strip only on both sides of (3.3), it is transformed as follows:

$$\begin{aligned}\frac{R_s}{w^2}\int_{-w/2}^{w/2} i(x,\vec{k}_{\rho i})dy - \frac{1}{w^2}\int_{-w/2}^{w/2}\int_{Array} g_{xx}(x,y;x',y')i(x',\vec{k}_{\rho i})\\ \sum_{n=-\infty}^{\infty} e^{-jk_{yi}nd_y}\mathrm{rect}(y'-nd_y)d\vec{r}\,'dy = \frac{1}{w}\int_{-w/2}^{w/2} e^{-j\vec{k}_{\rho i}\vec{\rho}}E_{ix}(\vec{k}_{\rho i})dy.\end{aligned} \tag{3.5}$$

3.3.2 Spectral Equation for the Electric Current on the Strips

Once the integral equation is set up, its solution can be obtained proceeding as described in [97]. In short, the integral equation (3.5) is simply transformed in an algebraic equation by translating both left hand and right hand sides in spectral domain making use of the pertinent spectral expressions for the Green's function, $g_{xx}(\vec{r},\vec{r}\,') = FT^{-1}[G(k_x,k_y)]$, the current $i(x,\vec{k}_{\rho i}) = FT^{-1}[I(k_x,\vec{k}_{\rho i})]$, and the incident field, $E_{ix}(\vec{k}_{\rho i})$.

Furthermore, the equation is rendered more compact representing separately the transverse spectral integration by introducing a dedicated function, $Z(k_x)0$, that represents the sum of the fields scattered by the entire array for each longitudinal wavenumber k_x. With the introduction of $Z(k_x)$, which has dimensions of impedance per unit length, Ω/m, the spectrum in k_x obeys the equation:

$$\begin{aligned}\frac{R_s}{w}\int_{-\infty}^{\infty} I(k_x,\vec{k}_{\rho i})e^{-jk_x x}dk_x + \int_{-\infty}^{\infty} I(k_x,\vec{k}_{\rho i})Z(k_x)e^{-jk_x x}dk_x =\\ \mathrm{sinc}(k_{yi}w/2)\int_{-\infty}^{\infty} 2\pi\delta(k_x - k_{xi})E_{ix}(\vec{k}_{\rho i})e^{-jk_x x}dk_x.\end{aligned} \tag{3.6}$$

The explicit expression for the function $Z(k_x)$ can be expressed as a spatial summation:

$$Z(k_x) = \frac{-1}{2\pi} \int_{-\infty}^{\infty} G(k_x, k_y) \sum_{n=-\infty}^{\infty} e^{-jk_{yi}nd_y} e^{jk_y nd_y} \mathrm{sinc}^2 \left(\frac{k_y w}{2} \right) dk_y \tag{3.7}$$

or, equivalently, as a summation of FW by resorting to the Poisson infinite summation as follows:

$$Z(k_x) = \frac{-1}{d_y} \sum_{m_y=-\infty}^{\infty} G(k_x, k_{ym}) \mathrm{sinc}^2 \left(\frac{k_{ym} w}{2} \right) \tag{3.8}$$

where $k_{ym} = k_{yi} - 2\pi m_y d_y$.

Equating the spectra on both sides of equation (3.6) we obtain the explicit expression for the spectrum of the current in the strips:

$$I(k_x, \vec{k}_{\rho i}) = \frac{2\pi\delta(k_x - k_{xi}) \mathrm{sinc} \left(\frac{k_{yi} w}{2} \right) E_{ix}(\vec{k}_{\rho i})}{Z(k_x) + \frac{R_s}{w}} \tag{3.9}$$

Accordingly, the current induced by the considered plane wave in each of the strips and at x is:

$$i(x, \vec{k}_{\rho i}) = \tilde{I}(\vec{k}_{\rho i}) e^{-jk_{xi}x} \tag{3.10}$$

where

$$\tilde{I}(\vec{k}_{\rho i}) = \mathrm{sinc} \left(\frac{k_{yi} w}{2} \right) \frac{E_{ix}(\vec{k}_{\rho i})}{Z(k_{xi}) + \frac{R_s}{w}} \tag{3.11}$$

Once the total current flowing in the central strip $i(x, \vec{k}_{\rho i})$ is known, the current density over the entire array can be calculated by using (3.2).

In equation (3.11), $E_{ix}(\vec{k}_{\rho i})$ represents the amplitude of the incident electric field component along x calculated at the strip position in the absence of it. The *incident field* equals the *direct field* if the strips are in free space. However, in the presence of general stratifications the incident field will be accounting for possible multiple reflections. The explicit relationship between the incident and direct fields is further explained in Section 3.6. Also in (3.11), R_s is the strips sheet resistance (Ω/sq), which can be expressed in terms of the material conductivity , and the thickness of the strips h, assumed much smaller than the skin depth, as $R_s = 1/(\sigma h)$. Finally, the spectral impedance $Z(k_x)$, which represents the electric field scattered by the equivalent currents of the array averaged over the central strip, can be expressed as:

$$Z(k_x) = \sum_{m_y=-\infty}^{+\infty} Z^{m_y}(k_x) \tag{3.12}$$

defining

$$Z^{m_y}(k_x) = -\frac{1}{d_y} G(k_x, k_{ym}) \mathrm{sinc}^2\left(\frac{k_{ym}}{2}\right) \tag{3.13}$$

The analytic expression of the spectral Green's function $G(k_x, k_y)$ depends on the stratification considered. It can be expressed in terms of the TE and TM input impedances of the upper (Z_{TE}^u and Z_{TM}^u) and lower (Z_{TE}^d and Z_{TM}^d) half spaces, depending on the specified stratification, as:

$$G(k_x, k_y) = -Z_{TM}\frac{k_x^2}{k_\rho^2} - Z_{TE}\frac{k_y^2}{k_\rho^2} \tag{3.14}$$

where $Z_{TM} = Z_{TM}^u Z_{TM}^d/(Z_{TM}^u + Z_{TM}^d)$ and $Z_{TE} = Z_{TE}^u Z_{TE}^d/(Z_{TE}^u + Z_{TE}^d)$.

While the current expression has been previously evaluated with similar techniques in the literature, the in depth analysis of impedance $Z(k_x)$ constitutes the core of the equivalent network presented in this chapter, figure 3.3.

3.4 Optimized Absorber Geometries

In this section, the analytical expression of the current derived in (3.11) is used to optimize the geometry of absorber based KIDs. Absorbers of the two different superconducting materials (working in the region above the cut-off) relevant to the KIDs are investigated here: TiN and Al. Several stratifications are considered to maximize the frequency band of absorption. In all the cases, the width and the period are chosen to maximize the absorbed power as $wZ(k_x) \approx R_s$. The actual power absorbed, that depends also on the considered stratification, is evaluated and validated with full wave simulations in section 3.7.

The following stratifications (shown in figure 3.5) are investigated:

I. Absorber printed on thin slab and backed via backing reflector, representing an absorber placed directly in the focal plane of a parabolic reflector.

II. Absorber embedded in the interface between two semi-infinite dielectrics, representing an absorber printed at the interface between a dielectric elliptical lens and free space.

III. Same stratification as in case II. but backed by a reflector at a distance h_b (with the separation layer obtained either via a dielectric slab or free space).

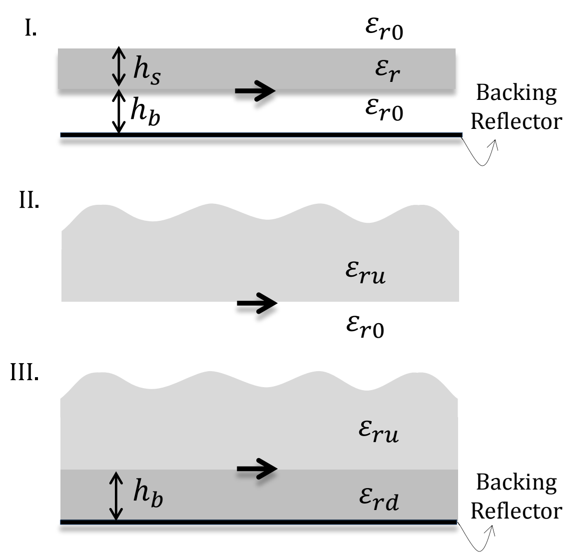

Figure 3.5: Geometries of the investigated stratifications.

Note that the network in figures 3.3 and 3.4 specifically represents case II., since there are only two transmission lines equivalent to each infinite dielectric.

When the absorber is placed directly in the focal plane of a parabolic reflector, the stratification to be considered is case I. A backshort is used to maximize the received power, and the absorber is placed on a silicon dielectric slab for fabrication reasons. In order to obtain impedances with low Q resonant curves, it is necessary to drastically decrease the substrate thickness to values of around $1 - 10$ μm. Note that this case is also relevant in bolometric detectors where the absorber needs to be printed on a membrane for thermal reasons.

The TiN strips can be fabricated with a thickness of $h = 50$ nm, leading to a sheet resistance of $R_s = 30$ Ω/sq, [92]. Figure 3.6a shows the real and imaginary part of the grid impedance in (3.12) (solid lines) times the absorber width for the optimized design of case I as a function of the frequency for normal incidence, $k_{xi} = 0$. The impedance shows, around the central frequency, a real part equal to the sheet resistance and a small imaginary part.

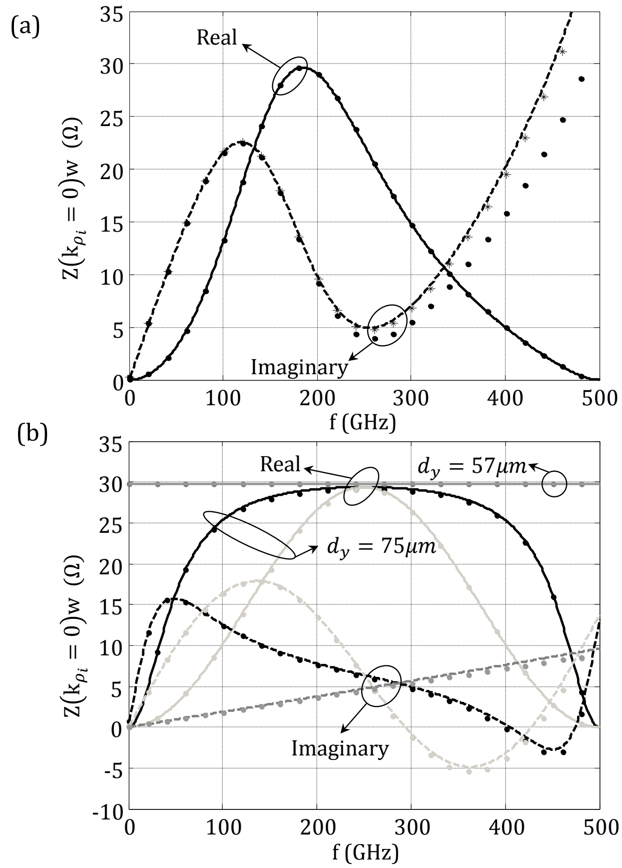

Figure 3.6: Impedance of TiN designs for the cases shown in figure 3.5, for normal incidence: (a) Case I with $w = 24\mu m$, $d_y = 300\mu m$, $\varepsilon_r = 11.9$, $h_s = 10\mu m$, and $h_b = 300\mu m$. (b) Case II (dark grey lines), case III with $\varepsilon_{rd} = 11.9$ and $h_b = 87\mu m$ (light grey lines), and case III with $\varepsilon_{rd} = 1$ and $h_b = 300\mu m$ (black lines). The three cases have $w = 20\mu m$ and $\varepsilon_{ru} = 11.9$. The dots represent the analytical impedance, $Z^{m_y=0} + jX_{as}$, for each case. The asterisks in (a) represent the analytical impedance including the first higher order modes $Z^{m_y=0} + Z^{FHM} + jX_{as}^{HM}$.

When the absorber is placed under a dielectric lens, the stratifications to be considered are II. and III. The case of semi-infinite dielectrics, II., leads to a real part of the impedance essentially constant, while the imaginary part presents a linear growing positive behavior (inductance loading) as shown in figure 3.6b (dark grey lines). The case involving a backing reflector in silicon, III., (also shown in figure 3.6b) is characterized by a low Q resonant curve, associated with h_b being a quarter wavelength. However, if the backshort is made of air, $\varepsilon_{rd} = 1$, the impedance presents an even smaller frequency variation.

In all these TiN cases, the real part of the impedance is larger than the imaginary part, which is always of the order of 5 Ω at the central frequency. In case of Al KIDs, the strip thickness is $h = 27$ nm and the sheet resistance is $R_s = 2$ Ω/sq. The optimal

Al absorber impedance for configurations II and III. is shown in figure 3.7. In this case, the imaginary part of the impedance is comparable with the real part, thus it is difficult to get $wZ(k_x) \approx R_s$ without reaching values of w too small and difficult to manufacture. Even so, the absorber geometry is optimized to obtain an imaginary part of the impedance almost constant over the absorption band. The small width makes the fabrication of this configuration more difficult at higher frequencies.

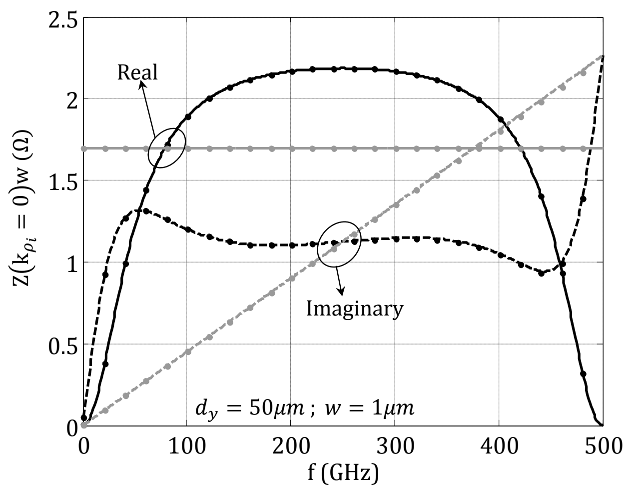

Figure 3.7: Impedance of an Al design for the last two cases shown in figure 3.5, for normal incidence: Case II (grey lines) and case III with $\varepsilon_{rd} = 1$ and $h_b = 300\mu m$ (black lines). The two cases have $d_y = 50\mu m$,$w = 1\mu m$ and $\varepsilon_{ru} = 11.9$. The dots represent the analytical impedance, $Z^{m_y=0} + jX_{as}$, for each case.

3.5 Dominant Terms of the Impedance

The impedance $Z(k_x)$ is dominated by two different mechanisms. On one hand, a tight periodicity along y guarantees the dominance of the fundamental FW, which accounts for propagating incident and scattered fields. On the other hand, the fact that the currents are bound to be flowing in narrow strips induces around them strongly inductive fields that are associated with higher order transverse (along y) FW. These two effects can be highlighted by extracting from the summation in equation (GeneralImpedance) the two terms that represent these mechanisms: the fundamental ($m_y = 0$) FW term, $Z^{m_y=0}$, and an analytical asymptotic contribution representing the higher order FW terms, that will be indicated as X_{as}.

The original impedance $Z(k_x)$ can then be represented by these two terms plus a remaining contribution, Z_{rem}:

$$Z(k_x) = Z^{m_y=0}(k_x) + jX_{as}(k_x) + Z_{rem}(k_x) \tag{3.15}$$

The asymptotic spectral contribution reactance can be obtained, as shown in the Appendix A, by retaining the small period approximations in the summation over the higher order FW. The steps lead to

$$X_{as}(k_x) = \frac{\xi_0}{\pi}\left(\frac{k_0}{2} - \frac{k_x^2}{k_0(\varepsilon_r^d + \varepsilon_r^u)}\right)\left[\ln\left(\frac{d_y}{2\pi w}\right) + \frac{3}{2}\right]. \tag{3.16}$$

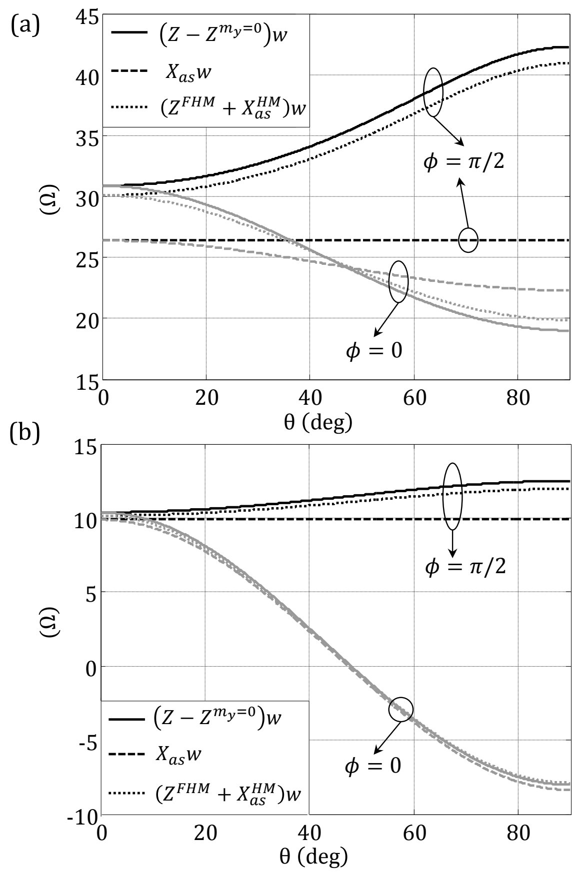

Figure 3.8: Impedance for two cases shown in figure 3.5 versus the plane wave incidence angle (θ), for $\phi = 0$ (black) and $\phi = \pi/2$ (grey). (a) Case I with $d_y = 0.4\lambda_0$ and $w = d_y/12.5$. (b) Case III with $d_y = 0.35\lambda(\lambda = \lambda_0/\sqrt{\varepsilon_{ru}})$, $w = d_y/3.75$ and $\varepsilon_{rd} = 1$. In both cases $\varepsilon_{ru} = 11.9$ and $f = 400$ GHz. The term $(Z - Z^{m_y=0})$ is represented with solid lines, the term X_{as} with dashed lines and the term $(Z^{FHM} + X_{as}^{HM})$ with dotted lines.

The expression for the reactance X_{as} is similar to the expressions reported in [103] and [115]. The main difference come from the fact that we are using a constant transversal behavior of the current instead of an edge singular one. It is the same as the one of a strip printed at the interface between two different dielectric semi-spaces: i.e., it does not depend on the stratifications as higher order spectral components are exponentially attenuated.

Figures 3.6 and 3.7 also show with dots, for all the cases studied, the values of the analytic impedance, $Z^{m_y=0} + jX_{as}$, for normal incidence (i.e., $k_{xi} = 0$). In figure 3.6b and 3.7 a very good agreement is observed between the analytical impedance and the impedance in (3.12), so that the remaining term Z_{rem} can be in fact neglected. In the Al design in figure 3.7, the geometry was optimized to get a flat behavior of the imaginary part of the impedance by compensating the increasing asymptotic term, X_{as}, with the decreasing imaginary part of $Z^{m_y=0}$. In fact, since the dominant terms of the impedance are explicitly dependent from the geometrical parameters, their analytical expressions can be used to fine tune the absorber designs.

In figure 3.6a there is a larger difference between the imaginary part of the impedance including all FW terms and the analytical one. This is due to the effect of the higher order FW modes. On one hand, the period is relatively large. On the other hand, to calculate the asymptotic term, we are assuming, that the Green's function tends asymptotically to the same value that is assumed by the configuration associated with two semi-infinite homogeneous dielectric layers, so the effect of thin layers is not included. A different analytical impedance can be easily formulated to take into account the effect of the next two higher order FW modes: $Z^{m_y=0} + Z^{FHM} + jX_{as}^{HM}$ where $Z^{FHM} = Z^{m_y=1} + Z^{m_y=-1}$. These terms can be calculated using (3.13). The new asymptotic term, X_{as}^{HM}, calculation is presented also in Appendix A and leads to:

$$X_{as}^{HM}(k_x) = \frac{\xi_0}{\pi}\left(\frac{k_0}{2} - \frac{k_x^2}{k_0(\varepsilon_r^d + \varepsilon_r^u)}\right)\left\{\ln\left(\frac{d_y}{2\pi w}\right) + \frac{3}{2} + \frac{d_y^2}{2w^2\pi^2}\left[\cos\left(\frac{2\pi w}{d_y}\right) - 1\right]\right\}. \tag{3.17}$$

Therefore, even in this case, the impedance remains fully analytical. Figure 3.6a shows the very good agreement of this new analytic impedance, $Z^{m_y=0} + Z^{FHM} + jX_{as}^{HM}$, represented with asterisks, with respect to (3.12).

In figure 3.8, the terms $Z - Z^{m_y=0}$, X_{as} and $Z^{FHM} + X_{as}^{HM}$ are shown as a function of the plane wave incident angle, for cases where the first higher order modes are relevant. We can see that equation (3.17) is able to recover the imaginary part of the total impedance. Therefore, Z_{rem} can be neglected for all cases of interest.

3.5.1 Lumped Equivalent Circuit

The dominant impedance terms, together with the current in the strips (3.11), suggest how to derive an equivalent circuit (shown in figure 3.9) that can be used to evaluate the absorbed power per unit length along the strip in each linear unit cell of dimension d_y. The circuit includes a voltage source, proportional to the projection of the component along the investigated strip (i.e. along x) of the incident electric field, the dynamic part of the impedance, $Z^{m_y=0}$, the inductive part of the impedance, $Z^{FHM} + jX_{as}^{HM}$, the remaining term, Z_{rem}, and the surface resistance of the absorber R_s/w.

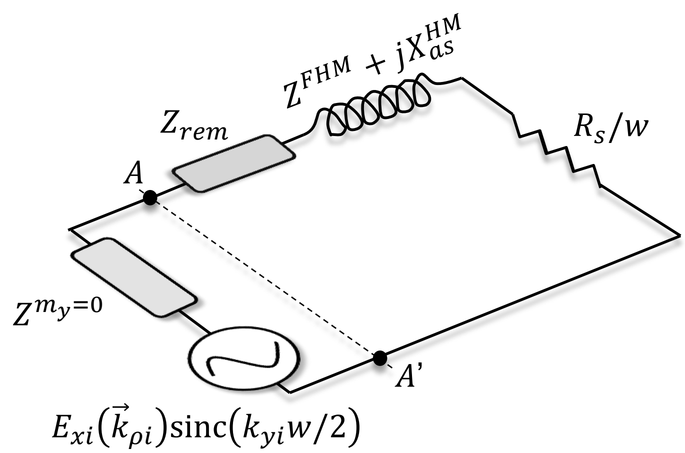

Figure 3.9: Lumped equivalent circuit of the absorber in the linear unit cell.

The circuit is easily divided in two parts: the right-hand side (RHS) with respect to terminals A$-$A$'$ represents the voltage drop due to the resistance and to the surroundings of the absorber, while the components on the left-hand side (LHS) account for the interaction of flowing current with the external world represented by the equivalent generator and the dynamic impedance.

3.6 Distributed Equivalent Network Representation

The equivalent circuit in figure 3.9 does not explicitly describe the relationship between the direct field and the electric currents of the strips. To introduce this relationship explicitly, we extend in this section the circuit of figure 3.9 into a rigorous equivalent network that also describes the entire field propagation starting from the direct plane wave.

3.6.1 Strip Current to FW Magnetic Field Transformer

The expression of $Z^{m_y=0}(k_x)$, (3.13), suggests that the fundamental term of the impedance can be thought of as the result of an impedance $G(k_x, k_{yi})$ transformed by a transformer with turns ratio $n = \mathrm{sinc}(k_{yi}w/2)/\sqrt{d_y}$ as in figure 3.10. Note that in figure 3.10 the ϕ-dependence of the impedance is explicitly expressed by using $k_x^2/k_\rho^2 = \cos^2\phi$, $k_y^2/k_\rho^2 = \sin^2\phi$ in (3.14).

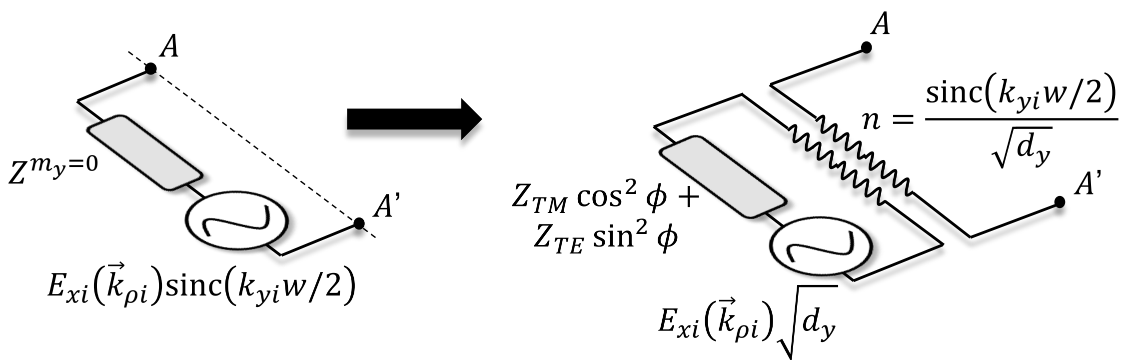

Figure 3.10: Separation of the part of the circuit that represents the incident field from the current in the absorber.

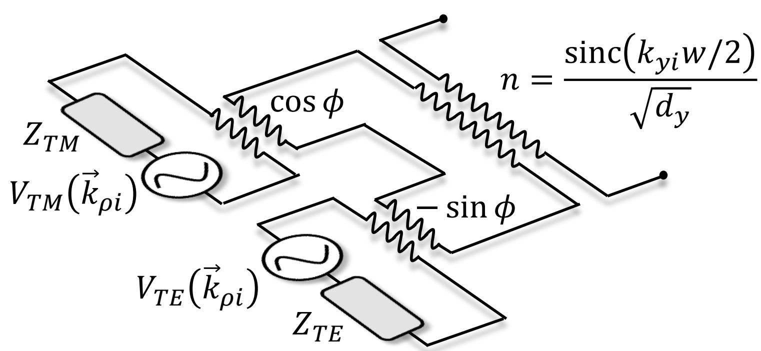

Figure 3.11: Separation of the TM and TE circuits components of the dominat FW.

The current flowing in the sheet resistance (RHS of circuit in figure 3.9) is not modified by this circuit operation, provided that the incident electric field is now multiplied by $\sqrt{d_y}$ which accounts for the projection of the incident field in the dominant FW ($m_y = 0$). As a result of the introduction of this transformer, the current in the LHS of the circuit in figure 3.10 represents the amplitude of the total (incident plus scattered) magnetic fields associated with the dominant FW. Accordingly, also the voltage at the LHS represents the amplitude of the total electric fields associated with the dominant FW.

3.6.2 TE and TM Generator

It is convenient to further express the LHS of the circuit as the series of TE and TM circuits that take into account separately for the two TE and TM components of the dominant FW. This superposition can be seen as the series connection of two transformers, with turns ratio $n_{TM} = \cos\phi$ and $n_{TE} = -\sin\phi$, connected to separate TE and TM loads as in figure 3.11. The complete network of the problem under analysis is shown in figure 3.3.

Apart from the introduction of the transformers n_{TM} and n_{TE}, the main difference between circuit in figure 3.11 and the one in figure 3.10 is the appearance of two equivalent TE and TM generators. Their introduction follows the representation of the incident electric field $\vec{e}^{\,i}$, as a function of the direct field by using a standard transverse (with respect to z) TE and TM fields. In a realistic situation the knowledge of the voltage sources representing the incident field will not be straightforward. In fact, the absorbing strips will be embedded in a dielectric and metallic stratified configuration. The cumulative effects of the multiple reflections defines the eventual incident field, $\vec{e}^{\,i}$, which must be expressed as a function of the given direct field $\vec{e}^{\,dir}$. Accordingly, it is convenient to express the incident fields in terms of the direct fields by means of an equivalent TE and TM transmission line network that represents the stratification. To this end, since the absorber is periodic along y, it is useful to introduce the fundamental Floquet mode basis vectors $\vec{e}_{TM}$ and $\vec{e}_{TE}$ to represent both the direct and incident plane waves:

$$\vec{e}_{TM} = \frac{1}{\sqrt{d_y}}(\cos\phi\;\hat{x} + \sin\phi\;\hat{y})e^{j\vec{k}_{\rho i}\cdot\vec{\rho}} \tag{3.18}$$

$$\vec{e}_{TE} = \frac{1}{\sqrt{d_y}}(-\sin\phi\;\hat{x} + \cos\phi\;\hat{y})e^{j\vec{k}_{\rho i}\cdot\vec{\rho}} \tag{3.19}$$

In this basis, the transverse components of the incident field can be expressed as:

$$\vec{e}_{tr}^{\,i}(\vec{k}_{\rho i}, \vec{\rho}, z=0) = V_{TM}(\vec{k}_{\rho i}, z=0)\vec{e}_{TM} + V_{TE}(\vec{k}_{\rho i}, z=0)\vec{e}_{TE}. \tag{3.20}$$

The circuit in figure 3.10 requires the knowledge of the term $E_{ix}(\vec{k}_{\rho i})$, which can be evaluated resorting to

$$\vec{e}_{tr}^{\,i}(\vec{k}_{\rho i}, \vec{\rho}, z=0)\cdot\hat{x} = e^{-j\vec{k}_{\rho i}\cdot\vec{\rho}}E_{ix}(\vec{k}_{\rho i}) = \frac{1}{\sqrt{d_y}}e^{-j\vec{k}_{\rho i}\cdot\vec{\rho}}(V_{TM}(\vec{k}_{\rho i})\cos\phi - V_{TE}(\vec{k}_{\rho i})\sin\phi). \tag{3.21}$$

Consequently, the equivalent voltage generator can be expressed as follows:

$$E_{ix}(\vec{k}_{\rho i})\sqrt{d_y} = V_{TM}(\vec{k}_{\rho i})\cos\phi - V_{TE}(\vec{k}_{\rho i})\sin\phi \tag{3.22}$$

where V_{TM} and V_{TE} are the two voltage sources in the circuit of figure 3.11. The expressions of these voltages can be calculated by using the equivalent transmission line shown in figure 3.4. They are the open circuit solution of the transmission line representation of the stratification at the strip array location, i.e. $V_{TM}(\vec{k}_{\rho i}) = V_{TM}(\vec{k}_{\rho i}, z = 0)$ and $V_{TE}(\vec{k}_{\rho i}) = V_{TE}(\vec{k}_{\rho i}, z = 0)$.

The direct field equivalent TE and TM sources are specified as follows:

$$V_{TM}^{+}(z) = \int_{-d_y/2}^{d_y/2} \vec{e}^{\ dir}(\vec{k}_{\rho i}, \vec{\rho}, z) \cdot \vec{e}_{TM}(\vec{k}_{\rho i}, \vec{\rho})dy \tag{3.23}$$

$$V_{TE}^{+}(z) = \int_{-d_y/2}^{d_y/2} \vec{e}^{\ dir}(\vec{k}_{\rho i}, \vec{\rho}, z) \cdot \vec{e}_{TE}(\vec{k}_{\rho i}, \vec{\rho})dy \tag{3.24}$$

Note that these voltages have unit of $\mathrm{V}/\sqrt{\mathrm{m}}$. The incident field can then be represented using the TE and TM voltages. This choice is made so that the current flowing in the circuit in figure 3.9 has the dimensions of Ampere.

The complete network of figure 3.3 is analytical and rigorously connects the direct fields to the electric currents in the absorber.

3.7 Use of the Equivalent Network

3.7.1 Power Absorbed per Unit Length in a Linear Unit Cell

The power absorbed per unit length along the strip in each linear cell (d_y) of the periodic array can be obtained directly from the equivalent circuit as

$$P_{abs}^{\Delta x, d_y} = \frac{1}{2}|\tilde{I}(\vec{k}_{\rho i})|^2 \frac{R_s}{w} \tag{3.25}$$

where $P_{abs}^{\Delta x, d_y}$ has unit of W/m. Once the absorbed power is calculated, it is straightforward to get the absorbing efficiency (η) by normalizing it with the incident power. The incident power per unit length in a linear unit cell can be calculated directly from the direct field as the sum of the TE and TM contributions:

$$P_{in}^{\Delta x, d_y} = P_{in}^{TM} + P_{in}^{TE} = \frac{1}{2}\frac{|V_{TM}^{+}|^2}{Z_{TM}} + \frac{1}{2}\frac{|V_{TE}^{+}|^2}{Z_{TE}}. \tag{3.26}$$

The efficiency for the cases studied in Section 3.3 and 3.4, obtained analytically from the equivalent circuit, is shown in figure 3.12 for normal incidence. These curves are validated with full wave simulations in CST, showing a good agreement.

From figure 3.12, one can observe that, for TiN absorbers in case I., a frequency bandwidth of about one octaves for efficiencies above 90% can be obtained. A similar bandwidth is obtained for case III. with a silicon backshort. Instead, if the backshort is made of air, the frequency bandwidth is increased up to 2.6 octaves. A similar frequency bandwidth is achieved for the Al based absorber in case III. If one is willing to accept absorption efficiencies down to 75%, the TiN absorber in case II. presents the largest absorption band. The analytical model of the efficiency has also been validated with full wave simulations as a function of the plane wave incident angle in figure 3.13.

3.7.2 Power Absorbed in a Finite Array

In a realistic finite absorber, the current can be assumed to be unperturbed by the truncation of the strips and their finite number because of the strong losses. In this case the total power absorbed over an area $L_x \times L_y$, can be evaluated as

$$P_{abs}(k_{\rho i}, L_x, N) = \frac{R_s}{2w}\sum_{n=-N/2}^{N/2}\int_{-L_x/2}^{L_x/2} |i(x, \vec{k}_{\rho i})|^2 dx \tag{3.27}$$

where $N = L_y/d_y$. According with equation (3.10):

$$P_{abs}(k_{\rho i}, L_x, N) = \frac{1}{2} L_x N |\tilde{I}(\vec{k}_{\rho i})|^2 \frac{R_s}{2w} \tag{3.28}$$

3.7.3 TE-TM Coupling

The circuit in figure 3.2 would describe the coupling between the fundamental TE and TM FW via a Black Box representation. The equivalent network in figure 3.3 explicitly shows the mechanism of this coupling. A TM incident FW magnetic field excites a current in the strips. This current is bound to flow in both TE and TM transformers, and thus it necessarily induces some TE magnetic fields in the surrounding of the periodic structure.

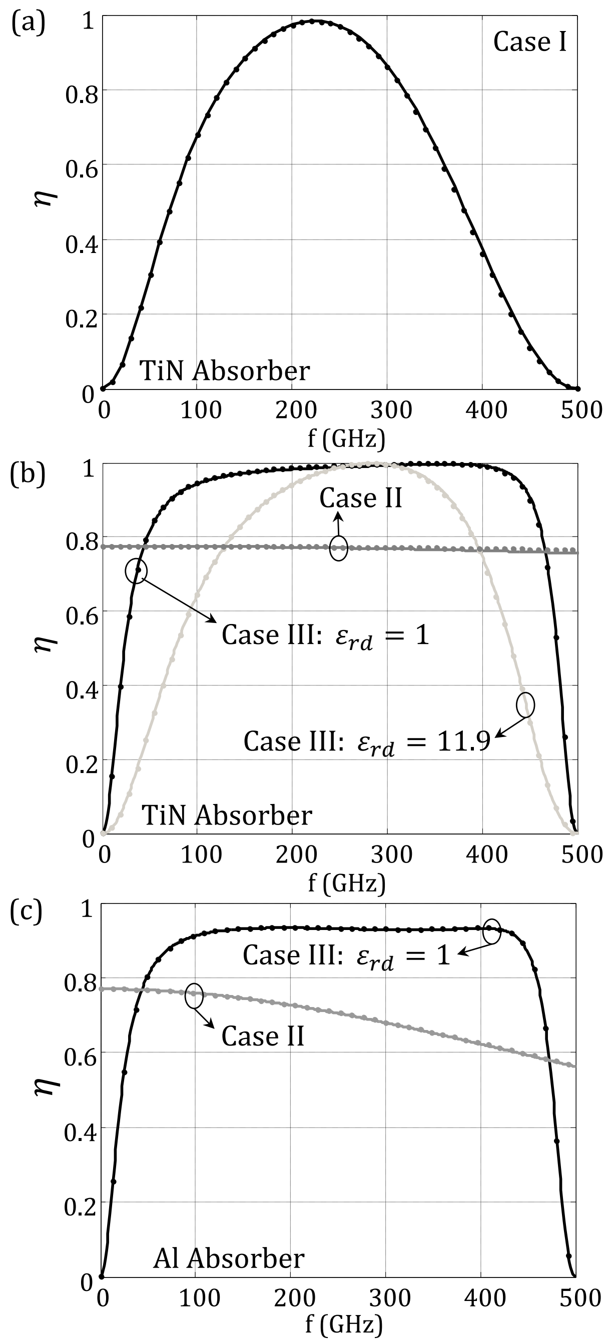

Figure 3.12: (a), (b) and (c) efficiencies for normal incidence relevant to the designs considered in figures 3.6a, 3.6b and 3.7, respectively, versus frequency. The solid lines are the analytical results and the dots represent CST simulations.

Only in the principal planes the TE and TM modes are decoupled. Figure 3.14a shows the TM-TM and TE-TE reflection coefficients, for the same cases addressed in figure 3.13,

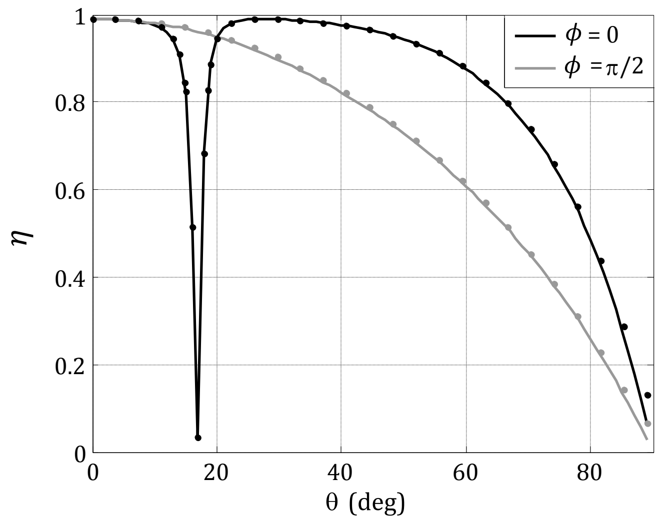

Figure 3.13: Efficiency of the TiN design for the case III with $\varepsilon_{ru} = 11.9$ and $\varepsilon_{rd} = 1$ (same geometry than in figure 3.6b) as a function of the incident θ angle, for the two principal planes and for $f = 250$ GHz. The solid lines are the analytical results and the dots represent CST simulations.

calculated in the upper transmission line of the network shown in figure 3.3, validated with CST. Figure 3.14b shows the coupled reflections TE-TM in the same cases for diagonal incidence.

3.8 Conclusions

A Green's function based equivalent network for the analysis of linearly polarized absorbers under general plane wave incidence has been presented. The networks main achievement with respect to previous networks is the separate treatment of the average field in the absorbers plane and the electric current in the lossy strips. This is obtained via the introduction of ad hoc transformers. A second achievement is the validity of the network in situations where higher order modes play a significant role. A third achievement is that the equivalent network allows the assessment of the coupling between TE and TM waves. Finally the network is also extremely simple to use since all the components are obtained analytically. Apart from characterization advantages, each of the network's components is associated with a specific physical mechanism, thus the dimensioning of the absorber is simplified by physical insight. The network introduced here has been used to design optimized absorber geometries for THz KID detectors showing efficiencies larger than 90% over a bandwidth of up to 2.6 octaves.

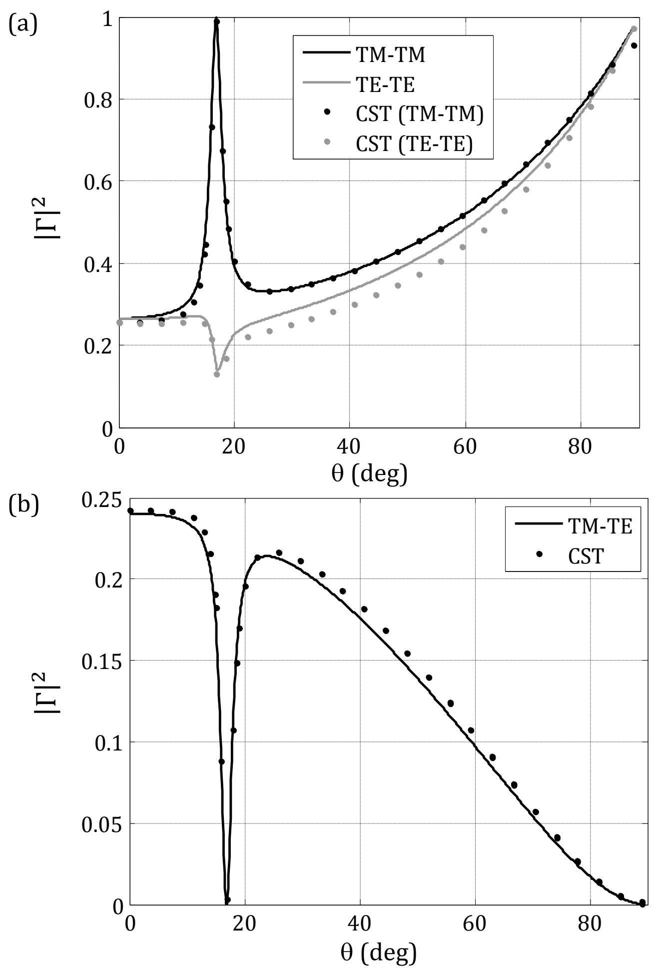

Figure 3.14: Coupled reflections for the TiN design for the case III with $\varepsilon_{ru} = 11.9$ and $\varepsilon_{rd} = 1$ (same geometry than in figure 3.6b) as a function of the incident θ angle in the diagonal plane ($\phi = \pi/4$), for $f = 250$ GHz.

Chapter 4

Analysis of Distributed Absorbers under THz Focusing Systems

4.1 Introduction

The next generation of terahertz (THz) instruments for space imaging requires arrays of thousands of detectors located in the focal plane of a telescope [116]. Kinetic Inductance Detectors have been proposed for space imaging because, as mentioned in Chapter 1, they present and unprecedented intrinsic read-out, which derives from the possibility of using frequency multiplexing techniques.

In this chapter, the coupling between focusing systems and linearly polarized absorbers (see figure 4.1), embedded in a generic multi-layer dielectric structure, is investigated by using the analytical spectral model based on FO derived in Chapter 2 coupled with the equivalent network representation derived in Chapter 3. The proposed method is able to analytically and efficiently characterize the power captured by distributed absorbers located under focusing systems, also with small F/D ratios, and printed on a multilayer dielectric structure.

Two cases are taken as reference: a free-standing absorber under a parabolic reflector and an absorber under a dielectric elliptical lens. The method shows that the power captured by free-standing absorbers varies smoothly with large F/D ratios as expected. On the contrary, when dense lenses are present , the absorbed power shows a surprising dependence from the geometrical parameters. Even so, absorbers under dense lenses can show higher efficiencies over wide frequency bands than free-standing ones. The method

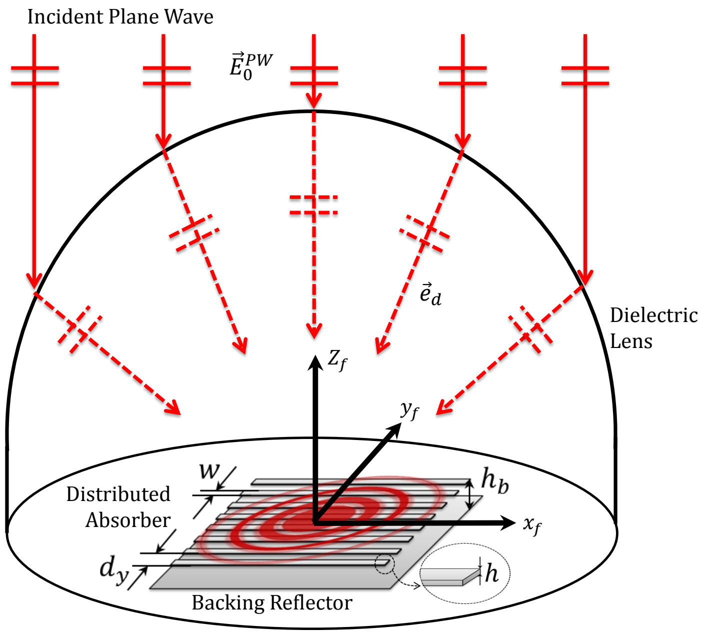

Figure 4.1: Linearly polarized absorber placed at the focal plane of a focusing system.

is validated with full-wave time-consuming simulations.

4.2 Absorber Current Induced by a General Field Configuration

KIDs based on absorbers can be modeled as a series of parallel and infinitely long absorbing strips with a width w, as explained in Chapter 3. The strips are periodically and tightly arranged, with period d_y. Figure 4.1 shows the geometry of the absorbers hosted in the focal plane of a dielectric lens and kept at a finite distance from a backing reflector. The absorbed power can be calculated over a finite area, once the current flowing on the strips is known.

In Chapter 3, an analytical equivalent circuit that allows calculation of the current at the cross section x, $i_n(x_f, ndy) = I_0(k_{xi}, k_{yi})e^{-jk_{xi}x_f}e^{-jk_{yi}y_f}$, which is induced in each of the n-strip when the absorber is illuminated by a *direct* plane wave $(E_d(k_{xi}, k_{yi}))$, has been discussed. The direct field is represented as a superposition of two TM and TE impinging voltage waves, see figure 4.2, of amplitude $V^+_{TM}(k_x, k_y)$ and $V^+_{TE}(k_x, k_y)$, respectively. The derivation of these TE and TM sources was also described in the previous chapter and can

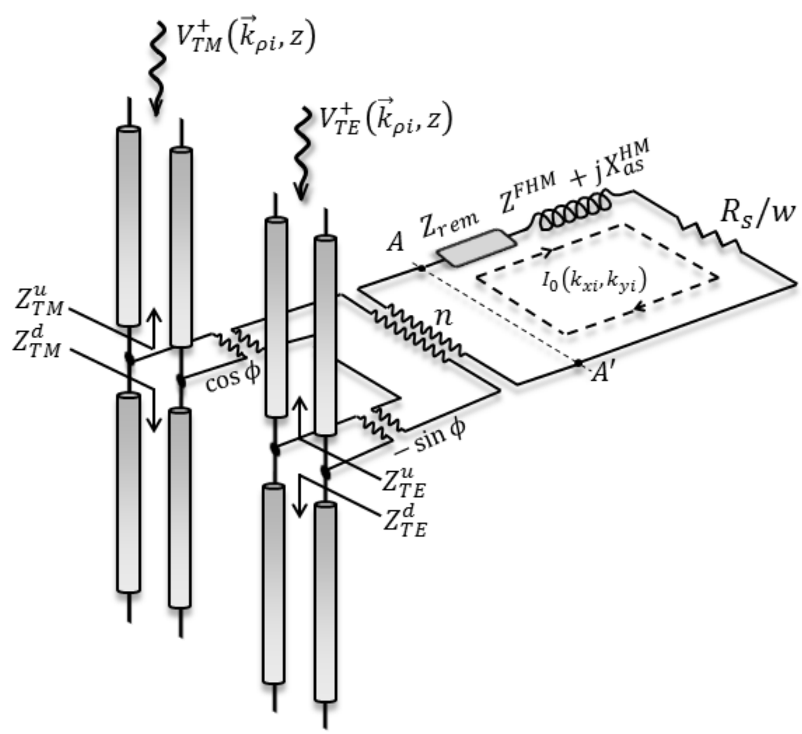

Figure 4.2: Equivalent network developed for the characterization of the interaction of a plane wave impinging in a linearly polarized absorber. Each component of the circuit is defined in Chapter 3.

be rewritten as:

$$V_{TM}^{+}(k_x, k_y) = \sqrt{d_y}\vec{E}_d(k_x, k_y) \cdot \hat{\rho}, \tag{4.1}$$

$$V_{TE}^{+}(k_x, k_y) = \sqrt{d_y}\vec{E}_d(k_x, k_y) \cdot \hat{\phi}. \tag{4.2}$$

The solution of the equivalent network gives

$$I_0(k_{xi}, k_{yi}) = \operatorname{sinc}\left(\frac{k_{yi}w}{2}\right) \frac{E_{ix}(k_{xi}, k_{yi})}{Z(k_{xi}) + \frac{R_s}{w}}, \tag{4.3}$$

where $Z(k_{xi})$ is defined in Chapter 3, R_s is the sheet resistance (Ω/sq), and $E_{ix}(k_{xi}, k_{yi})$ represents the amplitude of the x-component of the incident electric field calculated at the strip position in absence of the absorber, but including any possible dielectric stratification where the absorber is embedded. This field is expressed as the voltage in A-A', see figure 4.2, superposition of the fields induced by both TE and TM direct voltage waves. Note that the *incident* field, $\vec{E}_i$, is different from the *direct* field, $\vec{E}_d$, as it accounts for the presence of possible the dielectric stratifications, as explained in Chapter 3.

When the absorber is illuminated by a generic coherent field (e.g. the field in the focal plane of a focusing system), the direct electric field $\vec{e}_d(\vec{\rho}_f)$ (i.e. in absence of absorber and the stratification) can be expressed as a coherent superposition of plane waves, as explained in Chapter 2:

$$\vec{e}_d(\vec{\rho}_f) = \frac{1}{4\pi^2} \int_{-\infty}^{+\infty} \int_{-\infty}^{+\infty} \vec{E}_d(k_{xi}, k_{yi}) e^{-jk_x x_f} e^{-jk_y y_f} dk_x dk_y, \tag{4.4}$$

In the following we will refer to $\vec{E}_f$ rather than $\vec{E}_d$, to highlight our present attention on focusing systems. This plane wave expansion is particularly useful when used in combination with the circuit derived in Chapter 3.

Thanks to the linearity of the system, the total current in the n-th strip of the absorber, $i_n(x_f, nd_y)$, can be expressed as the superposition of the currents induced by each of these plane waves, as follows:

$$i_n(x_f, nd_y) = \frac{1}{4\pi^2} \int_{-\infty}^{+\infty} \int_{-\infty}^{+\infty} I_0(k_x, k_y) e^{-jk_x x_f} e^{-jk_y n d_y} dk_x dk_y \tag{4.5}$$

where $I_0(k_x, k_y)$ is calculated by (3.11). The power absorbed by the strips can now be easily calculated from (4.5) using the sheet resistance, R_s. For a finite absorber of dimensions $L_x \times L_y$, the power absorbed can be approximated as a summation over a finite number of cells ($N = \lceil l_y/d_y \rceil$) as follows

$$P_{abs}(L_x, N) = \frac{R_s}{2w} \sum_{n=-N/2}^{N/2} \int_{-L_x/2}^{L_x/2} |i_n(x_f, nd_y)|^2 \, dx_f \tag{4.6}$$

Expressions (4.5) and (4.6) highlight that, the coherent summation of the current induced by each of the plane waves is needed to evaluate the total power absorbed. In some cases this coherent summation operation can be simplified. That is, if the array is very well sampled and occupies a region significantly larger than the region in which the direct field is significant. In such configuration, the spatial integral and the summation in (4.6) can be extended to infinity without making a significant error. The power can then be calculated resorting to the Parseval's Theorem, as follows

$$P_{abs} \simeq \frac{R_s}{2w} \frac{1}{d_y} \frac{1}{4\pi^2} \int_{-\infty}^{+\infty} \int_{-\infty}^{+\infty} |I_0(k_x, k_y)|^2 \, dk_x dk_y \tag{4.7}$$

In this case the power is proportional to the incoherent weighed sum of the power associated to each plane wave separately. It is worth noting that, in all practical applications, since no evanescent waves reach the absorber surface, the integrals in (4.7) are spectrally limited. If one names $k_\rho = \sqrt{k_x^2 + k_y^2}$, $k_{\rho 0} < k_0 \sin\theta_0$ defines such limit, where k_0 is the free space wavenumber and θ_0 is the subtended rim angle of the focusing system in figure 2.2. The integration domain can be further reduced when FO plane wave expansion is used as shown in Chapter 2. In the next section, the coupling of a distributed absorber with a parabolic reflector and elliptical lens is investigated in detail by evaluating the analytical expression of the direct field PWS.

4.3 Canonical Geometries

In this section, we explicitly derive the expressions of the PWS for two canonical geometries: a parabolic reflector and an elliptical dielectric lens, by using the method explained in Chapter 2. We consider a plane wave incidence into these focusing systems from broadside with a linear polarization along x and an amplitude E_0^{PW}.

4.3.1 Parabolic Reflector

Figure 4.3 shows the geometrical parameters together with the FO equivalent surface for a parabolic reflector. In this configuration, the equivalent surface, S, touches the reflector surface in the apex. Thus the sphere radius is equal to the focal distance, i.e. $R = F$. A parametrization of the integral in (2.2) in terms of (θ, ϕ) associates every point, $\vec{r}$, on the surface S to a ray with propagating vector $\hat{k} = -\vec{r}$, where $\hat{r}$ is the radial unit vector. Each ray has undergone a reflection at the reflector's surface (see the inset of figure 4.3 for a visual clarification).

For a linearly polarized plane wave coming from broadside, the parallel and perpendicular unit vectors of the reflected fields coincide with the spherical unit vectors components, $\hat{e}_r^{||}(\theta, \phi) = \hat{\theta}$ and $\hat{e}_r^{\perp}(\theta, \phi) = \hat{\phi}$. At S, the PO aperture field (i.e. the reflected field) is a local plane wave and its explicit expression becomes:

$$\vec{e}_s(\theta, \phi) = -S^r_{pread}(\theta)(\cos\phi\hat{\theta} - \sin\phi\hat{\phi})E_0^{PW}. \tag{4.8}$$

where the spreading term, $S^r_{pread} = 1/\cos^2(\theta/2)$, accounts for the conservation of energy in the ray path from the incidence plane to the reference sphere. The spreading term is

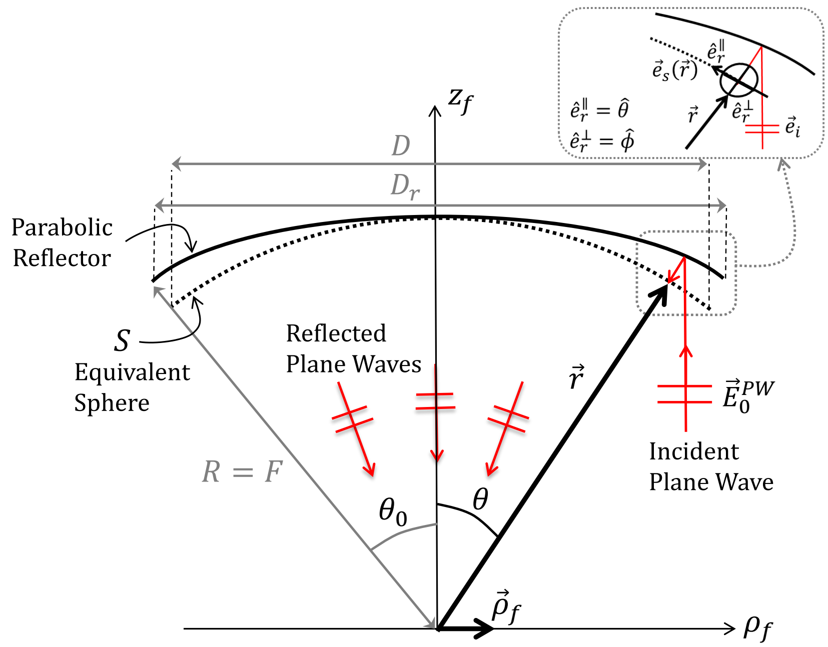

Figure 4.3: Equivalent sphere and geometrical parameters for a parabolic reflector.

calculated by imposing that the power density within the solid angle has to be equal to the power density reflected by the parabola. It is worth noting that the electric fields are all in phase at the equivalent sphere. The integral in (2.2) can be performed analytically for large R/D giving rise to the well-known Airy pattern, defined as:

$$\vec{e}_f(\vec{\rho}_f) = -\frac{jkRe^{-jkR}}{2\pi}A(\rho_f)\hat{x} \tag{4.9}$$

where

$$A(\rho_f) = \frac{\pi D^2}{2R^2}\frac{J_1(k\rho_f D/(2R))}{k\rho_f D/(2R)}. \tag{4.10}$$

In a general case, so when R/D is not too large, the integral along ϕ can be performed analytically using the integral representation of Bessel functions [117].

Finally a Fourier Transform representation of the focal field, (2.9), can be obtained by using the PWS for a normally illuminated parabolic reflector as:

$$\vec{E}_f(k_x, k_y) = -\frac{4\pi kRE_0^{PW}e^{-jkR}}{k_z}\frac{1}{k+k_z}\left(\frac{k_x}{k_\rho}\hat{\theta} - \frac{k_y}{k_\rho}\hat{\phi}\right) circ(k_\rho, k_{\rho 0}). \tag{4.11}$$

where $k_z = \sqrt{k^2 - k_\rho^2}$.

Equation (2.2) with (4.8) and (4.11) highlight the representation of the field in the focal plane is represented as a sum of plane waves whose propagation directions are defined as those of the rays traveling from the reflector to the observation points. Accordingly, the PWS is limited to a spectral region defined by the parametrization of the reflector: $\theta \in (0, \theta_0)$. Figure 4.4 shows the co-polar component of the electric field in the focal plane of a reflector characterized by R/D = 3 evaluated resorting to FO, a standard PO (GRASP software [75]) and the Airy pattern expression. For these large R/D cases, the focal fields resemble the Airy pattern. The results are presented for reflectors diameters of 20λ and 70λ highlighting the respective FO domains of applicability. As it can be seen from figure 2.3a in Chapter 2, the integrand is limited by an amplitude error for the small diameter, whereas by the phase error for the larger diameter. As observed in figure 4.4, the limit of applicability for the smaller diameter indicates an error in the amplitude larger than 0.15 dB, whereas the phase has an error smaller than 12°. Instead, the amplitude error in the larger diameter is negligible (< 0.02 dB), whereas the phase error is larger than 25°. Therefore, the amplitude and phase applicability regions carried out for the argument of (2.7) are well translated in the same amplitude and phase applicability regions of the focal plane field.

4.3.2 Elliptical Dielectric Lens

A similar PWS spectrum can be obtained for an elliptical dielectric lens. Such lens has perfect focusing properties when its eccentricity is characterized by $e = 1/\sqrt{\varepsilon_r}$, with ε_r being the lens relative dielectric constant. Figure 4.5 shows the lens geometry and the equivalent sphere, S, used for the FO calculation. Note that S touches the lens only in correspondence of its rim. Therefore, in this case, $R \neq F$:

The procedure to calculate the FO plane wave spectrum is analogous to the one described in the previous section, with the main difference being the expression for the field tangent to the sphere as follows:

$$\vec{e}_s(\theta, \phi) = S^l_{pread}(\theta)(\tau_\parallel(\theta)\cos\phi\hat{\theta} - \tau_\perp(\theta)\sin\phi\hat{\phi})E_0^{PW}, \tag{4.12}$$

where $\tau_\parallel(\theta)$ and $\tau_\perp(\theta)$ are the parallel and perpendicular transmission Fresnel coefficients. The transmission and reflection coefficients for a normally incident plane wave can be evaluated once it is recognized that the normal to the ellipse is $\hat{n} = ((\cos\theta - e)\hat{z} +$

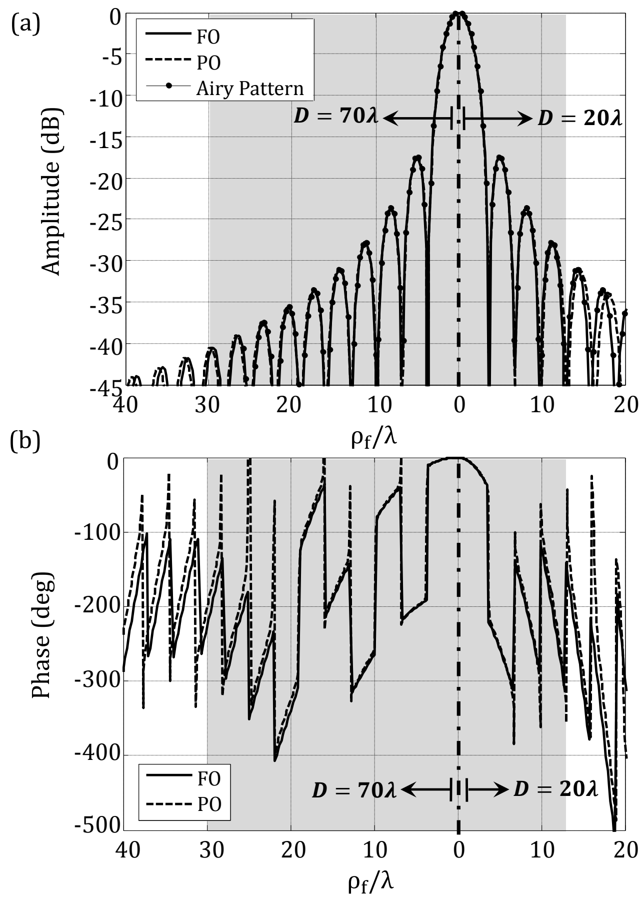

Figure 4.4: Focal plane fields of $R/D = 3$ reflectors with two different diameters, $D = 20\lambda$ (right side of the figures) and $D = 70\lambda$ (left side of the figures), calculated using FO and compared with a normal PO (GRASP simulations) and with the well-known Airy pattern: (a) amplitude and (b) phase. The validity region is highlighted in grey. The fields are practically symmetric in ϕ so only one of the main planes ($y = 0$) are shown.

$\sin\theta\hat{\rho})/\sqrt{1+e^2-2e\cos\theta}$. Moreover, the spreading function is calculated by imposing the power density within the solid angle has to be equal to the power density transmitted by the lens:

$$S^l_{pread} = \frac{c(1-e^2)}{e(1-e\cos\theta)}\frac{1}{R} \tag{4.13}$$

with c being half of the distance between the two foci of the ellipse. It is worth noting that when the eccentricity of the lens tends to zero the surface degenerate to a sphere, and $S^l_{pread}(\theta) = \sqrt{\cos\theta}$.

Therefore, the lens focal plane field can be approximated as a plane wave expansion, as

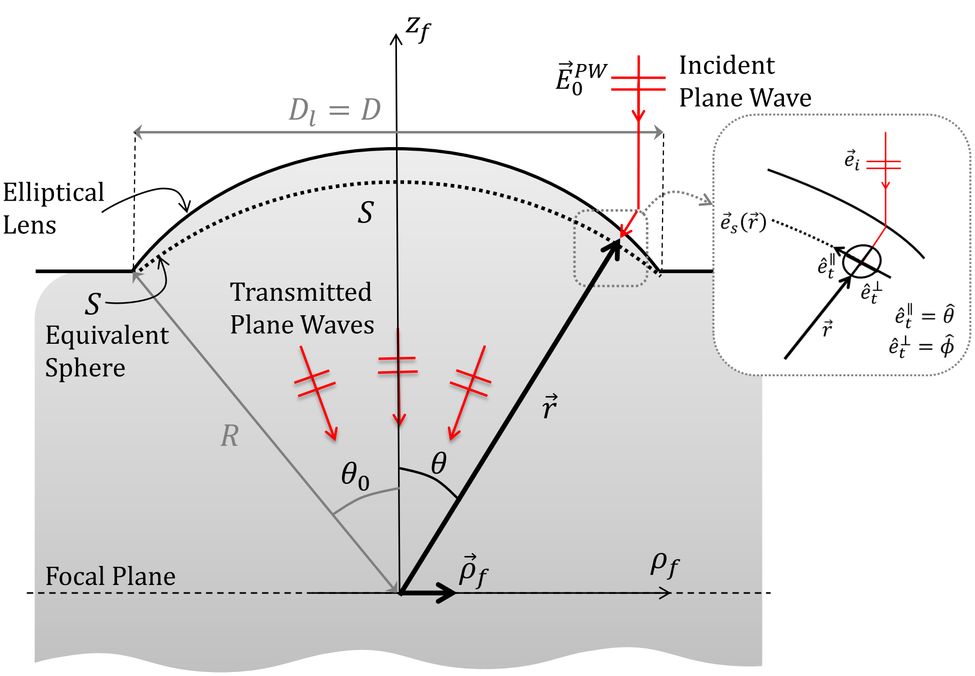

Figure 4.5: Equivalent sphere and geometrical parameters for an elliptical lens.

in the previous section, using

$$\vec{E}_f(k_x, k_y) = \frac{j2\pi E_0^{PW} e^{-jkR}}{k_z} \frac{c(1-e^2)}{e(1-e\cos\theta)} \left(\tau_{\parallel}(\theta)\frac{k_x}{k_\rho}\hat{\theta} - \tau_{\perp}(\theta)\frac{k_y}{k_\rho}\hat{\phi} \right) circ(k_\rho, k_{\rho 0}). \quad (4.14)$$

where $\theta = \sin^{-1}(k_\rho/k)$.

Figure 4.6 shows the co-polar component of the electric fields in the focal plane of a $6\lambda_0$ diameter elliptical silicon ($\varepsilon_r = 11.9$) lens with $R/D = 0.6$ evaluated by resorting to FO, a standard PO, and the Airy pattern expression. As described by figure 2.3b in Chapter 2, this case is limited by the phase error ($< 25°$). It is worth noting that for this small R/D case, the focal fields differ significantly from the Airy pattern.

4.4 Numerical Examples

In this section we proceed to investigate the performance of distributed absorbers under focusing systems. Specifically, we start by observing the spatial current distribution on the strips when the absorber is located under a silicon elliptical lens. The separation

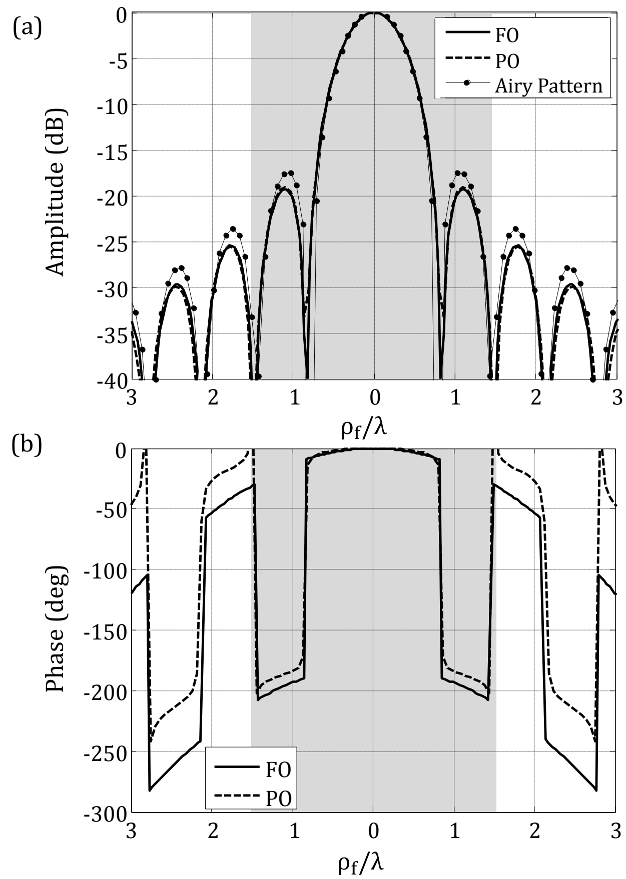

Figure 4.6: Focal plane fields of an $R/D = 0.6$ elliptical silicon lens, with $D = 20\lambda = 6\lambda_0$, calculated using FO and compared with a normal PO and with the well-known Airy pattern: (a) amplitude and (b) phase. The validity region is highlighted in gray. The field is symmetric in ϕ so only one of the main planes ($y = 0$) are shown.

layer between the absorber and the backing reflector is filled either via a silicon slab or a free space. The optimum absorber parameters are designed as explained in Chapter 3. Figure 4.7 shows the distribution of the current along the central strip calculated with (3.10) for two different R/D cases very close one to each other. Specifically, we assume $D = 20\lambda = 6\lambda_0$ and we consider $R/D = 1.6$ ($\theta_0 = 18°$) for the first case, while $R/D = 1.8$ ($\theta_0 = 16°$) for the second. For both cases, the observation ranges shown in figure 4.7 fall within the FO applicability region. The largest part of the power (95%) is contained within the main lobe and the first two secondary lobes. This is the most significant area when calculating the absorbed power. In the case of a reflector characterized by $R/D = 1.8$, the plane waves impinging on the absorber form, with respect to the focal plane normal (the z_f axis in figure 4.5), an angle smaller than the critical angle $\theta_c = 16.85°$ between silicon and free space. Conversely, for $R/D = 1.6$ ($\theta_0 = 18°$) the plane waves arriving to the absorber from the edge of the lens impinge with an angle larger than the critical angle. As can be observed from a comparison between figure 4.7a and b, the two R/D produce appreciably different currents where free space backshort is present, despite the fact that they are associated to almost the same R/D (see the insets in figure 4.7). This difference is associated to the effect of the critical angle.

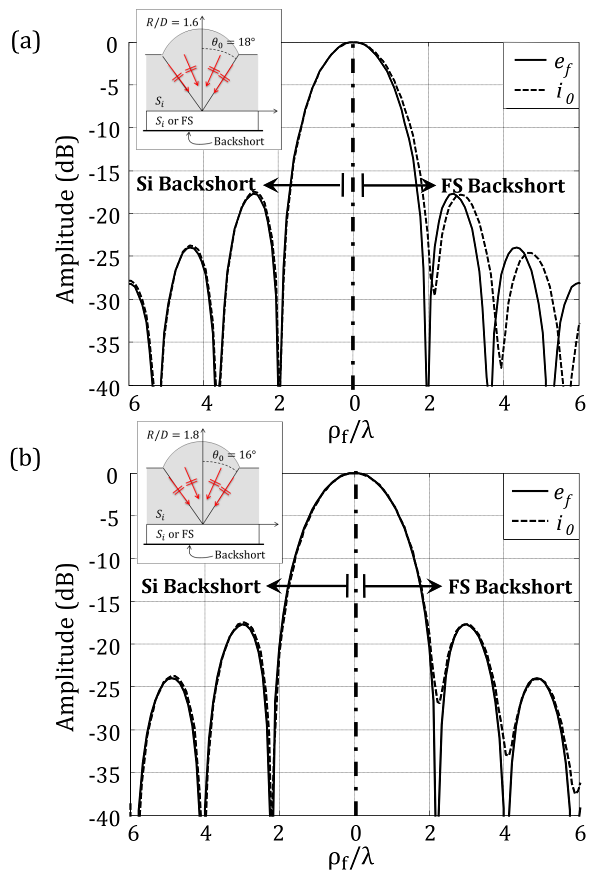

Figure 4.7: Currents in the absorber central strip, at 250 GHz, for (a) $R/D = 1.6$ and (b) $R/D = 1.8$ silicon elliptical lenses with $D = 7.2mm$. In both figures, the right side represents the backshort obtained via free space (FS) and, the left side, obtained via a silicon slab. The normalized focal plane field is also shown. Absorber geometry: $d_y = 75\mu m$ and $w = 20\mu m$, and sheet resistance $R_s = 30\Omega$. The insets show a drawing of the analyzed lens configuration.

This effect can be appreciated thanks to the fact that the analytical tool presented here links the focusing system with the spectral Green's function of planar dielectric stratified media. To highlight this effect, figure 4.8 shows the variation of the spectral current, (3.9), normalized to its maximum value for the same two cases of figure 4.7 at two different frequencies. The peak around $k_{xi} = 0.29k$ is associated to the critical angle present only in the case of free space backshort. The effect of the critical angle is also present on the incident field, calculated in the absence of the absorber, as shown in the right axis of figure 4.8.

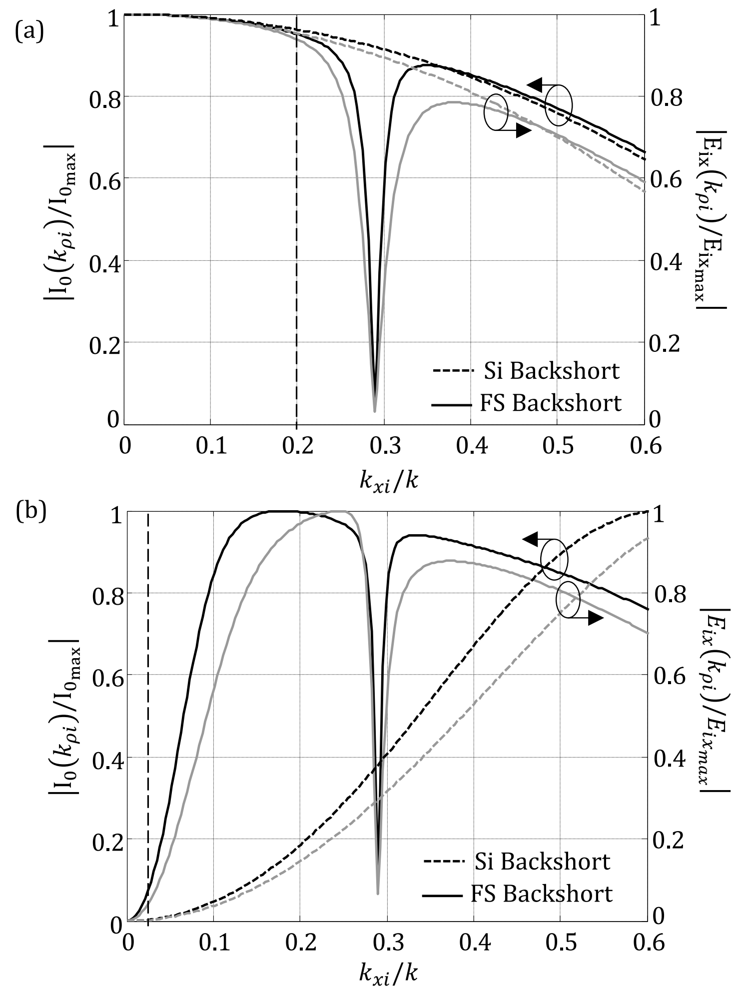

Figure 4.8: Normalized current, black lines and left axis, and normalized incident field, gray lines and right axis, as a function of k_{xi}/k for $k_{yi} = 0$ for the same cases shown in figure 4.7. (a) $f = 250$ GHz and (b) $f = 500$ GHz.

4.4.1 Proportionality between Currents and Electric Fields

Figures 4.7a and b, also show the direct field coming from the focusing lens, normalized to its maximum value. In general, the shape of the spatial current differs from this field, since it depends on the integration of the spectral components of the direct field, the absorber equivalent circuit, and the effect of the dielectric stratifications on the incident field, as pointed in the previous section. However, a close observation of figure 4.7 suggests that, in some cases, the spatial distribution of the electric current and that of the focal direct field are essentially proportional one to the other, even for large ranges of observation. This occurs when the spectral variation of the current is small. Figure 4.8a shows this variation for the same case than figure 4.7 at 250 GHz. One can see that the variation as a function of k_{xi}/k is constant up to an angle of about 10°, i.e. $k_{xi}/k \approx 0.2$. However, if we go to a different frequency, figure 4.8b, the variation is constant only up to about 2°, i.e. $k_{xi}/k \approx 0.03$. Beyond these limits one cannot claim any sort of proportionality between the spatial current and direct fields without incurring in significant errors. In general, the limit will depend on the dielectric stratification in which the absorber is embedded and the frequency.

4.4.2 Simplified Model for Small Angular Regions

For cases with small variation of the direction of the incidence rays, it is useful to find a simplified expression to quantify the power absorbed using the previous proportionality between the currents and the direct field. To this regard, we can assume that $I_0(k_x, k_y) \approx I_0(0,0)$ in (3.10) and (4.6). Following several straightforward steps, one arrives to a simplified expression of the absorbed power:

$$P_{abs} = \frac{R_s}{2wd_y}|I_0(0,0)|^2 \frac{1}{4\pi^2} \int\int_{Abs_{Area}} |A(\rho_f)|^2 dx_f dy_f, \tag{4.15}$$

where $A(\rho_f)$ is defined in (4.10). The value of the spectral current at broadside, $I_0(0,0)$, can be evaluated in a generic dielectric stratification using the following expression:

$$|I_0(0,0)| = \left| \frac{E_f(0,0)S_{trat}}{Z(0) + R_s/w} \right| \tag{4.16}$$

where S_{trat} relates the incident voltage wave (V_{TM}^+) with the open circuit solution of the transmission line representation of the stratification at the absorber location (V_{TM} in Chapter 3). Therefore, S_{trat} depends on the specific stratification where the absorber is embedded. In the cases of figures 4.7 and 4.8, $S_{trat} = 1 + (Z^d - Z^u)/(Z^d + Z^u)$ where Z^u and Z^d are the input impedances of the upper and lower half spaces defined in figure 4.2 evaluated at broadside (i.e. $Z^{u/d} = Z_{TE}^{u/d} = Z_{TM}^{u/d}$).

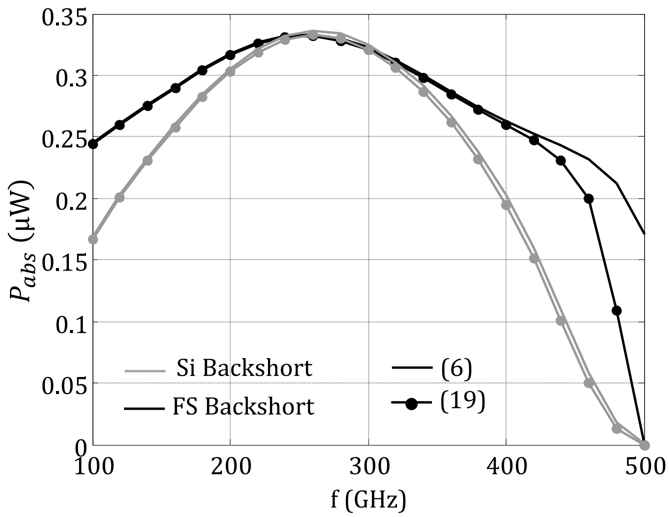

Figure 4.9: Analytical absorption efficiency calculated for the same cases of figures 4.7 and 4.8, but using a lens with $\theta_0 = 10°$.

Therefore, the integration of the spatial current distribution in (3.10) can be simplified into a spatial integration over the well-known Airy pattern distribution, leading to a much faster computation time. Figure 4.9 shows the calculated absorbed powers, using (4.6) and (4.9) for the same cases shown in figures 4.7 and 4.8, but using a lens with $\theta_0 = 10°$, as a function of the frequency. The agreement is very good except at the higher frequencies. For such frequencies, the proportionality between the spatial current and focal field is no more valid for the free space backshort. For this case, there is a significant variation of the spectral current in the angular range defined by the lens illumination (i.e. up to 10°) as shown in figure 4.8b.

4.4.3 Absorption Efficiency and Validation of the Model

In the general case, the absorption efficiency of a focusing absorbing system can be directly obtained using (4.6) and normalizing it by the power of the plane wave impinging on the focal system aperture (D_l in the case of the lens and D_r for the reflector) accordingly to figure 4.3 and 4.5. Figure 4.10 shows this efficiency for a large $R/D = 1$ and a small $R/D = 0.6$ elliptical lenses. In the large R/D case the presence of a matching layer, with thickness $\lambda/4$ at the central frequency of the band, is included. The same cases have been analyzed by using the CST software for comparison; the excellent agreement is evident. The CST computation is very time consuming (for the cases shown in figure 4.10 CST took over two hours in comparison of the analytical method that took less than a minute). Moreover, the computation time in CST increases with the dimensions of the lens. This is because CST requires a full wave simulation of the whole optical system (figure 4.11 shows the electric field inside the lens simulated by CST for the same $R/D = 0.6$ case of figure (4.10). The inset of figure 4.10 shows the normalized current, in the central strip of the absorber, validated with CST for the small R/D case at the central frequency.

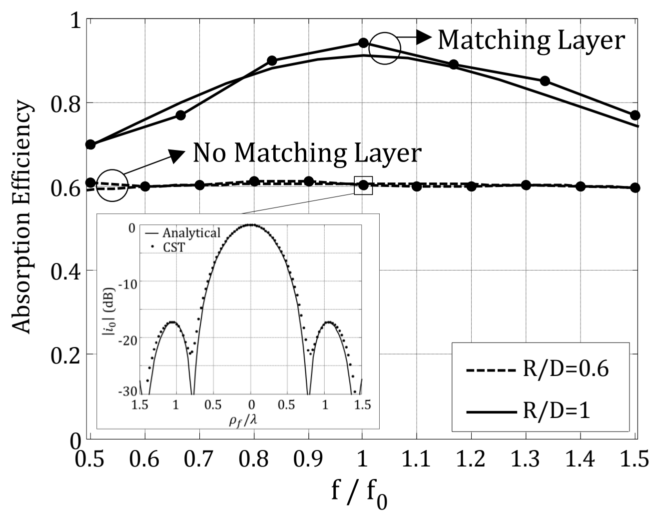

Figure 4.10: Analytical absorption efficiency validated with CST (lines with dots) for two lenses: $R/D = 1$ (dashed lines), with matching layer, $d_y = 20\mu m$, $w = 10\mu m$ and $R_s = 55\Omega$, and $R/D = 0.6$ (solid lines), without matching layer, $d_y = 75\mu m$, $w = 20\mu m$ and $R_s = 30\Omega$. In both cases $D = 20\lambda = 6\lambda_0$ and a backshort in free space is used located at $\lambda_0/4$ at the $f = f_0$. The inset shows the current in the absorber validated with CST for the $R/D = 0.6$ case at the $f = f_0$.

To evaluate the current along the strips, the proposed model assumes an infinite extension of the absorber. A finite absorber dimension is only considering in the calculus of the absorbed power, (4.6). This is equivalent to neglect the edge effects associated to the absorber finiteness. However, these effects are usually very small, in practice, because of the significant loss in the metal strips. In order to study the validity of the approximation, figure 4.12 shows the absorption efficiency for different dimensions of the absorber, for the case $R/D = 0.6$ in figure 4.10, validated with CST. The absorber areas considered, apart from the infinite case, are those that sample the main lobe and half the main lobe of the field at the central frequency. It can be observed that the agreement is excellent except for the smallest area. Indeed, this case has an absorber dimension of only 0.6λ at the central frequency.

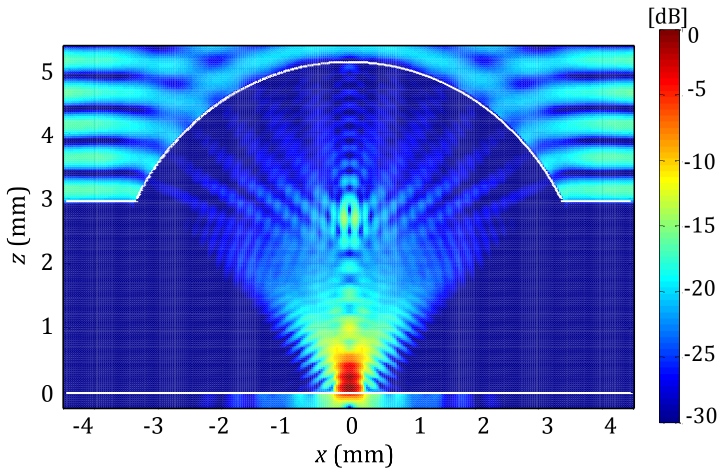

Figure 4.11: Electric field amplitude for the $R/D = 0.6$ lens case shown in figure 4.8, at the central frequency.

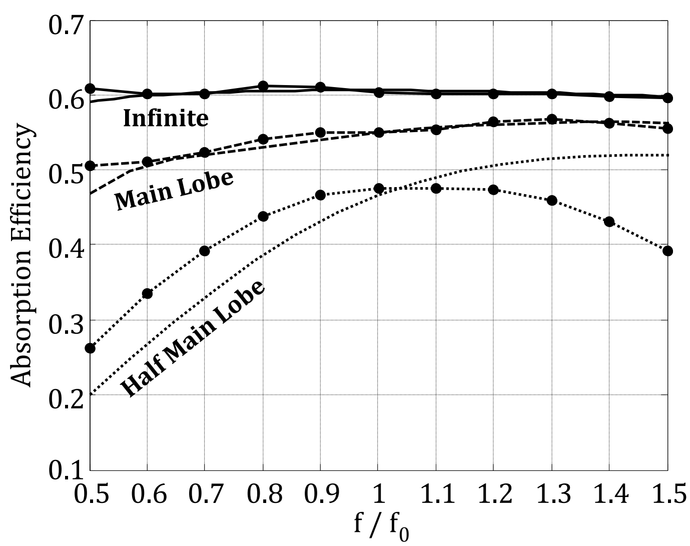

Figure 4.12: Analytical absorption efficiency validated with CST (lines with dots) for three different areas of the absorber: infinite area and the areas which sample the main lobe and half of the main lobe, for the same $R/D = 0.6$ case of figure 4.10. Areas considered at the central frequency.

4.5 Absorber Design for KIDs

In this section, the proposed analytical model is used to design some absorber configurations with optimum performances. First, we point out the influence of different multilayer stratifications, placed at the focal plane of a dielectric lens, on the absorption efficiency. The efficiency of a free-standing absorber (an absorber placed on an infinite silicon medium) would have a maximum efficiency of 50% that would decay smoothly with the R/D ratio of the lens. To improve the efficiency, one can place a silicon backshort at $\lambda/4$. The efficiency goes up to 100% and also decays smoothly with the R/D ratio, as shown in figure 4.13. Instead, if the backshort is placed at $\lambda_0/4$ in free space, the efficiency will increase up to 100% but have unexpected variations versus the R/D ratio due to the presence of the critical angle, shown also in the same figure. The most surprising case is when the absorber is placed between infinite silicon and free space mediums. In this case the efficiency is 78% for normal incidence and increases for R/D ratios associated to subtended rim angles larger than the critical one, see figure 4.13. This increase is related to the fact that there is no power transmitted to the air medium after this angle. Figure 4.13 also shows the CST validation of the efficiency for two angles, $\theta_0 = 30°$ and $\theta_0 = 50°$, and for each case considered.

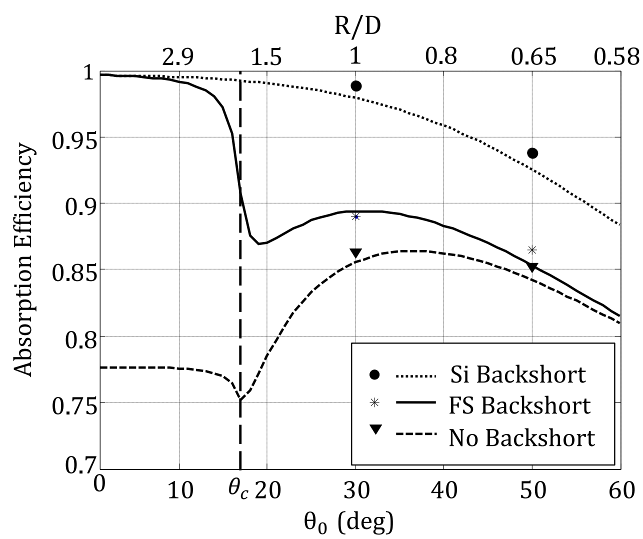

Figure 4.13: Absorption efficiency versus lens subtended rim angle (the R/D value related to each angle is indicated in the upper axis) for three different stratifications: backshort in free space (FS) and using a silicon slab (in both cases $d_y = 53\mu m$, $w = 14\mu m$), and no backshort with free space under the absorber ($d_y = 41\mu m$, $w = 14\mu m$). In all cases, $D = 70\lambda = 20\lambda_0$ (at $f_0 = 350$ GHz), $R_s = 30\Omega$ and a matching layer is used. Dots, asterisks and triangles correspond to CST simulations.

Second, we have investigated how to maximize the absorption frequency bandwidth. According to figure 4.13, the optimum cases when a silicon/free space transition is present are: $\theta_0 = 13°$ with backshort and $\theta_0 = 35°$ without backshort. The case where the backshort is in silicon is not considered here because, as it is proved in Chapter 3, it provides narrower bandwidth compare to the other cases considered. The efficiency as a function of the frequency is shown in figure 4.14, when a standard quarter wavelength

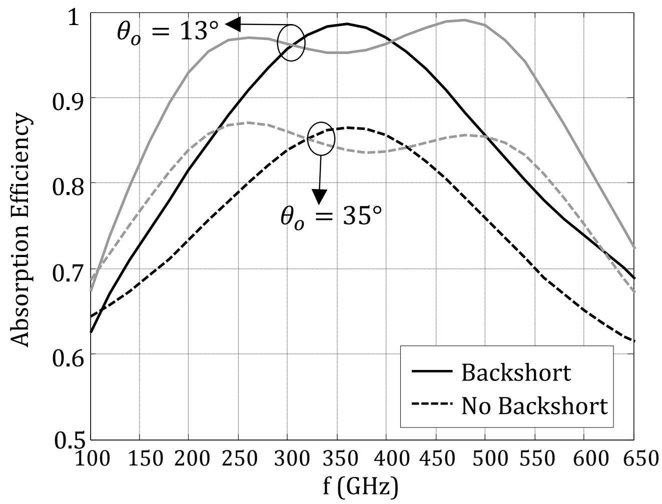

Figure 4.14: Absorption efficiency for two optimized lenses with and without free space backshort. Black lines represent a single matching layer ($\varepsilon_{rm} = 3.45$ and $h_m = 115.4\mu m$) and the gray lines a double matching layer ($\varepsilon_{rm1} = 2.07$, $\varepsilon_{rm2} = 4.90$, $h_{m1} = 144.1\mu m$ and $h_{m2} = 96.1\mu m$). Same absorbers parameter and lens aperture than in figure 4.13.

matching layer is used. It is evident that the better performance, in terms of both efficiency and bandwidth, is obtained for the backshort case. The frequency response of this case is actually limited by the matching layer, and not by the absorber itself (see Chapter 3 for curves associated to plane wave efficiencies showing larger absorption bandwidths). If a double matching layer (or, for instance, wide-band grove based matching layers [118]) is employed, the efficiency bandwidths can be increased considerably as shown in figure 4.14.

Finally, a comparison of the efficiencies of KIDs coupled to reflectors versus lenses is presented in figure 4.15. Typically, reflectors are characterized by very large R/D ratios (e.g. future telescopes, as SPICA, are being planned with $R/D = 10$). In this case, the absorber is free-standing, i.e. printed in a very thin silicon membrane. Figure 4.15 shows the efficiency of an infinite free-standing absorber under large R/D parabolic reflector, typical of space astronomical telescopes, for the SAFARI first frequency band. The 80% relative bandwidth corresponds to 1.4 octaves. In the same figure, the two best cases shown in figure 4.14 for the lens coupled absorbers are also plotted as reference. In these cases, the absorbers have a finite area that covers the first two secondary lobes of the focal field. The 80% bandwidth of the single matching layer case is comparable to that of the parabolic reflector: 1.2 octaves. If a broader band matching layers is employed, the bandwidth can be significantly increased. For the example of the figure, the relative bandwidth is 1.9 octaves.

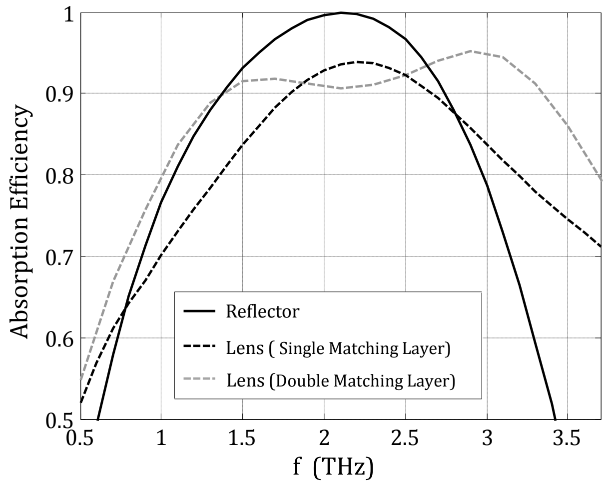

Figure 4.15: Absorption efficiency optimized for SAFARI Scenario for a lens coupled absorber with $R/D = 2.2$ plus a free space backshort, and for a free-standing absorber printed on a thin silicon membrane of $\lambda_0/200$ thickness under a $R/D = 10$ reflector.

It could be possible to increase the absorption bandwidth also in absorbers on the focal plane of reflectors by using thick silicon substrates with broadband matching layers. However, for KID focal plane arrays, the absorbing area would be limited to at least 75% of the total array sampling area [34]. The remaining 25% area is required for the read-out circuits. Instead lens coupled KID will lead to a better sampling efficiency.

4.6 Conclusions

An analytical spectral model able to analyze efficiently THz absorbers hosted in complex focal plane arrays has been presented. The model applies the Fourier Optics plane wave representation of the focal plane fields to realistic reflector and lens systems linked to an analytical equivalent network, representing the absorber currents. A validation of the methodology via comparison with an alternative numerical full-wave technique has been presented. Finally, wide-band and high absorption efficiencies are obtained for lens-coupled absorbers.

Chapter 5

Time-Delay Multiplexing with Linear Arrays of THz Transceivers

5.1 Introduction

The Jet Propulsion Laboratory's (JPL) 675 GHz imaging radar, summarized in [5], utilizes a single mechanically scanned beam to rapidly detect hidden objects and weapons under clothing. The radar operation is based on the frequency-modulated continuous-wave (FMCW) technique to get three-dimensional target images using a $\sim$30 GHz bandwidth. It has been demonstrated to effectively detect concealed person-borne threats [44], [41], [43]. This system generates 40×40 cm images of targets located at 25 m standoff distances with frame rates of about 1 Hz. To overcome signal attenuation, the radar relied on an active, heterodyne transceiver architecture. The specific details on the radar's performance capabilities can be found in [5], however, as a clarification for the rest of this chapter and the next one, a brief summary of the THz imaging radar antenna system is provided in next section.

Increasing the radar's imaging speed is important to handle targets in motion and to image over a larger field of view (FoV). This speed could be increased using faster beam scanning motors, but this approach is infeasible because the motor's size and power requirements increase rapidly with the FoV and frame rate. Another option to shorten the acquisition time, while minimizing the same number of transceivers is to implement quasioptical time-delay multiplexing of the radar beam. This method was first described and demonstrated in a 4 m standoff radar prototype [46]. The method involves diverting half of the radar beam's power through a delay line using a quasioptical waveguide (QOWG).

The time-delay multiplexing technique does not introduce any modifications in the scanning mechanism or back-end electronics hardware, while reducing the imaging time by a factor of two. However, for near-video rate imaging, to multiplex a single beam into two is still not enough; a THz transceiver array will be necessary. The next generation of heterodyne arrays at submillimeter wavelengths is likely to be in the format of linear arrays, [51] and [47]. Here we present a study of how time-delay beam multiplexing can work for an array of multiple beams simultaneously.

5.2 THz Imaging Radar Antenna System

The quasioptical system of the imaging radar developed at JPL is explained in detail in [45] and [119]. It can be divided in two main parts: the scanning and the feed optical subsystems, as figure 5.1 shows. The scanning system is composed of a confocal Gregorian reflector system (CGRS) consisting on two reflectors: a primary ellipsoidal reflector with one focus confocal with a parabolic sub-reflector and the other in the standoff plane at a distance of $R = 25$ m. The CGRS was chosen because its excellent scanning performance, [120], as a consequence of a cancellation of the coma and astigmatism aberrations that are normally present in more conventional reflector configurations, [121]. The election of an ellipsoidal primary reflector is explained because the 25 m standoff distance is electrically very close to the antenna (in its near field) for a 675 GHz radar. A parabolic reflector would focus in the far field. Therefore, an elliptical main reflector with a near field focusing point is needed to achieve diffraction-limited focusing at 25 m. The collimated beam illuminating the parabolic sub-reflector is generated at the feed optics and scanned by a flat mirror. A small rotating mirror for beam steering was proposed due to the technical challenge of scaling a phased array technology to submillimeter waves. Furthermore, it reduces the scanning time compared to an initial version of the optical system where the main aperture was slowly rotated, along with the system's front-end electronics, to image the target. The rotating mirror is illuminated by a collimated beam rather than a expanding one because it relaxes the tolerances on the position of the rotating mirror's principal axes, which otherwise would be difficult to align at these frequencies. This results in negligible aberrations over the large field of view. The scanning mirror is mounted on orthogonal rotary motor stages that rotate it an angle (θ_m) about two axes (elevation and azimuth), steering the collimated beam by $\theta_{sm} = 2\theta_m$. The beam is then focused by the primary reflector at the standoff plane and steered towards $\theta_s = 2\theta_{sm}/M$ where M is the system magnification (considering a beam-deviation factor 1 for simplicity). Therefore the beam is focused at $\rho_s \approx \theta_s R$ in the target plane. With a magnification M=10, the target field of view is ± 0.25 m $\times$ ± 0.25 m. The plane shown in figure 5.1 will be denoted as the vertical or elevation plane. Beam steering over the target plane at range can also be achieved by displacing the transceiver from the feed reflector's focal point by a distance $\Delta\rho$. In other words, the collimated beam incident over the flat mirror will be titled by $\Delta\rho/F$, where F is the feed reflector focal distance (see figure 5.2).

In this radar antenna system, a beam splitter is used in the THz transceiver to accomplish the transmitter/receiver duplexing. The beam splitter consists of a thin silicon wafer oriented at 45° form the outgoing beam. This system provides very high isolation with the cost of 6 dB two-way signal loss from its unused port. A more optimal solution would be to use a circulator to accomplish the duplexing, however, it cannot be easily obtained at these high frequencies.

The THz radar images are acquired by raster scanning the radar beam across the field of view, with two different speeds. The elevation is the fast direction while the azimuth is the slow one. The vertical scanning is accomplished with a fast precision rotator that constantly accelerate, for the first half of the scan, and decelerate, for the second half, in order to get a scanning time limited by the maximum motor torque. This fast acceleration is one of the keys to achieve short imaging times. The horizontal motor rotation speed is kept constant obtaining a serpentine scan path. This linear raster scanner generates a continuous motion that uniformly samples the image. As explained in [45], there is an inverse-squared relationship between the image time and the scanning-mirror acceleration in the vertical direction. In view of this fact, to simultaneously project several beams onto the target (either by multiplexing or using arrays), one have to consider that there is a substantial difference in acquisition time depending on weather the beams lie on in the vertical or horizontal direction due to the different speeds of the two directions. If the division is done in the horizontal plane in N_h parts, then the time reduction would be N_h whereas the horizontal motor speed will be kept the same. However, if the division is done in the vertical plane in N_v parts, the reduction would be only $\sqrt{N_v}$ due to the square-root dependence of the vertical scanning time and the FoV vertical length. It is, therefore, preferable to have a the multiple beams located in the same plane where the fast scanning is located for the maximum acquisition time reduction.

The radar system imaging speed increase is limited by two factors: the motor's acceleration and the SNR. Faster scanning optics might be possible, but, as the scanning motor's acceleration scales as the inverse square of the imaging time, it is unlikely to be done in a cost effective manner. For heterodyne radar detection, the SNR is directly proportional to the dwell time per image pixel ($\tau = \tau_i/N_m$, being τ_i the total imaging acquisition time and N_m the number of pixels mechanically obtained with the raster scanning), $SNR \propto P_0\tau/N_0$. An order of magnitude frame rate speed-up would degrade the radar image quality. However, in the JPL's imaging radar, the limitation factor for the imaging speed is the motor rotation speed, not the SNR degradation.

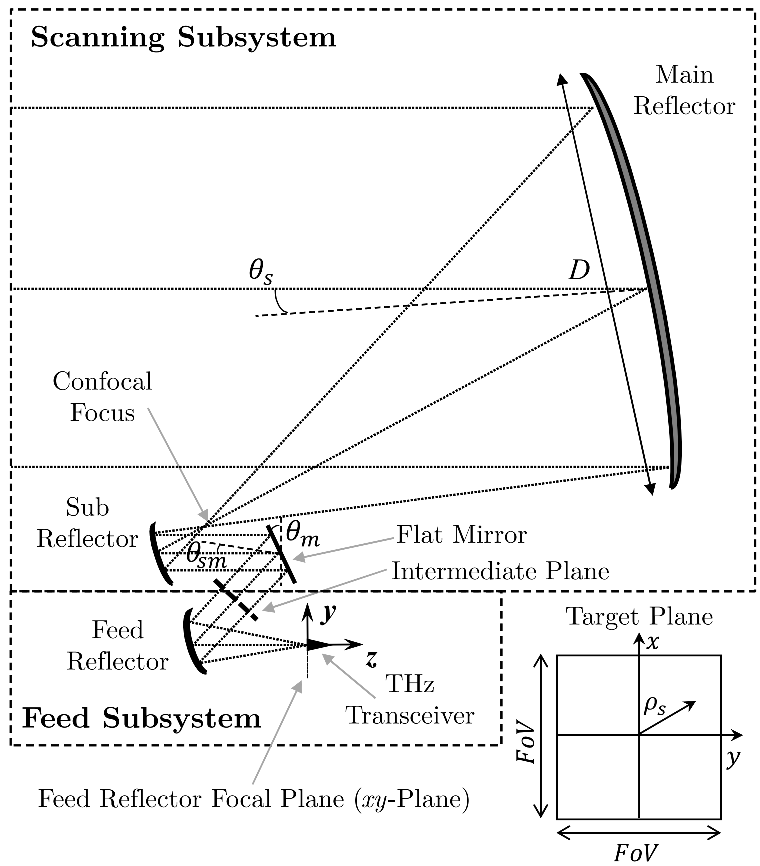

Figure 5.1: Geometry of the THz radar quasioptical system (vertical plane). Bottom right, the target plane FoV.

5.3 Quasioptical Multiplexing System for a Single Transceiver

The method used to increase the radar frame rate is based on time-delay two-beam multiplexing, dividing the radar's beam into two. Each beam points to a different half of the FoV during scanning, with a subsequent reduction in the scanning time. The FoV division is done at the intermediate plane (see figure 5.1) so both beams are scanned simultaneously. Both, the main and the multiplexed beams, are then focused in the target plane at offset locations. On reflection, both beams are detected using a single receiver and distinguished from one another by a separation (delay) in their time-of-flight to the target. The multiplexing system is placed along the horizontal or azimuth plane of the system.

In the first time-delay multiplexing approach described in [46], the beam splitting and polarization rotation were done using waveguide structures, leading to high ohmic losses and decreased sensitivity from transmit/receive signal leakage. A low-loss alternative using an all-quasioptical multiplexing approach (a silicon wafer beam splitter and a rooftop mirror polarization rotator) was proposed in [45] and implemented successfully in [5] to avoid these problems while still doubling the imaging frame rate. A system based on the same quasioptical waveguide (QOWG) system was used to obtain polarimetric radar images.

The silicon beam splitter duplexes the transmit and receive beams, and the power deflected by the beam splitter (3 dB) is captured by the QOWG to form the multiplexed beam. In this way, we are reusing 3 of the 6 dB initially lost by the beam splitter. The time-delay multiplexing technique reduces the imaging time by a factor of two, without increasing the scanning mirror speed, raising the SNR by a factor 2, as in this case: $SNR_{Mux} \propto P_0\tau'/N_0$ where $\tau' = \tau_i/N'_m$ and $N'_m = N_m/2$.

5.3.1 Quasioptical Waveguide Design

The initial implementation of the QOWG, with a delay of 90 cm, is shown in detail in figure 5.2.The QOWG is designed to obtain a multiplexed beam with an equivalent focus in the feed reflector's focal plane (described with a gray triangle in figure 5.2), displaced symmetrically about its focal point with the main beam. The distance of this displacement can be calculated by considering that to double the imaging speed by halving the scanning mirror's rotation angle in the horizontal direction, the multiplexed and main beams in the target plane have to be focused at a distance $\rho_s = FoV/4$ from the center of the FoV. Therefore, we need to introduce an angular tilt in the collimated beam of $\theta_{sm} = \rho_s M/R$. This angle will be obtained by tilting the beam by $\theta_h = \theta_{sm}$ at the intermediate plane. If the transceiver is displaced from the feed reflector focal point by $d_h = \rho_s MF/R$ in the x-axis (see figure 5.2 and 5.3), the beam generated by the feed reflector will be tilted the required angle. In the same way, if the multiplexed beam's equivalent focus is displaced a distance d_h on the other side (see figure 5.2) then this beam will be tilted an angle $-\theta_h$ at

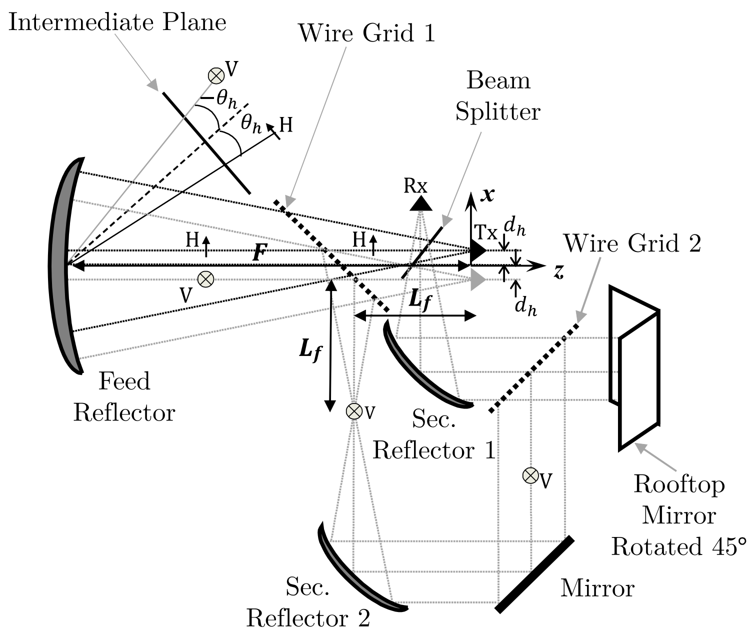

Figure 5.2: Schematic of feed optics including the QOWG multiplexing system showing the horizontal plane.

the intermediate plane. In figure 5.3 a schematic of the feed reflector focal plane is shown.

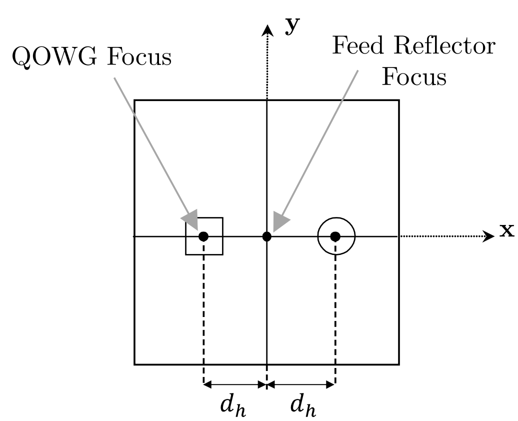

Figure 5.3: Feed reflector focal plane composed of the transceiver horn (represented with the square) and the equivalent multiplexed beam (represented with a circle) offset symmetrically from the feed focus at the origin.

The whole optical system (including the QOWG) has been simulated with GRASP in order to calculate the beams' field shape at the target plane. In figure 5.4, the beams' radii at -3 dB are shown as a function of the ϕ-coordinate, considering a polar coordinate system centered at the point of maximum power for each target spot. The fourth power of the electric field is calculated because the radar's two-way beam path effectively squares the

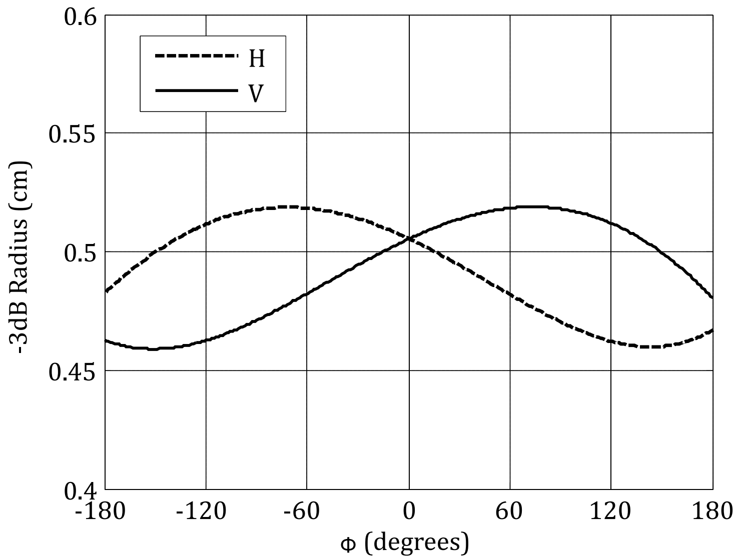

Figure 5.4: Main (H) and multiplexed (V) beam -3 dB radius, calculated for $|E|^4$.

beam intensity. The beams have a slightly elliptical shape, due to the phase aberrations, as shown in figure 5.5. The phase aberrations are due to difference in the path length of all the rays, introduced when shifting the feeds from the feed reflector focus. It is possible to make, for each beam, a ray tracing and calculate, in the spot diagram at the target plane, the radius of each ray with respect to the central one. Therefore, a measure of the system aberrations can be the root mean squate (RMS) radius of all the rays in the spot diagram. For the single-transceiver multiplexing system, the main and multiplexed beams have a RMS radius of 16.2λ. In this case, the QOWG itself does not introduce any extra optical phase aberrations because the transceiver is located in the QOWG focus. Aberrations come dominantly from the displacement of the beam foci from the feed reflector focus. This is in contrast to the results presented in section 5.4. The system resolution is 1.04 cm, calculated as the two-way beam width at -3 dB (Half Power Beam Width or HPBW). This value is obtained as the average of the beam's -3 dB radius as a function of the ϕ-coordinate. The system's one-way spillover, simulated as the losses in the optical system when the beams have traveled from the source to the target, is 0.35 dB for both beams.

5.3.2 Measurements

The QOWG has been manufactured and measured together with the radar optical system. Figure 5.6 shows a photograph of the manufactured multiplexing system.

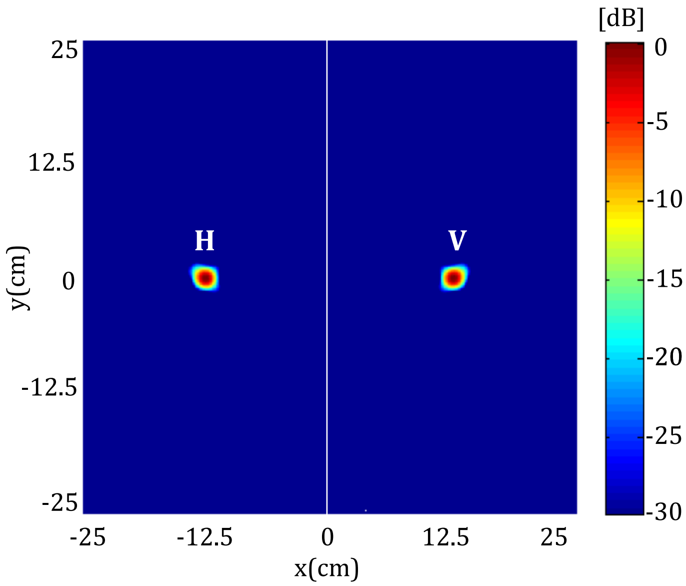

Figure 5.5: Main (H) and multiplexed (V) beams for a single transceiver, at the target FoV, simulated with GRASP and plotted as $|E|^4$.

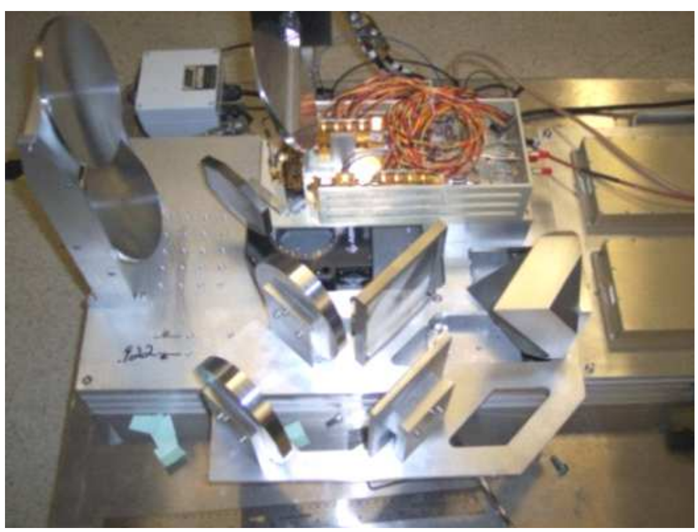

Figure 5.6: Photograph of the manufactured multiplexing system.

The beam profiles were experimentally validated by imaging a 3 mm diameter metal bead suspended by nylon thread at a 25 m standoff distance. Figure 5.7 shows the measured beam profiles for the H and V signals. The measured beams' shapes are quite circular, in an agreement with the simulations of figure 5.5. Both measured signals have a similar power level, confirming that the QOGW does not introduce significant additional losses in this case.

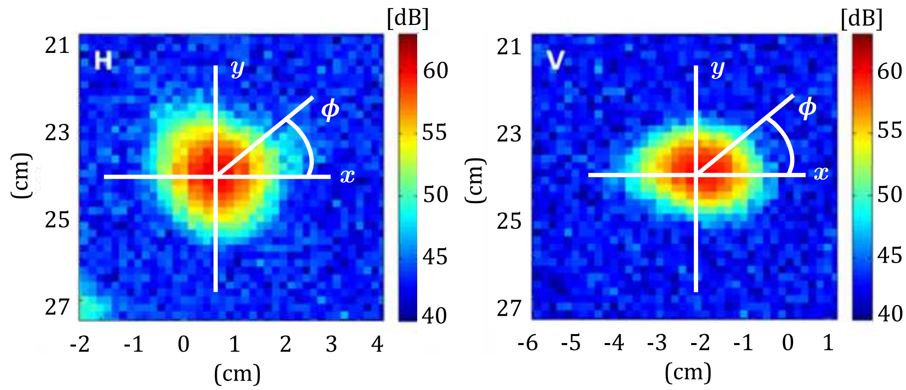

Figure 5.7: Main (H) and multiplexed (V) beam profile measurements.

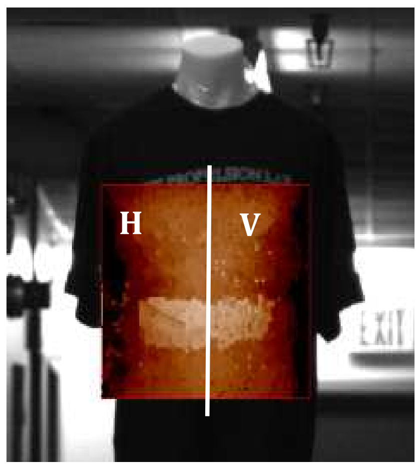

Figure 5.8: Concealed object image acquired with the multiplexing system.

Figure 5.8 shows an example of a fast 1 second (1 Hz) image obtained with the two-beam multiplexing system of a concealed mock bomb-belt on a mannequin at 25 m standoff distance. Without the two-beam multiplexing, the image of figure 5.8 would have taken 2 seconds to acquire with the same pixel density.

5.4 Quasioptical Multiplexing System for a 2×1 Transceiver Array

Results obtained in the previous section for a single transceiver show that multiplexing is a feasible technique to double the acquisition speed without any additional THz, RF, or computing hardware. The next step towards a multiplexed array is to study the performance of this technique with a two-element transceiver array.

5.4.1 Quasioptical Waveguide Design

For this new configuration, almost the same QOWG is used. In this new design, we have the FoV divided in four regions with a total of four different beams. To this aim, a vertical beam tilt, $\pm\theta_v$, at the intermediate plane, as well as the horizontal ones, $\pm\theta_v = \pm\theta_v$, needs to be implemented. The vertical tilt is generated with an additional vertical displacement of the transceiver, d_v, as shown in figure 5.9. With these shifts, the theoretical position of the multiplexed beams' virtual foci in the feed reflector focal plane are displaced in the vertical plane, d_v, and in the horizontal plane, d_h. As explained in section 5.2, a vertical division of the FoV, leads to a time reduction by a factor of $\sqrt{N}$ when the FoV is divided in N regions, due to the sinusoidal acceleration of the vertical scanning motor. Thus with this new configuration, a $2\sqrt{2}$ frame rate speed-up compared to a single scanning beam is possible. The linear array of transceivers has been chosen to lie along the y-axis, which is the symmetrical plane of the QOWG (xz-plane). With this orientation, the aberrations introduced by the QOWG in both multiplexed beams are the same and lower than if the array were placed in the other plane. Multiplexing is therefore still done in the horizontal plane.

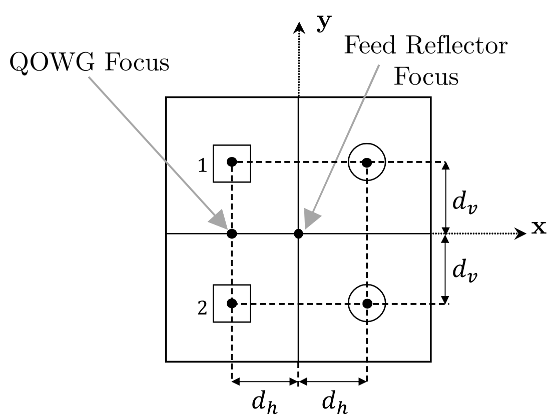

Figure 5.9: Feed reflector focal plane composed by the 2×1 transceiver array (squares) and the theoretical positions of the multiplexed beams' foci (circles) in the feed reflector focal plane. The feed reflector focus is located at the origin of the coordinate system.

In the single-transceiver configuration, a rooftop mirror oriented at 45° was used to rotate the multiplexed beam polarization. This works as long as the multiplexed beam impinges on the rooftop aperture with normal incidence. In the two-transceiver case, the transceivers are slightly shifted away from the QOWG focus. When the beams leave the first parabolic reflector of the QOWG, they are tilted in the yz-plane (the vertical plane). If a rooftop reflector were used, the outgoing beams will therefore be deflected into the horizontal plane, away from their intended positions in the target plane. To overcome this problem, a different method to rotate the polarization is used, based on a grooved grating rotator as shown in figure 5.10. The same grating concept was used in [122] to design a 675 GHz radar duplexer with low loss. This grating exhibited high efficiency with losses better than 0.1 dB over the radar's 5% bandwidth. In the polarization rotation implementation of figure 5.10, the grating polarizer converts the incoming linear polarization (H) in a circular one (right-hand-circular, or RHC). Then the circular polarization reflects from a flat mirror that reverses the direction of rotation to left-hand-circular, or LHC, and then the grating converts the LHC polarization back to linear, but with orthogonal direction (V). With this technique, the incident and reflected signals, with orthogonal polarization, remain in the same plane even if they arrive with a tilted angle.

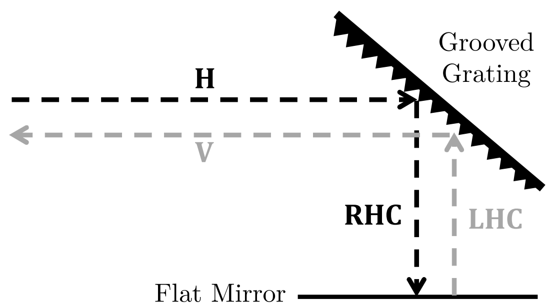

Figure 5.10: Operating principle of grating-based polarization rotator.

Figure 5.11 shows the simulation of the four beams' fields at the target plane. The multiplexed beams are observed to be not Gaussian because they are affected by strong phase aberrations caused by the displacement of the transceiver from the QOWG focus. They have lost their beam symmetry due to the vertical shift in the feed reflector symmetric plane, $\pm d_v$. Furthermore, the multiplexed rays arrive to the feed reflector with a tilt in the yz-plane as a consequence of the shift in the QOWG focus. This tilt causes non-uniformities in the illumination of the feed reflector, increasing the aberrations of the multiplexed beams compared with the main beams. The main beams also have significant aberrations due to the vertical shift of the transceivers from the feed reflector focal point. In this case the RMS radius is 22.3λ for H1 and H2, 14.7λ for V1 and 27λ for V2.

In figure 5.12, the beams' radii at -3dB are shown as functions of the ϕ-coordinate. The beams have lost the symmetry that was presented in the simpler multiplexing geometry

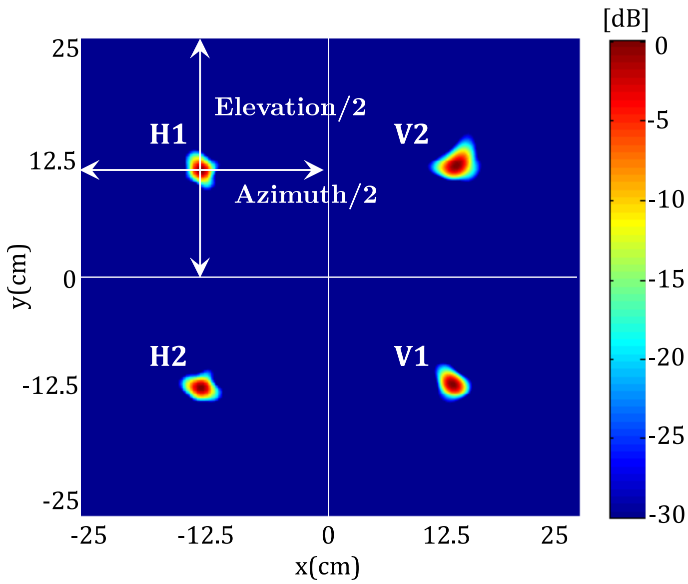

Figure 5.11: Main (H1 and H2) and multiplexed (V1 and V2) beams for a 2×1 transceiver array, at the target FoV, simulated with GRASP and plotted as $|E|^4$.

in figure 5.5. The resolution in this case is 1.54 cm, determined by the highest radius variation, i.e., beam V2. The spillover, shown in table 5.1, is different for each one of the four beams and it takes a maximum value of 2.09 dB for the V2 pixel.

Beam	Spillover (dB)
H1	0.37
H2	0.40
V1	1.71
V2	2.09

Table 5.1: One-way spillover for the main and multiplexed beams.

5.4.2 Measurements

The two-element QOWG configuration has been manufactured to validate the design. The beam profiles were experimentally validated by imaging the same small metal beads as in the single element case. A photograph of the grating rotator implemented to rotate the multiplexed beams polarization is shown in figure 5.13. Figure 5.14 shows the measured beam profiles for the upper transceiver (H1 and V1) signals.

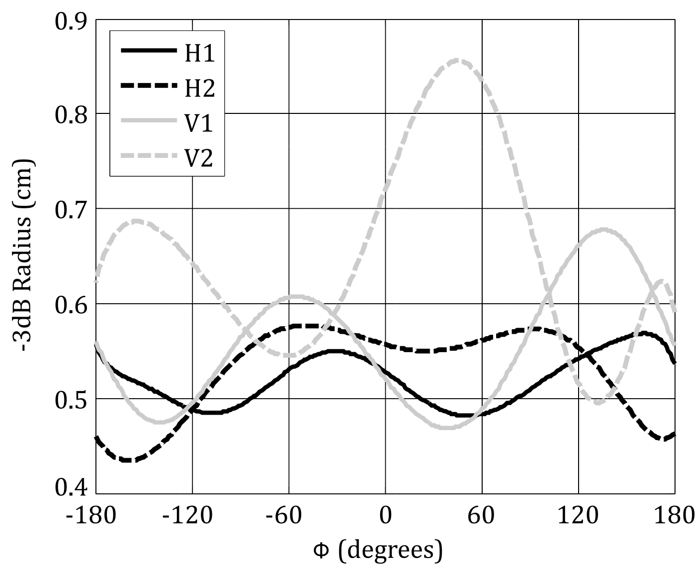

Figure 5.12: Main (H1 and H2) and multiplexed (V1 and V2) beams -3 dB radius, calculated for $|E|^4$.

Figure 5.13: Photograph of the grating rotator used to rotate the multiplexed beams polarization in the two elements QOWG configuration.

Both signals (H1 and V1) provide similar resolution and are consistent with the values obtained in the simulations. However, when the measured signals levels are compared, the multiplexed beam is about 6 dB weaker than the main beam. This difference is due to the spillover as well as the larger HPBW. The larger HPBW results in less power level reflected from the target bead, reducing the measured signal amplitude.

Another issue encountered with this design is that the small losses in the grating polarizer result in a weak backscattered signal with H polarization that goes through the vertical wire grid 2 in figure 5.2, and arrives again in the feed reflector plane. For example,

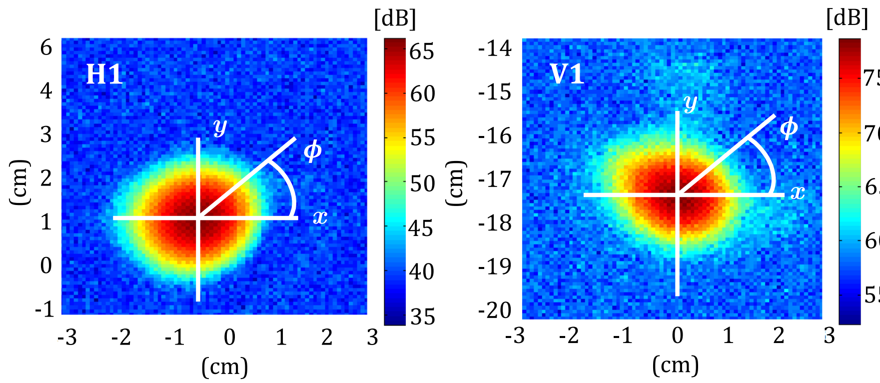

Figure 5.14: : Main (H1) and multiplexed (V1) beam profile measurements for the transceiver upper channel.

when the beam generated by transceiver number 1 (see figure 5.9) arrives at the grating with an angle θ in the vertical plane, the small backscattered signal will be tilted an angle $-\theta$, will pass through the wire grid, and will arrive exactly at transceiver number 2 (and vice versa). This unwanted cross-talk corrupts the receiving signal and affects the receiver sensitivity, and must be mitigated by slightly shifting the whole transceiver in the vertical plane. In this way the transceivers will not be symmetrical in the this plane and the receiving signal will not be corrupted by the wrong polarization. The displacement needed in the transceivers is the equivalent of one beamwidth in the feed focal plane and therefore it should not impact the imaging performances.

The simulations and measurements performed validate the multiplexing concept and its feasibility for reducing the acquisition time in imaging systems. However, if we want to extend this method for multiplexing larger arrays, the optical system needs to be improved in order to obtain good quality beams with minimal optical aberrations and spillover.

5.5 Multiplexing of Large Linear Arrays

The optical aberrations and spillover loss obtained for the two-element transceiver will be even higher when larger arrays are multiplexed due to the higher shift of the beams from the system focus. For this reason, it is very important to optimize the optical design in order to reduce as much as possible these aberrations and the spillover level. The multiplexing configuration performance can be improved by modifying the feed optics system. One optically simple solution is to increase the system f-number ($f_{\#}$). This solution involves a change in the $f_{\#}$ of the feed reflector and also in the QOWG. By increasing the $f_{\#}$, the angle at which the multiplexed beams leave the QOWG is smaller. This will considerably improve the illumination of the feed reflector. Moreover, the use of large $f_{\#}$ numbers leads to lower scanning losses and better beam qualities for parabolic reflectors, [123].

The simulated beams obtained by multiplexing the two-element array have been improved by increasing the system $f_{\#}$ from 1.4 to 2.9. To maintain the primary reflector's original illumination, the transceiver horns' taper angle also need to be modified from 12° to 6.2°, and the feed reflector focal length has been increased from 19.5 cm to 40 cm. The element separation is fixed by the focal distance of the feed reflector, so d_h and d_v are also increased to achieve the correct displacement of the beams in the FoV. The array is sparse with a separation between the elements of 4.2 cm. The horn antenna directivity is 30 dB so the Gaussian beam generated has a beam waist of about 1.4 mm, much lower than the array's elements separation ensuring that we have no space problems. In figure 5.15 the proposed QOWG modifications are shown. The distance between the elements of the QOWG is modified to suit the new configuration, avoiding ray blockage. In figure 5.16, the simulated beams fields are represented, and the beams shape has significantly improved with more symmetrical fields for both the main and multiplexed beams. With this system the RMS radius has decreased to 6.7λ for H1 and H2, 13λ for V1 and 9λ for V2. In table 5.2 the new one-way spillovers are shown and the maximum value has also decreased considerably to 0.63 dB for the V1 beam.

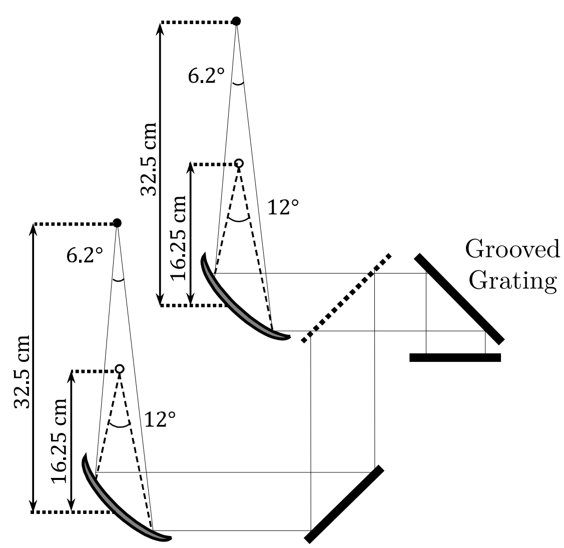

Figure 5.15: Comparison between the QOWG with $f_{\#} = 1.4$ and transceiver horns' taper angle of 12° and the new QOWG with $f_{\#} = 2.9$ and transceiver horns' taper angle of 6.2°.

Figure 5.17 shows a comparison of the -3 dB radius of the beam V2 for the initial two-

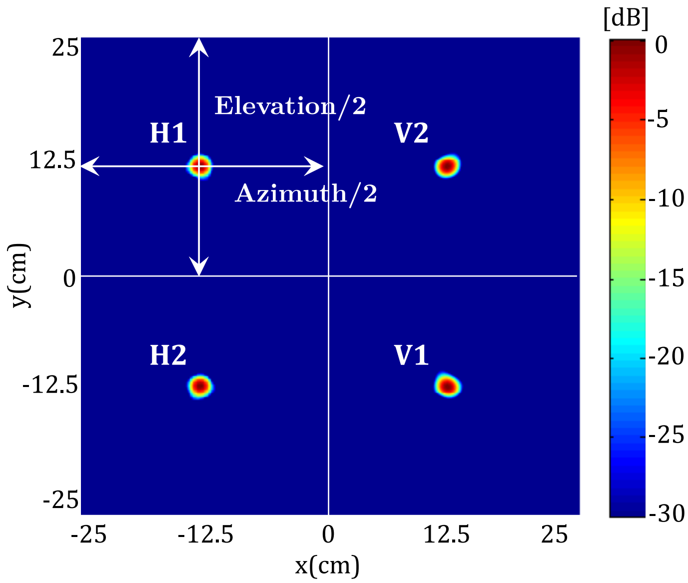

Figure 5.16: Main (H1 and H2) and multiplexed (V1 and V2) beams at the target FoV for a 2×1 transceiver array increasing the QOWG f-number, simulated with GRASP and plotted as $|E|^4$.

Beam	Spillover (dB)
H1	0.57
H2	0.51
V1	0.63
V2	0.58

Table 5.2: One-way spillover for the main and multiplexed beams for the QOWG with $f_{\#} = 2.9$.

element QOWG configuration ($f_{\#} = 1.4$) and the new configuration with a larger f-number ($f_{\#} = 2.9$). The resolution has been considerably improved, obtaining a value of about 1 cm that is comparable to the resolution achieved by the initial system where just one beam was multiplexed.

For video-rate imaging speeds, larger linear arrays will be needed. The new feed optics configuration, figure 5.15, allows the multiplexing of such large arrays due to the low aberrations and spillover levels that it provides. A six-element array, multiplexed with the $f_{\#} = 2.9$ QOWG shown in figure 5.15, has been simulated in order to study the performance of the designed system with large arrays. The array is placed along the elevation axis agreeing with the symmetrical axis of the QOWG. For maximizing the scanning speed, the slow motor should be in the elevation axis and the fast motor in the azimuthal axis,

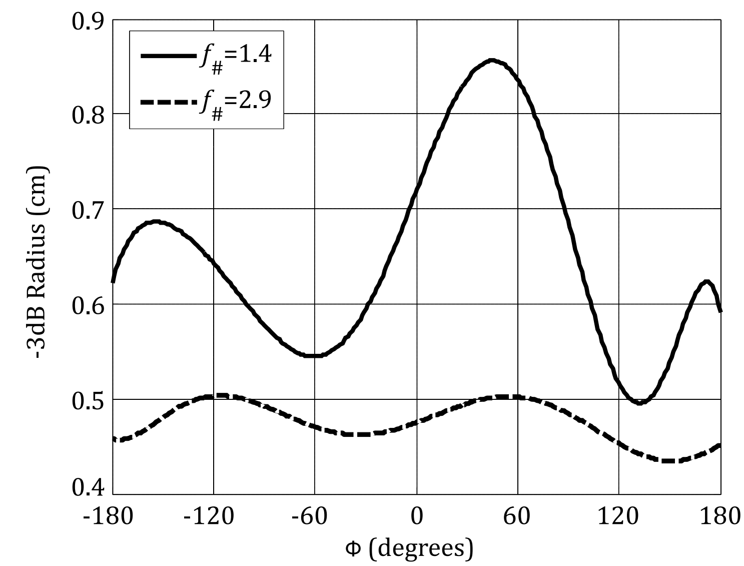

Figure 5.17: -3 dB radius of the beam V2 for the QOWG with $f_{\#} = 1.4$ and the new geometry increasing the system f-number to $f_{\#} = 2.9$.

contrary to the initial case, as explained in section 5.2. In figure 5.18a, the fields obtained at the target plane are shown. As it can be observed, the multiplexed beams shape is almost circular even for the edge pixels, but their position in the target plane describes a curve, in contrast to the main (H) beams that lie on a line. This shift in the beams position is due to the tilt of the rays when they leave the QOWG. This tilt could be further reduced by increasing even more the QOWG focal distance. However in order to maintain the system total dimension comparable to the original one (figure 5.1), the dimensions of the multiplexing system in the x-axis are limited by the main antenna reflector radius. The difference between the horizontal position of the edges beams (V1 and V6) and the central beams (V3 and V4), x in figure 5.18a, is 4 cm. It is possible to optimize the x-position of the array elements in the focal plane to compensate the multiplexed beam shift, see figure 5.19. Note that the elements of the array are only shifted transversally, not axially, so they are still placed in the xy-plane. In figure 5.18b the beams at the target plane, after the transceiver position optimization described in figure 5.19, are shown. The shift for both the main and multiplexed beams, in the target plane, is $x_H = x_V = 2$ cm; see figure 5.18b. This is slightly higher than the system resolution, so the scanning mirror rotation in the azimuth plane needs to be increased by an angle equivalent to this distance (x_H or x_V) to cover the whole field of view.

The RMS radius for the beam H1 is 13λ, 15λ for H2, 14.7λ for V1 and 14.3λ for V6, that are low values if we compare them with the other studied cases. The spillover level for

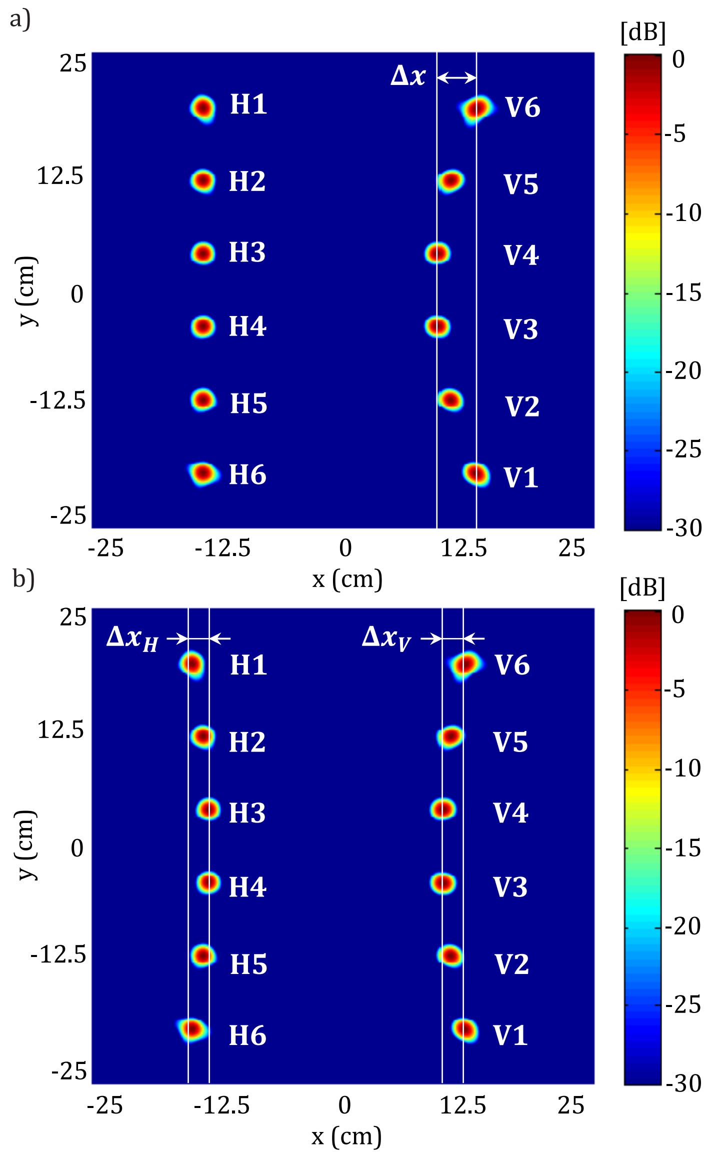

Figure 5.18: Main (from H1 to H6) and multiplexed (from V1 to V6) beams at the target FoV for a 6×1 transceiver array, simulated with GRASP and plotted as $|E|^4$. Beams obtained before, (a), and after, (b), the optimization of the transceiver positions.

Beam	Spillover (dB)	Beam	Spillover (dB)
H1	0.71	V1	0.89
H2	0.58	V2	0.62
H3	0.52	V3	0.52
H4	0.50	V4	0.52
H5	0.52	V5	0.57
H6	0.55	V6	0.72

Table 5.3: One-way spillover for the main and multiplexed beams for the six elements array.

the twelve beams is summarized in table 5.3 and it is better than 0.89 dB for all of them. In figure 5.20, the -3 dB radii for the edge beams are represented. The resolution, imposed by V1, is 1.2 cm, which is enough to obtain good quality images of concealed weapons.

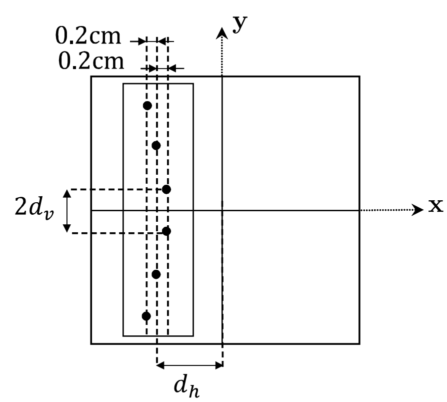

Figure 5.19: 6×1 THz transceiver array elements optimized position in the focal plane.

5.6 Conclusions

In this contribution we show how an all-quasioptical multiplexing technique can be used to increase the imaging speed of THz imaging radar based on linear arrays of transceivers. This increase is achieved by scanning the FoV with multiple pixels obtained from splitting each transmitted beam into two using a QOWG.

The multiplexing of large arrays is not trivial, as we have shown, due to the aberrations and spillover in the system. But it is possible to reduce these problems by designing QOWGs with large f-number. Displacements in the multiplexed beams can be reduced by

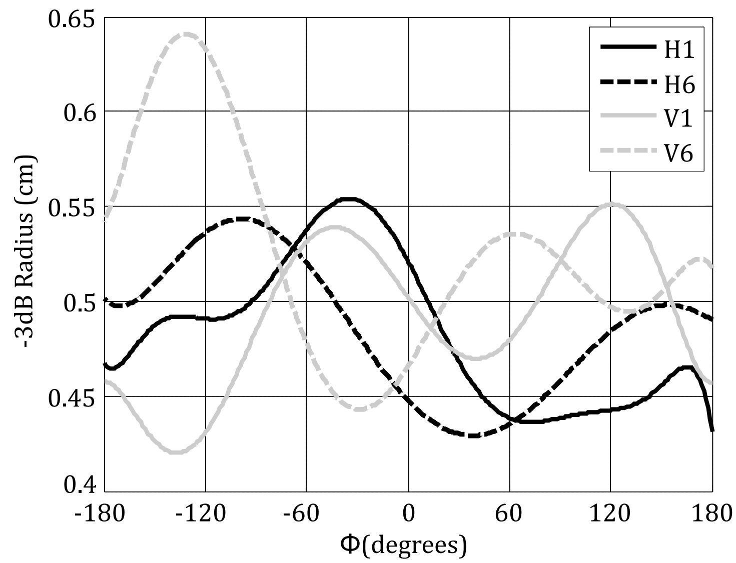

Figure 5.20: -3 dB radius of the beams H1, H6, V1 and V6 when multiplexing a six elements array.

optimizing the transceiver locations in the focal plane. In this contribution, multiplexing of a six-element sparse array has been simulated with a 1.2 cm resolution and spillover under 0.89 dB. The last array element beam is displaced by 24 HPBW in the target plane with respect to the FoV center, indicating that a compact array of 48 elements would have similar beam quality than the ones presented here.

In conclusion, the multiplexing technique could be a feasible and hardware-efficient method to reduce the acquisition time of the large transceiver arrays planned for future THz imaging systems.

Chapter 6

Refocusing a THz Imaging Radar

6.1 Introduction

Since the initial JPL's THz imaging radar system concept was demonstrated [44], almost all the improvements introduced in the radar have been related with the reduction of the acquisition time without degrading the image quality. However, the ability to acquire imagery over different standoff distances from the radar is also important.

The narrow beams needed for high resolution imaging only exist around the focal location of the antenna system. Outside this region the signal-to-noise ratio decreases and image blurring increases due to the defocusing effects resulting in gain loss and beam broadening of the antenna beam. Therefore, when objects located away from the nominal standoff distance are imaged, refocusing becomes necessary. To implement a refocusing system, the image focal plane must be displaced. Such displacement could be done extremely fast electronically by using phased arrays [52]. Although possible in theory, it is not practically achievable with the currently available THz technology. As an alternative, there is the conventional optical option to design a refocusing system by mechanically translating components as proposed in [119].

In the present chapter, an upgrade to the THz imaging radar optical system summarized in [5] is described. This upgrade provides this radar system with refocusing capabilities allowing imaging objects concealed in persons in movement. The method used is a mechanical axial translation of the transceiver. This is a simple way to implement the refocusing in the current system, because only the transceiver needs to be displaced without any modification in the optical system, and it provides good image performances. To avoid any

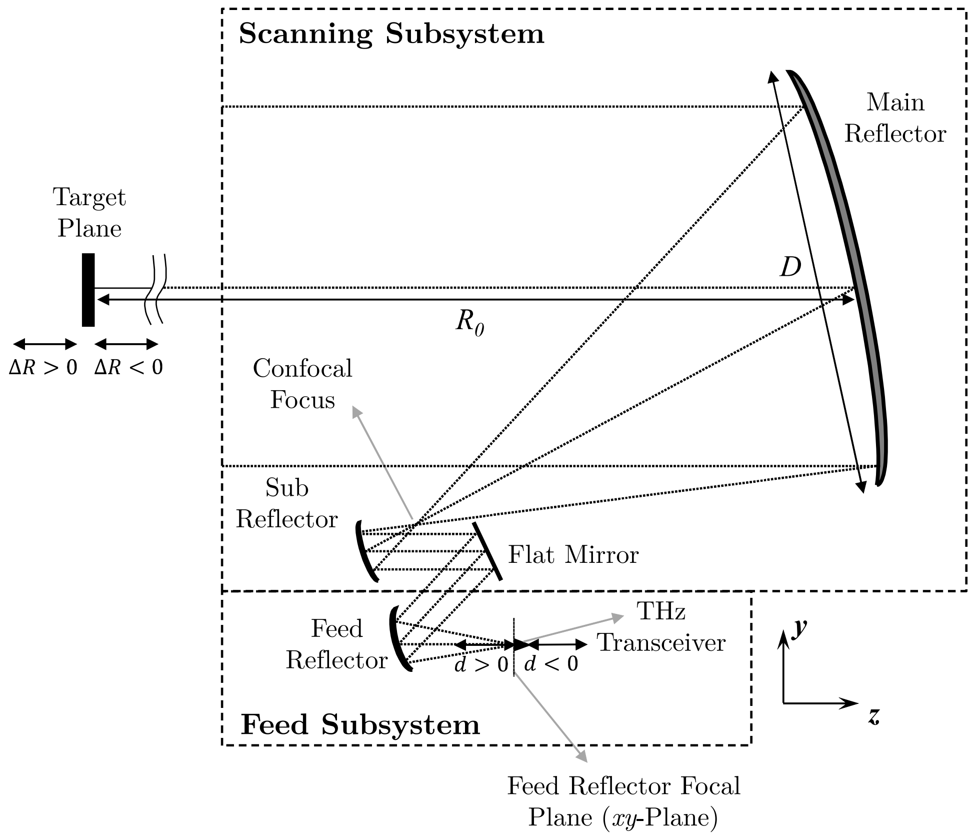

Figure 6.1: Geometry description of the THz radar optical system.

damage in the radar transceiver, the high frequency circuitry is packaged inside a metallic box. This box is mechanically displaced in order to achieve the refocusing.

Since the optical system is based on a confocal Gregorian configuration, the refocusing could be also achieved by shifting the sub reflector along an axis defined by the main ray. However, this approach will turn into higher spillover (SO) and significant ray blockage. The main reflector could also be displaced to this aim but, since it is a large reflector (1 m diameter), this will imply slow motion. A different approach for doing the refocusing could be the use of a deformable membrane mirror [124], once the technology will be available.

The desired refocusing range is 50% from the nominal distance, i.e., from 12.5 m to 37.5 m. This refocusing system and some measurements were initially presented in [125]. In the present chapter a detailed analysis of the optical system performances is presented. In section 6.2, the refocusing system implementation is described. The whole system has been simulated with the commercial software GRASP and results in terms of resolution, efficiency and optical aberrations are presented in section 6.3. The refocusing system was implemented and measured and the results are summarized in section 6.4. Finally, the system has been tested by acquiring through-clothes images of concealed weapons as it is shown in section 6.5.

6.2 Refocusing System Implementation

The initial optical system considered here is described in detail in [119], [125], [45] and a brief summary is provided in section 5.2 of Chapter 5. It is divided in two main parts: the scanning and the feed subsystems, as shown in figure 6.1. The scanning system is composed of the main ellipsoidal reflector with a secondary focus at the standoff plane. The main reflector is illuminated by a secondary parabolic mirror that focuses a collimated beam to the main reflector's close focus. The collimated beam, generated at the feed optics, is deflected by a flat scanning mirror mounted on orthogonal rotary motor stages to point the beam in elevation and azimuth. Because of the confocal geometry, the beam is then focused at the standoff plane by the main antenna, and steered over the field of view situated at a distance of $R_0 = 25$ m from the main antenna.

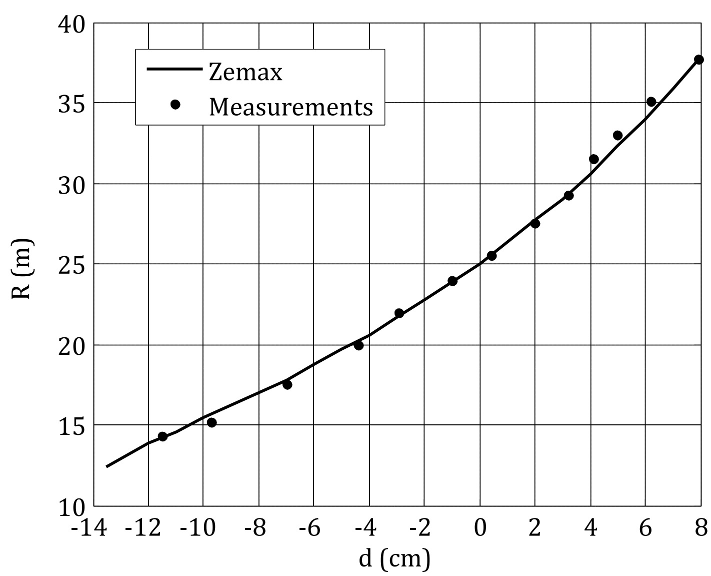

Figure 6.2: Refocusing distance (R) versus the transceiver axial translation (d). The solid line represents the Zemax simulations results and the dots are the measurements.

In the studied system, the main ellipsoidal antenna foci are the confocal point and the target point. One can focus to a different point by axially displacing the first focal point. The displacement of this focus generates a quadratic phase shift over the main aperture that displaces the position of the secondary focus by a certain amount R, [77]. One can change the target plane by shifting the confocal focus. The most convenient way to vary the confocal point is by translating the transceiver in the axial direction a distance d as described in [119] and illustrated in figure 6.1. This produces a better beam quality than displacing the main aperture because the feed reflector has a larger f-number. The scanning mirror rotation can still perform the steering of the beam in the cross-range plane at the refocused distance. If the transceiver is moved far from the feed reflector ($d < 0$) the refocusing distance decreases, and when the transceiver is nearer the reflector ($d > 0$) the focus distance increases.

The whole refocusing system has been simulated with the commercial software Zemax based on ray tracing. It is possible to make, for each refocusing position, a ray tracing and calculate, at the target plane, the radius of each ray with respect to the central one. A measure of the system aberrations is the RMS of all these radiuses. Figure 6.2 shows the transceiver axial translation needed to get each refocusing distances, $R = R_0 + R$. This curve has been obtained by minimizing the RMS radius of the incident rays for each transceiver position. Figure 6.2 also shows the measurements results obtained as explained in section 6.4.

6.3 Characterization of the Refocusing System

The whole refocusing system has been also simulated using the software GRASP. Figure 6.3 shows the simulated fields, plotted in dB as $20\log(|E|^2)$ at the target plane (xy-plane in figure 6.1) for different refocusing distances. The squared field is used in the figures because the radar's received signal is proportional to the product of the transmitted and received antenna patterns, which are the same [44].

To analyze the beamwidth, directly related with the system resolution, a study of the beams radius at -3 dB has been done. This parameter represents the points where the squared field has decayed -3 dB from its maximum and it is represented as a function of the ϕ-coordinate in a polar coordinate system centered in the maximum of $|E|^2$ for each beam. In figure 6.4, the -3 dB radiuses for R = 13.5, 25 and 37.5 m are shown. The beams have a slightly elliptical shape as it can be observed from the variation of the curves as a function of the angular coordinate, but this variation is below 0.1 cm for the three cases. The system beamwidth, shown in figure 6.5, is calculated as the average of the -3 dB radius. There is an increase in the beamwidth as a function of the refocusing distance.

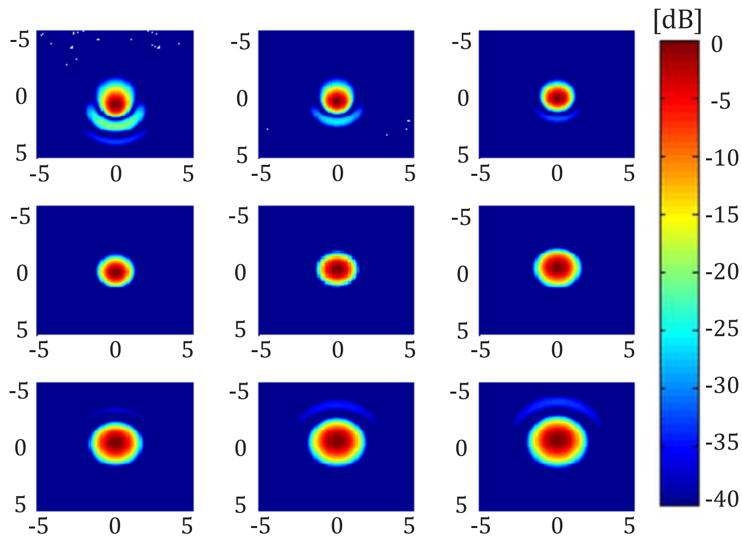

Figure 6.3: Normalized beams $|E|^2$ at different refocusing distances simulated with GRASP.

Even so, values under 1.5 cm are obtained for the whole range.

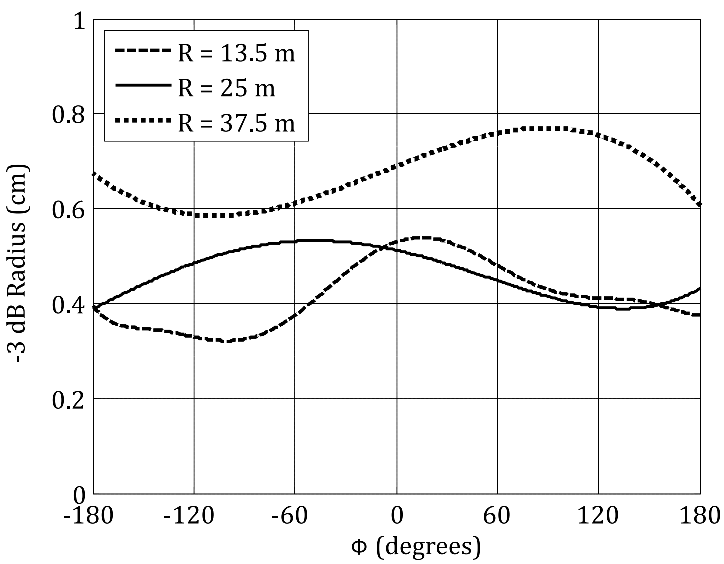

Figure 6.4: -3 dB radius of the simulated beams for 13.5, 25 and 37.5 m refocusing distances.

In order to study the quality of the refocusing system, its performances are compared with those obtained from a single mode Gaussian beam analysis done on an ideal elliptical reflector. A Gaussian beam, is a transverse EM mode which mathematical expression for its complex electric field amplitude can be found by solving the paraxial Helmholtz equation, [49]. Thus, the normalized electric field yields to

$$E(r,z)=\sqrt{\frac{2}{\pi w^2(z)}}e^{\left(-\frac{r^2}{w^2(z)}-jkz-\frac{j\pi r^2}{\lambda R_c(z)}+j\phi_0(z)\right)} \tag{6.1}$$

where z is the axis of propagation, r represents the perpendicular distance from the axis of propagation, w_0 denotes the beam waist radius (the beam radius at $z=0$), $k=2\pi/\lambda$ is the wave number, $R_c(z)$ is the radius of curvature, $w(z)$ is the beam radius and $\phi_0(z)$ is the Gaussian beam shift. These last three parameters are defined as:

$$R_c(z)=z+\frac{1}{z}\left(\frac{\pi w_0^2}{\lambda}\right)^2 \tag{6.2}$$

$$w(z)=w_0\sqrt{1+\left(\frac{\lambda z}{\pi w_0^2}\right)} \tag{6.3}$$

$$\tan\left(\phi_0(z)\right)=\frac{\lambda z}{\pi w_0^2} \tag{6.4}$$

For an ideal uniformly illuminated elliptical reflector focusing at R, the beam's full width to half-maximum (FWHM) is directly proportional to the focusing distance: $FWHM=(\lambda/D)R$. Instead, if the reflector illumination is tapered, as in this case, the theoretical FWHM beamwidth, derived by Gaussian beam approximations, obeys $FWHM=(1.02+0.0135Te(dB))\lambda/DR$, [49], where $Te(dB)=11$ dB is the field taper at the edge of the main aperture for the current configuration. In the case of an elliptical reflector, where the feed is displaced in order to change the focusing distance, this expression sets the lowest possible value of the resolution achievable at any distance by this refocused reflector. Moreover, from this equation we know that the FWHM of the refocused beam will increase with the refocusing distance.

The radar received signal is proportional to the square of the amplitude, $|E|^2$, therefore it is convenient to use as image quality parameter the width of the squared amplitude where its maximum is reduced -3 dB. We will refer as $FWHM_2$ to this parameter. To get this parameter, the expression of the FWHM must be properly normalized. The field amplitude of a Gaussian beam, relative to its maximum value and calculated from equation (6.1), follows the form $|E(r,z)|^2=e^{-r^2/w^2(z)}$, where $w(z)$ is defined as in (6.3). Thus, the associated squared field can be written as $|E(r,z)|^2=e^{-2r^2/w^2(z)}$. Expressing both

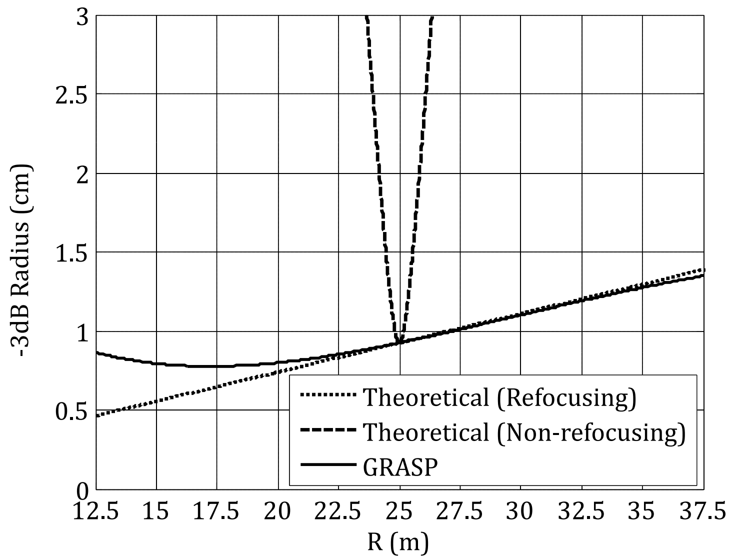

Figure 6.5: Beamwidth average for GRASP simulations (solid line). The dotted line represents the beamwidth that could be theoretically achieved by focusing the reflector using 6.5, and the dashed line represents the beamwidth if no refocusing is used.

equations in dB and relating the radius of the Gaussian beam at -3 dB, one can find a relationship between the FWHM of the one and two-way signals as:

$$FWHM_2 = FWHM/\sqrt{2} \tag{6.5}$$

This equation can be used to compare the performances of the refocused reflector system to those of an elliptical reflector with the same aperture dimension and a nominal focusing distance that changes in the same range of the refocused one, R, as shown in figure 6.5. Theoretical and simulated results of the beam widths have very good agreement for almost the whole refocusing range. The larger differences occur at the lowest distances where there are more phase aberrations.

The dashed line in figure 6.5 represents the theoretical value of the radius at -3 dB if no refocusing is used. To get this curve, the beam waist (calculated as the value of the beam radius at the nominal distance) is obtained by equating it to the $FWHM_2$ at the nominal refocusing distance. From these curves one can observe the need for refocusing outside the nominal position due to the rapid growth of the beam.

Figure 6.6 shows the field profile at the horizontal and vertical planes, xz and yz planes in figure 6.1, respectively, versus the refocused distance. The simulated beamwidth contours, obtained as the half power beamwidth in each plane, are also represented in figure

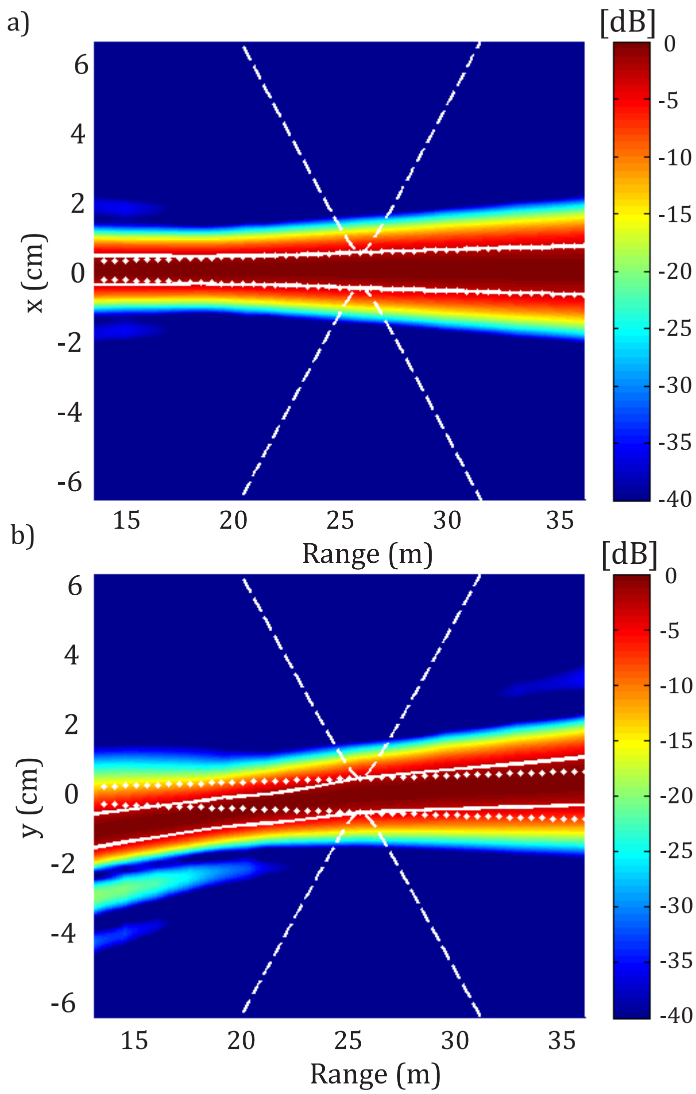

Figure 6.6: Normalized beams field profile, simulated with GRASP in the (a) horizontal and (b) vertical planes, as a function of the refocusing distance. The dotted and solid lines are the theoretical, equation (6.5), and simulated beamwidth contours respectively. The dashed lines represents the beamwidth if no refocusing is accomplished.

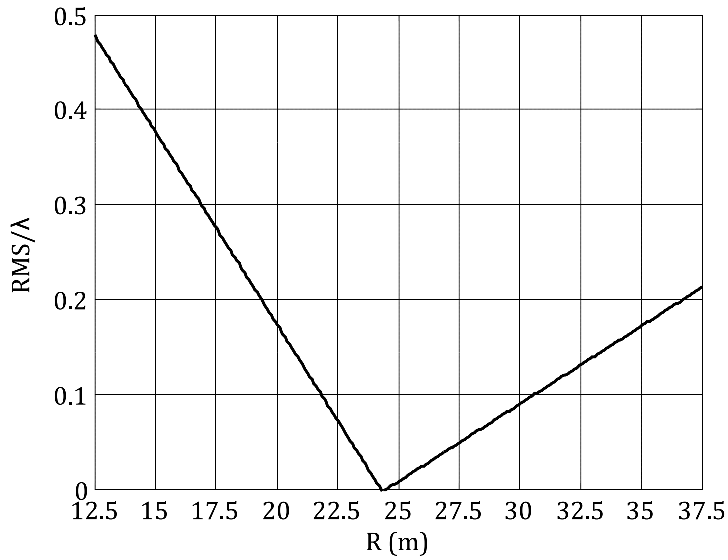

Figure 6.7: RMS error normalized by the wavelength versus the refocusing range.

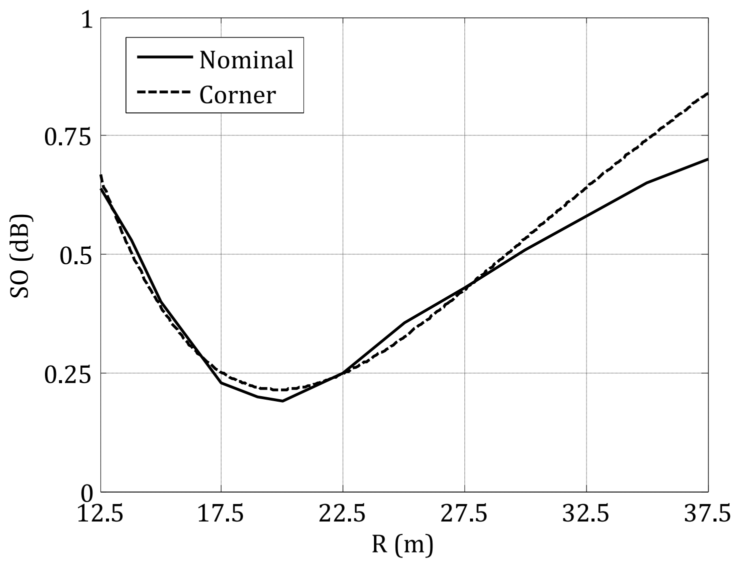

Figure 6.8: Refocusing system spillover as a function of the range. The solid line represent the beam in the center of the FoV and the dashed lines represents the beam in a corner of the FoV.

6.6 together with the theoretical ones obtained with 6.5. Both theoretical and simulated lines are in very good agreement for almost the whole range in the horizontal plane. However, the field axis along the range for the vertical plane is not fixed at 0 cm. This means that the beam in this plane presents a shift. This deviation appears as a consequence of the irregular illumination of the main reflector when the transceiver is moved because of the offset configuration. The tilt in the beam could be compensated by including a transversal displacement of the transceiver combined with the axial one. For the current configuration, the beam's tilt is, in the worst case, comparable to a beamwidth and therefore it is not significant for the image quality. Furthermore, including a transversal displacement would lead to a lower refocusing speed because two different linear motors will be needed. Although the simulated lines do not overlap the theoretical ones in figure 6.6 (right), one can appreciate that the absolute beamwidth value is similar in both cases. Therefore, we can conclude that the refocusing method provides a resolution comparable to the one obtained by an ideal elliptical reflector focusing at each of the analyzed distances.

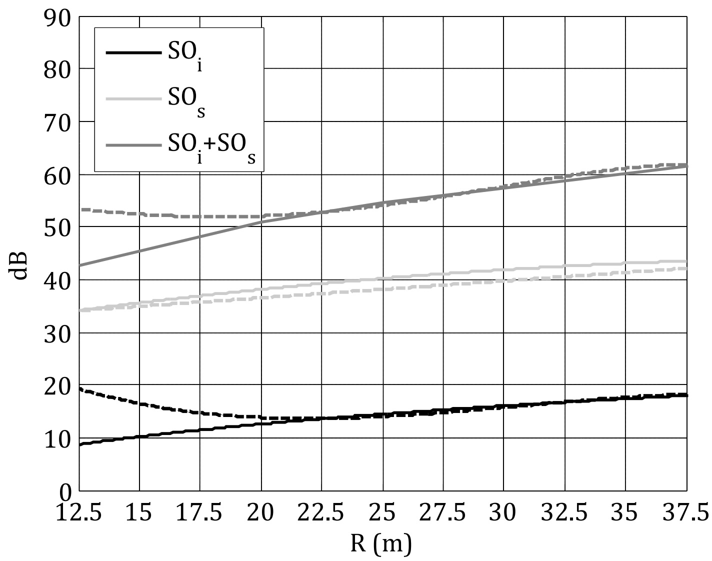

Figure 6.9: Incident (SO_i), scattered (SO_s) and total spillover for a 3 mm diameter metal sphere. The solid lines represent the theoretical values and the dashed lines the GRASP simulations.

Simulated results do not fit the theoretical values in the lower ranges, see figures 6.3, 6.5 and 6.6. At those ranges, there are significant phase errors in the quasioptical system resulting in non-Gaussian beams. The beams start to have asymmetric secondary lobes and the Gaussian shape is lost. Figure 6.7 shows the system optical aberrations calculated as the RMS error normalized by the wavelength. The RMS increases steeply as the range decreases from the nominal distance. Instead, it maintains a low value in the other part of the range.

The system efficiency is directly related with the system's SO. Figure 6.8 shows the simulated SO versus the range for two positions of the flat rotating mirror: the nominal position (beam at the center of the FoV) and the rotated position (beam at the corner of the FoV). The SO is under 0.75 dB for almost the whole refocusing range, leading to high efficiencies values above 85%. The sub reflector is oversized to reduce the SO, [119], and

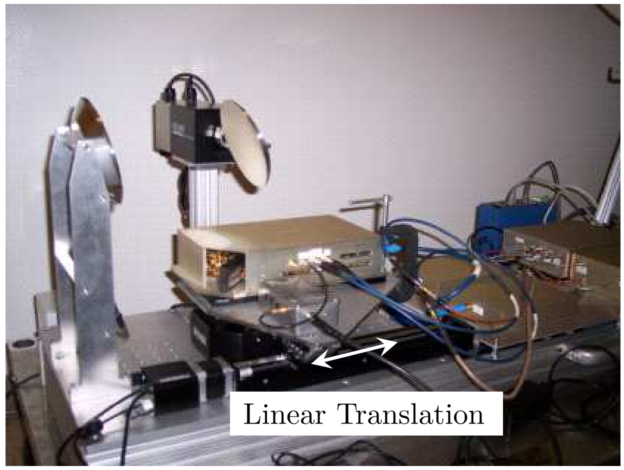

Figure 6.10: Implementation of the refocusing system.

the values obtained are limited by the main reflector aperture that cannot be modified for the current application.

The spillover losses when a 3 mm metal sphere is imaged have also been simulated in GRASP and calculated using simplifications for the whole range beams. These losses are directly related to the system signal-to-noise (SNR) ratio, shown in the last section. The terms that most affect the SNR are: the incident spillover (SO_i) and the scattered spillover (SO_s). SO_i is related with the power lost when the beam impinges on the small sphere. This term has been theoretically calculated as the fractional power outside the bead radius if an incident Gaussian beam is considered:

$$\mathrm{SO}_i = 1 - e^{-2\alpha} \tag{6.6}$$

where $\alpha = r_s^2/w_0^2$, being r_s the radius of the considered sphere. The other term of the spillover, SO_s, is related with the power scattered by the sphere, when it is illuminated with the beam, and not intercepted by the main reflector. As the impinging beam is much larger than the sphere diameter, we can suppose that the sphere has a uniform illumination and, therefore, it scatters an isotropic field. Accordingly, SO_s can be calculated as the ratio between the solid angle subtending by the main reflector and the solid angle of a whole sphere.

$$\mathrm{SO}_s = \frac{\Delta\Omega_s}{\Delta\Omega_i} = \frac{2\pi(1 - cos\theta)}{4\pi} \tag{6.7}$$

where θ would be the reflector edge angle.

In figure 6.9, SO_i and SO_s are shown for both the theoretical calculation and the GRASP simulations. Simulations and theoretical results provide similar results. The mismatch in the lower range of the incident spillover is related with the loss in the Gaussian shape of the beams due to the system phase errors mentioned before.

6.4 Measurements

The refocusing mechanical system has been manufactured, as shown in figure 6.10, and integrated with the entire antenna system. The high frequency circuitry is confined within a box. This box is displaced to achieve the refocusing, see figure 6.10. Outside this box the connections are at low frequencies. This packaging protects the high frequency transceiver while is moved.

To qualitatively verify that the radar beam refocuses in range with a linear translation of the transceiver, a thin nylon string with nine equally spaced 3 mm diameter brass beads glued to it was suspended at an angle moving upward with distance over a range span of about 4 m. With this configuration, a single image frame capture will show all of the beads simultaneously, but with different degrees of resolution because of the change in the radar beamwidth over the range where the beads are located. Figure 6.11 shows nine range-slices (at the nine ranges of the suspended beads) from five such images acquired at five different positions of the transceiver. From this data, it is immediately clear that as the transceiver moves forward, beads at further and further distances come into focus. To determine the optimum transceiver displacement position for a target at a given range, the focus quality and return signal levels of a small target at that range was maximized as a function of the transceiver position. The results are shown in figure 6.2, and they fit with the simulated values.

The beam shapes of the 3 mm bead targets at ranges spanning $13 - 38$ m have also been carefully measured with the radar. Figure 6.12 shows the normalized field measured for different refocusing positions. If we qualitative compare the measured beams with the simulated ones, the measurements exhibit a strong elliptical shape even for the nominal position. In figure 6.13 the radius at -3 dB for three refocusing positions, 13.5 m, 25.5 m and 37.5 m, are shown. The variation of the curves is higher than 1 cm in the worst case (37.5 m). This is a result of optical misalignment in the experimental setup because at the nominal position ($R_0 = 25$ m) the beam is already elliptical. In previous measurements, [45], the system was correctly aligned and the beam in the nominal position was shown not

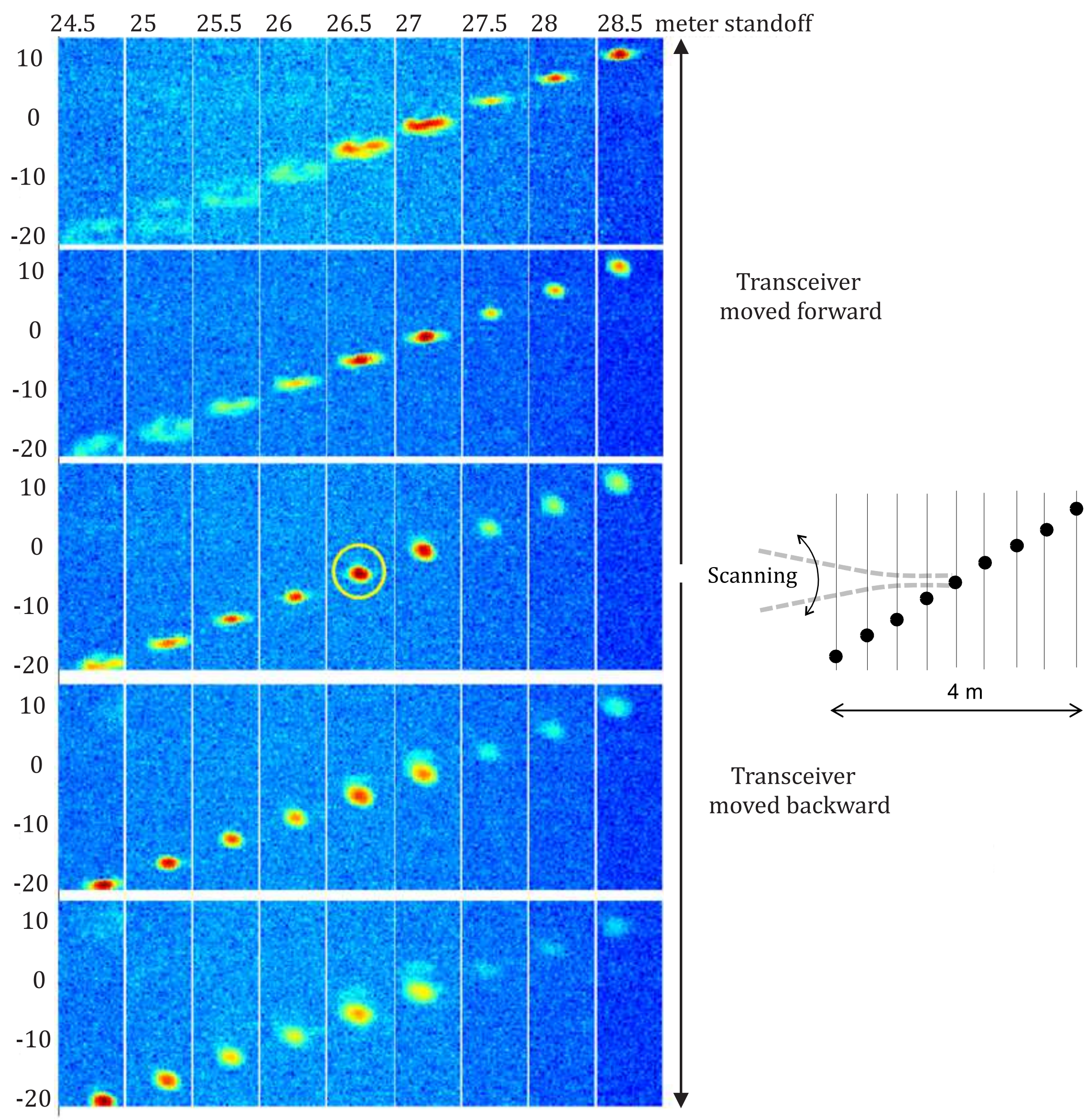

Figure 6.11: Single-images of the 3 mm spheres string captured at multiple ranges for the refocusing range validation and a scheme of the beads image acquisition.

to have this problem. The focus of this chapter is the validation of the refocusing concept. For that, we should consider the misalignment when comparing the simulations and the measurements. Another factor to consider when comparing these results is the way in which the measurements were done, see figure 6.11. The beams in figure 6.12 were obtained by imaging brass beads that were suspended at an angle moving upward with distance over a range span of about 4 m and a shift in the y axis of up to $\pm$ 10 cm. Therefore the measured

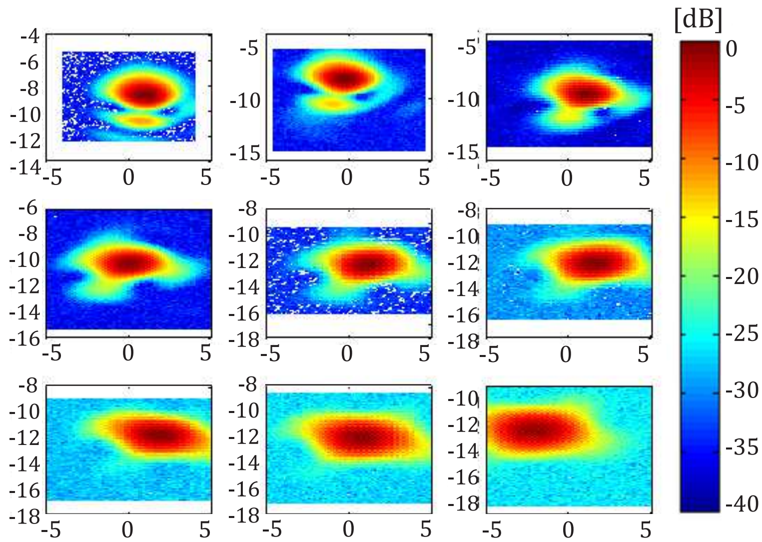

Figure 6.12: Measured normalized beams $|E|^2$ at different refocusing distances.

beams were not perfectly aligned with the reflector center. Even so, one can observe that the beamwidths increase with the range as in the simulations. Furthermore, the secondary lobes for the lower values of the range also appear as predicted by the simulations, showing a good agreement with the simulations.

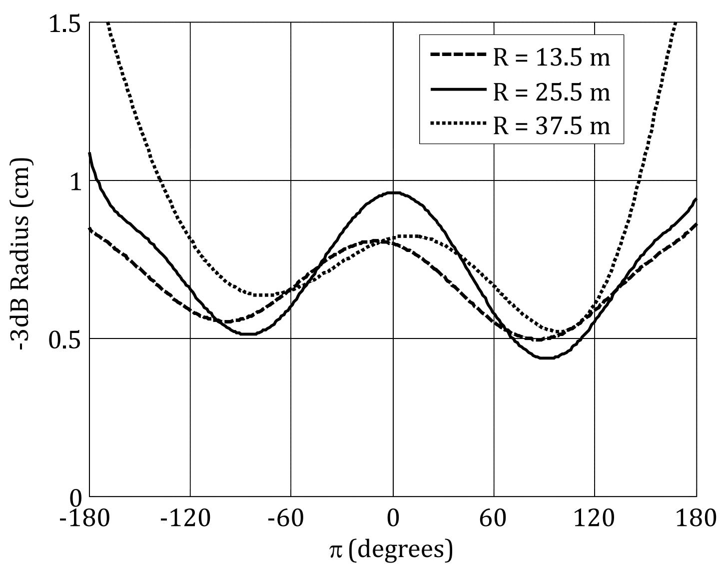

Figure 6.13: -3 dB radius of the measured beams for 13.5, 25.5 and 37.5 m refocusing distances.

Figure 6.14 shows the beamwidth of the measurements, taken from the images of figure

6.12 and calculated as the average of the -3 dB radius angular variation, compared with the simulated results. Although the measured beamwidth does not agree with the simulated lines due to the misalignment in the system mentioned before, one can appreciate that the variation of the beamwidth as the refocusing distance increases is the same in both cases.

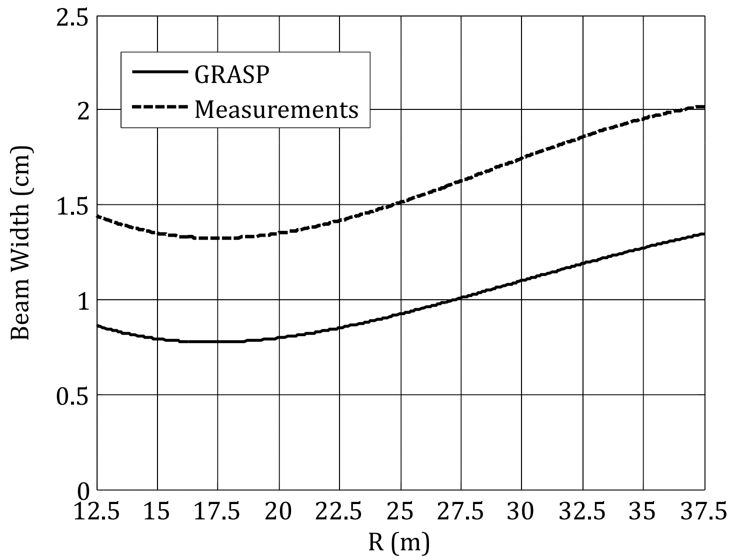

Figure 6.14: Beamwidth average for GRASP simulations (solid line) and measurements (dashed line).

6.5 Imaging Results

Finally, the refocusing system has been tested by acquiring through-clothes images of concealed weapons on a mannequin. Figure 6.16 shows 3D radar data of a mannequin, figure 6.15, torso with three PVC pipes concealed by a T-shirt, similar to the scenario described in [5]. With refocusing, very clear images of the concealed pipes can be acquired with the mannequin at standoff ranges from 13.5 to 37.5 m, albeit with diminished fields of view for the closer ranges. The quality of the image is very similar in all cases, proving the practical application of the system implementation presented here.

In figure 6.17, the average beam signal-to-noise ratio for the mannequin images is shown. There is a drop-off of less than 10 dB for this target from the nearest to the farthest standoff ranges. The minimum SNR is above 25 dB for the larger range which means there is enough signal for good quality images in the whole range. In this figure also the SNR of a 3 mm brass bead is shown compared with the GRASP simulation results. The simulated SNR is obtained directly from the total system SO, when a 3 mm metallic sphere is placed at the

Figure 6.15: Images of the 3 PVC pipes and the mannequin uncovered and covered with the T-shirt.

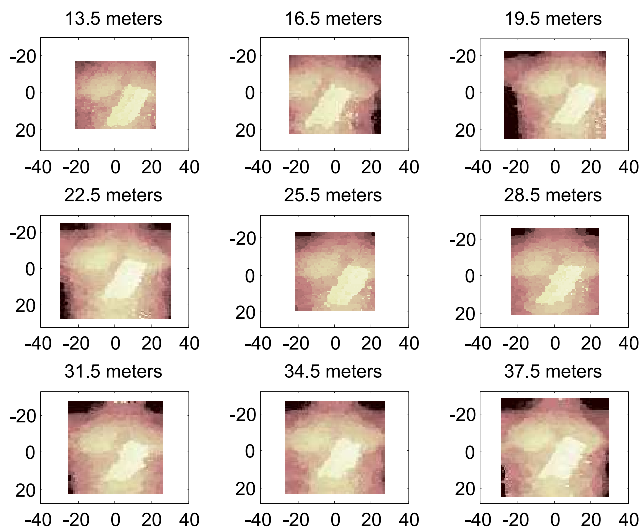

Figure 6.16: Imaging of mannequin with concealed plastic pipes for different values of the refocusing distance.

target plane, and normalized to the measured SNR at the nominal position

6.6 Conclusions

In this contribution we have presented a practical implementation of a refocusing optical system that allows displacing the standoff distance of a THz imaging radar by translating mechanically the transceiver. The system has been successfully characterized with simulations and experimentally leading to very good imaging quality over the standoff distances of 12.5 m 37.5 m. The measured antenna performances, in terms of beamwidth and optimum focus position, resemble the simulations. The system resolution, measured as the beamwidth, is kept below 1.5 cm and the spillover under 1 dB for the whole range. Because of this low spill over and well-focused beams achieved, the signal to noise ratio is over 25 dB allowing fast high quality imaging over the whole range span. The presented refocusing

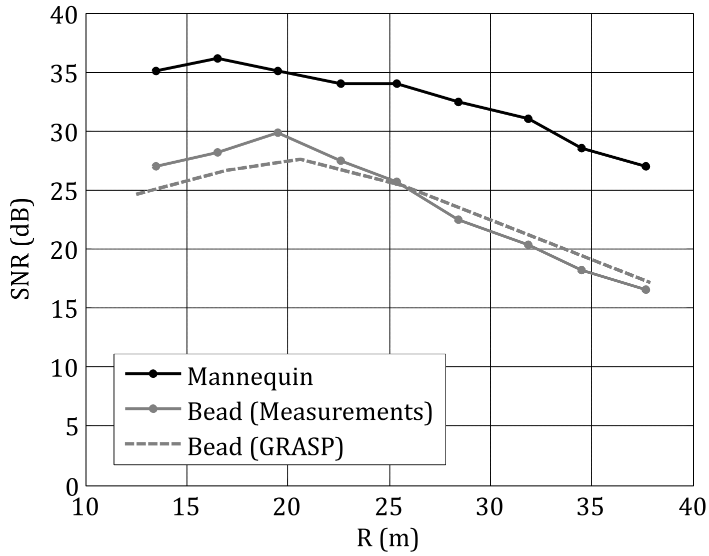

Figure 6.17: Signal to noise ratio for each position of the refocusing range when the mannequin and a 3 mm brass bead are imaged. The GRASP results are shown for the bead.

system is able to image persons in movement with high quality.

Chapter 7

Conclusions

This doctoral thesis has focused on the development of quasioptical solutions to solve some of the limitations present in THz imaging systems. THz frequency has nowadays a large number of potential uses. Throughout this thesis, two of the most outstanding applications of submillimeter waves have been addressed: Space and security imaging systems. In both cases, the use of quasioptical components, specifically lenses and mirrors, has been exploited to improve the systems performance. Besides, in order to facilitate the design process and further understand the nature of the problems faced, a deep analysis of the different configuration treated has been performed by using both in-house developed techniques and commercial software adapted to each specific situation. Due to the different characteristics of the applications studied in this work, the research has been divided in two main study areas.

7.1 Absorbers under THz Focusing Systems

Kinetic Inductance Detectors are a promising alternative to the traditional bolometers for the new generation of THz instruments for Space applications, due to the extreme ease of integration in large array configuration that they offer. The coupling of the THz radiation onto the KID resonator is a crucial point since, in astronomy, extremely low SNRs have to be detected. The approach studied during this thesis to perform this radiation coupling has been absorber-based KIDs. In this configuration, the absorption is achieved by matching the impedance for the structure with the incoming signal. Therefore, the geometry optimization becomes more difficult than in antenna cases since it has to be done together with the resonator design. In real scenarios, the large arrays of KIDs would be place in the focal plane of a telescope. Furthermore, in order to improve the sampling, optical efficiency and mutual coupling between the elements of the array, silicon lenses on top of each element can be used as an external radiation coupling mechanism. This lenses are typically characterized by small F/D ratios so the standard normal plane wave incidence analysis is not appropriate any more. In this first part of the thesis, an analytical spectral model able to characterized absorbers distributed on the focal plane of THz focusing systems, with large of small F/D ratios, has been developed.

An equivalent network for the analysis of linearly polarized absorbers under general plane wave incidence has been firstly implemented. The network is obtained by making used of the pertinent spectral Green's functions for stratified media. Three are the main achievement of this network. Firstly, it separates the treatment of the average field in the absorber plane and the electric current on the lossy strips. In this way, we obtain a direct relationship between the absorbed power and the geometrical parameters. A second achievement is the possibility of using the network also when higher order FW play an important role in the analysis, by introducing a dedicate analytical impedance term that take into account these effects. The third main achievement is that the circuit allows the assessment of the coupling between the TE and TM waves, by introducing dedicate transformers. Furthermore, all the components of the circuit are analytical so it is straightforward to use it. The validity of the network has been proved with CST simulations. Apart from the model characterization advantages, the network has been used to design some optimized absorber geometries showing efficiencies larger than 90% over a bandwidth of up to 2.6 octaves. It has been also shown that the use of a dense dielectric on top of the absorber provides high efficiency over larger bandwidths than the ones obtained in other configurations like free-standing absorbers printed on thin dielectric membranes.

A simple method based on Fourier Optics approximations has been derived in order to get a plane wave representation of electromagnetic focal plane fields. The limits of validity of these approximations within the THz range were not established. Therefore, an effort has been made in order to clarify the region of applicability of this method. This region is given as a circle in the focal plane with a specific diameter, and it depends on the focusing system aperture dimension, the system f-number (F/D) and the wavelength. Furthermore, the plane wave representation derived has been used together with the equivalent network for linear absorbers developed for a single plane wave incidence. In this way, the total current on the strips, when the absorber is located under a focusing system, is calculated by a coherent integration of the current due to each plane wave. Therefore, a complete tool for the analysis of absorbers under focusing systems with both, large and small F/D ratios, is provided. The methodology has been validated with alternative numerical techniques and with time-consuming full-wave simulations for two specific configurations: a dielectric elliptical lens and a parabolic reflector.

The overall method introduced in this part of the thesis is a powerful technique as it simply links spectral Green's functions, useful for the characterization of the field propagation in planar stratified media, with the focal fields in focusing systems.

7.2 New Capabilities for a THz Imaging Radar

In the second part of this thesis, two quasioptical solution have been applied, and measured, to an existing THz imaging radar for security applications. The radar was developed at JPL and it operates at 675 GHz. It effectively detects concealed person-borne threats with frame rates of 1 Hz. The goals of this part of the thesis were to further reduce the radar's acquisition time and to provide the system with refocusing capabilities without changes in the scanning optics, the source power, or in the back-end electronics hardware.

In order to increase the radar imaging speed up to near-video rates, THz transceivers linear arrays will be used in the future. In this work, we have presented a study of how all quasioptical time-delay beam multiplexing can work for an array of multiple beams simultaneously. The increase of the imaging speed is achieved by scanning the FoV with multiple pixels obtained from splitting each transmitted beam into two using a quasioptical waveguide. It has been shown that the multiplexing of large arrays is not trivial since aberrations and spillover in the system emerge. These problems are solved by increasing the f-number of the quasioptical elements. A six-elements array has been studied, obtaining a resolution of 1.2 cm with a 0.89 dB spillover. The last element of the array is displaced 24 half-power beamwidths from the FoV center, which means that a compact array of 48 elements would have a similar beam quality. Thus, the multiplexing technique has been proved to be a feasible and hardware-efficient method to further reduce the acquisition time of a large linear THz transceiver array, in the final goal of a near-video rate imaging.

Finally, the system has been provided with refocusing capabilities by means of a practical implementation of a simple and classical optical solution: a mechanical translation of the transceiver. The radar standoff distance was initially fixed to 25 m. After the refocusing has been implemented, a range between 12.5 m and 37.5 m can be imaged. The system has been characterized in terms of beam quality and spillover resulting in a resolution below 1.5 cm and less than 1 dB of spillover over the whole range. The refocusing was implemented in the actual system and the measurements resembles the values obtained in the simulations.

7.3 Future Research Lines

There are several research lines that can be thought as a continuation of the work presented here. Indeed, some of these lines are currently being developed within our research group.

The future of THz systems is in integrated focal plane array configuration. The optimization of the architecture of antenna arrays will play an important role in the development of these systems. In order to extend the framework presented in this thesis for future coherent cameras with pixels widely distributed from the real focus point, one needs to extend the methodology developed in Chapter 2. In this method, to obtain the PWS representation based on FO, the quadratic phase of the field, $e^{-jk\frac{\rho_f^2}{2R}}$, is neglected. This approximation is valid when the element analyzed is in the focal point of the focusing system. However, when analyzing elements off-focus, the information of this quadratic phase is relevant and must be considered. A natural next step for the work developed here is the extension of the plane wave representation to the entire region where the FO representation is valid. The principal mathematical step towards this extension is recognizing that the quadratic phase can be linearly approximated around a certain point in the focal plane. This point can be selected as the center of each array element in the focal plane. In order to maintain a PWS representation, it is necessary to introduce a change in the reference system, and obtain a derivation of a local PWS around this new reference system origin.

Another possible research line, is the analysis of the system imaging speed. This is a key parameter in the effectiveness of a radiometric system. This speed depends on the receiver sensitivity, which is proportional to the reception efficiency. The signal to noise ratio of a passive detector is directly proportional to the actual power received in the focal plane array. In order to optimize the acquisition speed for a certain level of signal to noise ratio, the received power needs to be maximized. The representation for power absorbers presented here could be used in the future to optimize the array configuration and to enable fast beam forming techniques in the presence of optical systems.

As mention before, the use future large heterodyne arrays in the THz range, due to the development of integrated technology, is near to be feasible. For the development of large integrated arrays technology that could be used for imaging applications such as active and interferometry imaging, the use of planar antennas in combination with dielectric lenses is envisaged. Planar antennas placed on high dielectric wafer feeding a dielectric lens can achieve high efficiencies. However, lens based antenna solution have not been much considered due to the higher mutual coupling compared to horn based ones. As a third research line after the work presented here, we propose to investigate the level of mutual coupling that can be achieved with lens array configurations, studying the main causes for this mutual coupling and explore possible mitigation strategies. Apart from the THz heterodyne array configurations, also THz direct detection instruments, as the radiometric arrays of KIDs, could benefit from this study. The actual impact of the spillover of these detectors in the noise can only be well estimated if the mutual coupling between the lens arrays is understood. Furthermore, as explained in Chapter 5, the mutual coupling between the transceivers can increase the phase noise in a frequency-modulated continuous-wave radar. Therefore, the study of mutual coupling could be a key point in the near future development of THz array technology.

Appendix A

Asymptotic Term of the Impedance

In this appendix, an expression representing the asymptotic behavior of the grid impedance is derived. We start by considering the expression of the impedance in the spectral domain:

$$Z^{m_y \neq 0}(k_x) = \frac{-1}{d_y} \sum_{m_y \neq 0} G(k_x, k_{ym}) \mathrm{sinc}^2 \frac{k_{ym} w}{2} \tag{A.1}$$

and recognizing the sinc function in equation (A.1) as Fourier transform of the rect function

$$Z^{m_y \neq 0}(k_x) = \frac{-1}{d_y} \frac{1}{w^2} \int_{-w/2}^{w/2} \int_{-w/2}^{w/2} S(k_x) dy' dy \tag{A.2}$$

where $S(k_x)$ is defined in order to get a more compact expression as follows:

$$S(k_x) = \sum_{m_y \neq 0} G(k_x, k_{ym}) e^{j k_{ym} (y - y')}. \tag{A.3}$$

We are interested in a number of different geometrical configurations, described in figure 3.5. In all cases, for large spectral numbers k_{ym}, the Green's function tends asymptotically to the same value that is assumed by the configuration associated with the dipole placed in the interface of two semi-infinite homogeneous dielectric layers, as case II. in figure 3.5, where ε_{ru} and ε_{rd} will be, in general, the relative permittivity of the media located immediately above and below the grid, respectively. The Green's function of two infinite media follows the form

$$G(k_x, k_{ym}) = -\frac{\xi_0}{k_0} \left(\frac{k_0^2}{k_{zu} + k_{zd}} - \frac{k_x^2}{\varepsilon_r^d k_{zu} + \varepsilon_r^u k_{zd}} \right). \tag{A.4}$$

The asymptotic behavior of (A.4) when k_{ym} is very large compared to the wave vector amplitude k_i, in both $i = 1,2$ media, can be calculated by considering that $k_{zi} = (k_i^2 - k_\rho^2)^{1/2} \to -jk_\rho$. Thus,

$$G_{as}(k_x, k_{ym}) = \frac{\xi_0}{k_0}\left(\frac{k_0}{2} - \frac{k_x^2}{k_0(\varepsilon_r^d + \varepsilon_r^u)}\right) \tag{A.5}$$

where $G_{as}(k_x, k_{ym})$ is the asymptotic Green's function.

Assuming small periods ($k_{yi} \ll 2\pi m_y/d_y$), the asymptotic Greens function can be approximated as

$$G_{as}(k_x, k_{ym}) \approx \frac{-\xi_0 d_y}{2\pi|m_y|} j\left(\frac{k_0}{2} - \frac{k_x^2}{k_0(\varepsilon_r^d + \varepsilon_r^u)}\right) \tag{A.6}$$

and the asymptotic expression of the function $S(k_x)$ can be represented as

$$S_{as}(k_x) = \frac{-\xi_0 d_y}{2\pi} j\left(\frac{k_0}{2} - \frac{k_x^2}{k_0(\varepsilon_r^d + \varepsilon_r^u)}\right) e^{jk_{yi}(y-y')} \sum_{m_y \neq 0} \frac{1}{|m_y|} e^{-j\frac{2\pi m_y}{d_y}(y-y')}. \tag{A.7}$$

Then, by using the mathematical identity $\sum_{m=0}^{\infty} \frac{1}{m} e^{j\alpha m}$, for $k_{yi} = 0$ we obtain the asymptotic term of the impedance by substituting (A.7) into (A.2)

$$\begin{gathered} Z_{as}(k_x) = jX_{as}(k_x) = j\frac{-\xi_0}{2\pi w^2}\left(\frac{k_0}{2} - \frac{k_x^2}{k_0(\varepsilon_r^d + \varepsilon_r^u)}\right) \\ \left[\int_{-w/2}^{w/2}\int_{-w/2}^{w/2} \ln\left(1 - e^{j\frac{2\pi}{d_y}(y-y')}\right) dy'dy + \int_{-w/2}^{w/2}\int_{-w/2}^{w/2} \ln\left(1 - e^{-j\frac{2\pi}{d_y}(y-y')}\right) dy'dy\right] \end{gathered} \tag{A.8}$$

One can further approximate to the first order the exponentials, $e^{j\alpha} \approx 1 + j\alpha$, since the spatial integrations are limited from $w/2$ to $w/2$ and, therefore, $(y - y')$ is small compared with d_y:

$$\begin{gathered} Z_{as}(k_x) = jX_{as}(k_x) = j\frac{-\xi_0}{2\pi w^2}\left(\frac{k_0}{2} - \frac{k_x^2}{k_0(\varepsilon_r^d + \varepsilon_r^u)}\right) \\ \left[-j\pi w^2 + 2\int_{-w/2}^{w/2}\int_{-w/2}^{w/2} \ln\left(-j\frac{2\pi}{d_y}(y - y')\right) dy'dy\right] \end{gathered} \tag{A.9}$$

Finally, the double spatial integration can be performed analytically leading to

$$\int_{-w/2}^{w/2}\int_{-w/2}^{w/2} \ln\left(-j\frac{2\pi}{d_y}(y-y')\right) dy'dy = w^2\left[\ln\left(\frac{2\pi w}{d_y}\right)+\frac{\pi}{2}j-\frac{3}{2}\right] \tag{A.10}$$

Thus, the overall asymptotic impedance contribution can be expressed as:

$$X_{as}(k_x) = \frac{\xi_0}{\pi}\left(\frac{k_0}{2}-\frac{k_x^2}{k_0(\varepsilon_r^d+\varepsilon_r^u)}\right)\left[\ln\left(\frac{d_y}{2\pi w}\right)+\frac{3}{2}\right] \tag{A.11}$$

In the cases where higher-order modes are relevant (large periods, thin dielectric slabs or closed backing reflectors), not only the fundamental term $m_y = 0$ has to be included in the analytical impedance but also the first two higher order modes $m_y = \pm 1$. In the cases where these modes will not be propagating, their impedance, $Z^{m_y=\pm 1}$, will be imaginary. Therefore, we include it in the analytical impedance. In this configuration, the asymptotic term of the impedance has to be calculated by excluding also these two terms from the summation in (A.1). Following similar steps than the ones explained in this appendix, one arrives to a new expression of the analytical reactance including the first two higher order modes:

$$X_{as}^{HM}(k_x) = \frac{\xi_0}{\pi}\left(\frac{k_0}{2}-\frac{k_x^2}{k_0(\varepsilon_r^d+\varepsilon_r^u)}\right)\left\{\ln\left(\frac{d_y}{2\pi w}\right)+\frac{3}{2}+\frac{d_y^2}{2w^2\pi^2}\left[\cos\left(\frac{2\pi w}{d_y}\right)-1\right]\right\} \tag{A.12}$$

List of Acronyms

BEM Boundary Element Method

CGRS Confocal Gregorian Reflector System

CPW CoPlanar Waveguide

EM Electromagnetic

FDTD Finite Difference Time Domain

FEM Finite Element Method

FFT Fast Fourier Transform

FMCW Frequency-Modulated Continuous-Wave

FW Floquet Wave

FWHM Full Width to Half-Maximum

FO Fourier Optics

FoV Field of View

GO Geometrical Optics

GTD Geometrical Theory of Diffraction

HEB Hot-Electron Bolometer

HPBW Half Power Beam Width

JPL Jet Propulsion Laboratory

KID Kinetic Inductance Detector

LEKID Lumped Element Kinetic Inductance Detector

LHS Left-Hand Side

MoM Method of Moments

PO Physical Optics

PWS Plane Wave Spectrum

PTD Physical Theory of Diffraction

QOWG Quasi-Optical WaveGuide

RHS Right-Hand Side

RMS Root Mean Square

SAFARI SpicA FAR-infrared Instrument

SIS Superconductor-Insulator-Superconductor

SNR Signal-to-Noise Ratio

SO SpillOver

SRON Space Research Organization of the Netherlands

STJ Superconducting Tunnel Junction

TES Transition Edge Sensor

UTD Uniform Theory of Diffraction

UAT Uniform Asymptotic Theory

List of Figures

List of Tables

Bibliography

[1] P. Siegel, "Terahertz technology," *Microwave Theory and Techniques, IEEE Transactions on*, vol. 50, no. 3, pp. 910–928, Mar 2002.

[2] J. M. Chamberlain, "Where optics meets electronics: Recent progress in decreasing the terahertz gap," *Philos. Transactions, Series A, Mathematical, Physical, and Engineering Sciences*, vol. 362, pp. 199–213, 2004.

[3] M. Tonouchi, "Cutting-edge terahertz technology," *Nature photonics*, vol. 1, no. 2, pp. 97–105, 2007.

[4] J. F. Federici, B. Schulkin, F. Huang, D. Gary, R. Barat, F. Oliveira, and D. Zimdars, "Thz imaging and sensing for security applications - explosives, weapons and drugs," *Semiconductor Science and Technology*, vol. 20, no. 7, p. S266, 2005.

[5] K. Cooper, R. Dengler, N. Llombart, B. Thomas, G. Chattopadhyay, and P. Siegel, "THz imaging radar for standoff personnel screening," *Terahertz Science and Technology, IEEE Transactions on*, vol. 1, no. 1, pp. 169–182, Sept 2011.

[6] P. Siegel, "Terahertz technology in biology and medicine," in *Microwave Symposium Digest, 2004 IEEE MTT-S International*, vol. 3, June 2004, pp. 1575–1578 Vol.3.

[7] V. Parshin, M. Tretyakov, M. Koshelev, and E. Serov, "Modern resonator spectroscopy at submillimeter wavelengths," *Sensors Journal, IEEE*, vol. 13, no. 1, pp. 18–23, Jan 2013.

[8] J. Waters, "Submillimeter-wavelength heterodyne spectroscopy and remote sensing of the upper atmosphere," *Proceedings of the IEEE*, vol. 80, no. 11, pp. 1679–1701, Nov 1992.

[9] B. Drouin, K. Cooper, R. Stachnik, and J. Pearson, "Submillimeter wave spectroscopy and the search for life on planets," in *Infrared, Millimeter and Terahertz Waves, 2008. IRMMW-THz 2008. 33rd International Conference on*, Sept 2008, pp. 1–3.

[10] H. Zhong, J. Xu, X. Xie, T. Yuan, R. Reightler, E. Madaras, and X.-C. Zhang, "Nondestructive defect identification with terahertz time-of-flight tomography," *Sensors Journal, IEEE*, vol. 5, no. 2, pp. 203–208, April 2005.

[11] J. Federici and L. Moeller, "Review of terahertz and subterahertz wireless communications," *Journal of Applied Physics*, vol. 107, no. 11, 2010.

[12] T. Kleine-Ostmann and T. Nagatsuma, "A review on terahertz communications research," *Journal of Infrared, Millimeter, and Terahertz Waves*, vol. 32, no. 2, pp. 143–171, 2011.

[13] G. Chattopadhyay, "Submillimeter-wave coherent and incoherent sensors for space applications," in *Sensors*, ser. Lecture Notes Electrical Engineering, S. Mukhopadhyay and R. Huang, Eds. Springer Berlin Heidelberg, 2008, vol. 21, pp. 387–414.

[14] J. Zmuidzinas, J. W. Kooi, J. Kawamura, G. Chattopadhyay, B. Bumble, H. G. LeDuc, and J. A. Stern, "Development of sis mixers for 1 thz," vol. 3357, 1998, pp. 53–62.

[15] A. Karpov, D. Miller, J. Stern, B. Bumble, H. LeDuc, I. Mehdi, R. Lin, and J. Zmuidzinas, "Low noise 1 thz sis mixer for stratospheric observatory: Design and characterization," *Applied Superconductivity, IEEE Transactions on*, vol. 21, no. 3, pp. 616–619, June 2011.

[16] J. Gao, M. Hajenius, Z. Yang, J. Baselmans, P. Khosropanah, R. Barends, and T. Klapwijk, "Terahertz superconducting hot electron bolometer heterodyne receivers," *Applied Superconductivity, IEEE Transactions on*, vol. 17, no. 2, pp. 252–258, June 2007.

[17] T. Crowe, R. Mattauch, H. Roser, W. Bishop, W. Peatman, and X. Liu, "Gaas schottky diodes for thz mixing applications," *Proceedings of the IEEE*, vol. 80, no. 11, pp. 1827–1841, Nov 1992.

[18] M. Gaidis, H. Pickett, C. Smith, S. Martin, R. Smith, and P. Siegel, "A 2.5-thz receiver front end for spaceborne applications," *Microwave Theory and Techniques, IEEE Transactions on*, vol. 48, no. 4, pp. 733–739, Apr 2000.

[19] E. Ojefors, U. Pfeiffer, A. Lisauskas, and H. Roskos, "A 0.65 thz focal-plane array in a quarter-micron cmos process technology," *Solid-State Circuits, IEEE Journal of*, vol. 44, no. 7, pp. 1968–1976, July 2009.

[20] B. Cabrera, R. M. Clarke, P. Colling, A. J. Miller, S. Nam, and R. W. Romani, "Detection of single infrared, optical, and ultraviolet photons using superconducting

transition edge sensors," *Applied Physics Letters*, vol. 73, no. 6, pp. 735–737, 1998.

[21] B. Karasik, A. Sergeev, and D. Prober, "Nanobolometers for thz photon detection," *Terahertz Science and Technology, IEEE Transactions on*, vol. 1, no. 1, pp. 97–111, Sept 2011.

[22] P. K. Day, H. G. LeDuc, B. A. Mazin, A. Vayonakis, and J. Zmuidzinas, "A broadband superconducting detector suitable for use in large arrays," *Nature*, vol. 425, no. 6960, pp. 817–821, Oct. 2003.

[23] E. Burstein, D. N. Langenberg, and B. N. Taylor, "Superconductors as quantum detectors for microwave and sub-millimeter-wave radiation," *Phys. Rev. Lett.*, vol. 6, pp. 92–94, Feb 1961.

[24] J. Glenn, P. A. R. Ade, M. Amarie, J. J. Bock, S. F. Edgington, A. Goldin, S. Golwala, D. Haig, A. E. Lange, G. Laurent, P. D. Mauskopf, M. Yun, and H. Nguyen, "Current status of Bolocam: a large-format millimeter-wave bolometer camera," in *Millimeter and Submillimeter Detectors for Astronomy*, ser. Society of Photo-Optical Instrumentation Engineers (SPIE) Conference Series, T. G. Phillips and J. Zmuidzinas, Eds., vol. 4855, Feb. 2003, pp. 30–40.

[25] E. Kreysa, H.-P. Gemünd, A. Raccanelli, L. A. Reichertz, and G. Siringo, "Bolometer arrays for Mm/Submm astronomy," in *Experimental Cosmology at Millimetre Wavelengths*, ser. American Institute of Physics Conference Series, M. de Petris and M. Gervasi, Eds., vol. 616, May 2002, pp. 262–269.

[26] W. Holland, M. MacIntosh, A. Fairley, D. Kelly, D. Montgomery, D. Gostick, E. Atad-Ettedgui, M. Ellis, I. Robson, M. Hollister, A. Woodcraft, P. Ade, I. Walker, K. Irwin, G. Hilton, W. Duncan, C. Reintsema, A. Walton, W. Parkes, C. Dunare, M. Fich, J. Kycia, M. Halpern, D. Scott, A. Gibb, J. Molnar, E. Chapin, D. Bintley, S. Craig, T. Chylek, T. Jenness, F. Economou, and G. Davis, "SCUBA-2: a 10,000-pixel submillimeter camera for the James Clerk Maxwell Telescope," in *Society of Photo-Optical Instrumentation Engineers (SPIE) Conference Series*, ser. Society of Photo-Optical Instrumentation Engineers (SPIE) Conference Series, vol. 6275, Jun. 2006, p. 1.

[27] A. Baryshev, J. A. Baselmans, S. J. C. Yates, L. Ferrari, L. Bisigello, R. M. J. Janssen, A. Endo, T. M. Klapwijk, B. Klein, S. Heyminck, and R. Gusten, "Large format antenna coupled micorwave kinetic iinductance detector arrays for radioastronomy," in *39th International Conference on Infrared, Millimeter, and THz Waves*, 2014.

[28] B. A. Mazin, "Microwave kinetic inductance detectors," Ph.D. dissertation, Califor-

nia Institute of Technology, United States, California, 2004.

[29] S. J. C. Yates, J. J. A. Baselmans, A. Endo, R. M. J. Janssen, L. Ferrari, P. Diener, and A. M. Baryshev, "Photon noise limited radiation detection with lens-antenna coupled microwave kinetic inductance detectors," *Applied Physics Letters*, vol. 99, no. 7, pp. –, 2011.

[30] A. Monfardini, A. Benoit, A. Bideaud, L. Swenson, A. Cruciani, P. Camus, C. Hoffmann, F. X. Désert, S. Doyle, P. Ade, P. Mauskopf, C. Tucker, M. Roesch, S. Leclercq, K. F. Schuster, A. Endo, A. Baryshev, J. J. A. Baselmans, L. Ferrari, S. J. C. Yates, O. Bourrion, J. Macias-Perez, C. Vescovi, M. Calvo, and C. Giordano, "A Dual-band Millimeter-wave Kinetic Inductance Camera for the IRAM 30 m Telescope," , vol. 194, p. 24, Jun. 2011.

[31] A. Baryshev, J. Baselmans, A. Freni, G. Gerini, H. Hoevers, A. Iacono, and A. Neto, "Progress in antenna coupled kinetic inductance detectors," *Terahertz Science and Technology, IEEE Transactions on*, vol. 1, no. 1, pp. 112–123, Sept 2011.

[32] A. Neto, N. Llombart, J. Baselmans, A. Baryshev, and S. Yates, "Demonstration of the leaky lens antenna at submillimeter wavelengths," *Terahertz Science and Technology, IEEE Transactions on*, vol. 4, no. 1, pp. 26–32, Jan 2014.

[33] A. Iacono, "Large focal plane arrays for thz imaging," Ph.D. dissertation, Eindhoven University of Technology, 2012.

[34] S. Doyle, P. Mauskopf, J. Naylon, A. Porch, and C. Duncombe, "Lumped element kinetic inductance detectors," *Journal of Low Temperature Physics*, vol. 151, no. 1-2, pp. 530–536, 2008.

[35] R. M. J. Janssen, J. J. A. Baselmans, A. Endo, L. Ferrari, S. J. C. Yates, A. M. Baryshev, and T. M. Klapwijk, "High optical efficiency and photon noise limited sensitivity of microwave kinetic inductance detectors using phase readout," *Applied Physics Letters*, vol. 103, no. 20, pp. –, 2013.

[36] C. M. McKenney, H. G. Leduc, L. J. Swenson, P. K. Day, B. H. Eom, and J. Zmuidzinas, "Design considerations for a background limited 350 micron pixel array using lumped element superconducting microresonators," in *SPIE, Millimeter, Submillimeter, and Far-Infrared Detectors and Instrumentation for Astronomy*, vol. 8452, 2012, pp. 84 520S–84 520S–10.

[37] B. Blazquez, N. Llombart, A. Neto, and J. Bueno, "Development of lens-coupled LEKID detectors arrays for THz radiation," in *Antennas and Propagation (EUCAP),*

2012 6th European Conference on, March 2012, pp. 3264–3267.

[38] S. Ahmed, A. Schiessl, and L. Schmidt, "Novel fully electronic active real-time millimeter-wave imaging system based on a planar multistatic sparse array," in *Microwave Symposium Digest (MTT), 2011 IEEE MTT-S International*, June 2011, pp. 1–4.

[39] A. Schiessl and S. Ahmed, "W-band imaging of explosive substances," in *Microwave Conference, 2009. EuMC 2009. European*, Sept 2009, pp. 1888–1891.

[40] D. Sheen, D. McMakin, and T. Hall, "Near field imaging at microwave and millimeter wave frequencies," in *Microwave Symposium, 2007. IEEE/MTT-S International*, June 2007, pp. 1693–1696.

[41] C. am Weg, W. von Spiegel, R. Henneberger, R. Zimmermann, T. Loeffler, and H. Roskos, "Fast active THz cameras with ranging capabilities," *Journal of Infrared, Millimeter, and Terahertz Waves*, vol. 30, no. 12, pp. 1281–1296, 2009.

[42] H. Quast and T. Loffler, "Towards real-time active thz range imaging for security applications," in *Electromagnetics in Advanced Applications, 2009. ICEAA '09. International Conference on*, Sept 2009, pp. 501–504.

[43] D. M. Sheen, T. E. Hall, R. H. Severtsen, D. L. McMakin, B. K. Hatchell, and P. L. J. Valdez, "Standoff concealed weapon detection using a 350-GHz radar imaging system," in *Society of Photo-Optical Instrumentation Engineers (SPIE) Conference Series*, vol. 7670, Apr. 2010, p. 8.

[44] K. Cooper, R. Dengler, N. Llombart, T. Bryllert, G. Chattopadhyay, E. Schlecht, J. Gill, C. Lee, A. Skalare, I. Mehdi, and P. Siegel, "Penetrating 3-d imaging at 4- and 25-m range using a submillimeter-wave radar," *Microwave Theory and Techniques, IEEE Transactions on*, vol. 56, no. 12, pp. 2771–2778, Dec 2008.

[45] N. Llombart, R. Dengler, and K. Cooper, "Terahertz antenna system for a near-video-rate radar imager [antenna applications]," *Antennas and Propagation Magazine, IEEE*, vol. 52, no. 5, pp. 251–259, Oct 2010.

[46] N. Llombart, K. Cooper, R. Dengler, T. Bryllert, G. Chattopadhyay, and P. Siegel, "Time-delay multiplexing of two beams in a terahertz imaging radar," *Microwave Theory and Techniques, IEEE Transactions on*, vol. 58, no. 7, pp. 1999–2007, July 2010.

[47] K. B. Cooper, T. A. Reck, C. Jung-Kubiak, C. Lee, J. V. Siles, R. H. Lin, A. Peralta, E. Decrossas, E. T. Schlecht, G. Chattopadhyay, and I. Mehdi, "Transceiver array

development for submillimeter-wave imaging radars," in *SPIE, Passive and Active Millimeter-Wave Imaging*, vol. 8715, 2013, pp. 87 150A–87 150A–8.

[48] K. Cooper and G. Chattopadhyay, "Submillimeter-wave radar: Solid-state system design and applications," *Microwave Magazine, IEEE*, vol. 15, no. 7, pp. 51–67, Nov 2014.

[49] P. F. Goldsmith, I. of Electrical, E. Engineers, M. Theory, and T. Society, *Quasioptical systems: Gaussian beam quasioptical propagation and applications*. IEEE press New York, 1998.

[50] J. Glenn, G. Chattopadhyay, S. F. Edgington, A. E. Lange, J. J. Bock, P. D. Mauskopf, and A. T. Lee, "Numerical optimization of integrating cavities for diffraction-limited millimeter-wave bolometer arrays," *Appl. Opt.*, vol. 41, no. 1, pp. 136–142, Jan 2002.

[51] T. Reck, J. Siles, C. Jung, J. Gill, C. Lee, G. Chattopadhyay, I. Mehdi, and K. Cooper, "Array technology for terahertz imaging," in *SPIE Defense, Security, and Sensing*. International Society for Optics and Photonics, 2012, pp. 836 202–836 202.

[52] W. Carter, "On refocusing a radio telescope to image sources in the near field of the antenna array," *Antennas and Propagation, IEEE Transactions on*, vol. 37, no. 3, pp. 314–319, Mar 1989.

[53] G. Mur, "A finite dilyerence method for the solution of electromagnetic waveguide discontinuity problems," *Microwave Theory and Techniques, IEEE Transactions on*, vol. 22, no. 1, pp. 54–57, Jan 1974.

[54] A. Taflove and S. Hagness, *Computational Electrodynamics: The Finite-difference Time-domain Method*, ser. Artech House antennas and propagation library. Artech House, 2005.

[55] D. Lynch and K. Paulsen, "Time-domain integration of the maxwell equations on finite elements," *Antennas and Propagation, IEEE Transactions on*, vol. 38, no. 12, pp. 1933–1942, Dec 1990.

[56] P. P. Silvester and R. L. Ferrari, *Finite Elements for Electrical Engineers*, 3rd ed. Cambridge University Press, 1996, cambridge Books Online.

[57] F. Teixeira, "Time-domain finite-difference and finite-element methods for maxwell equations in complex media," *Antennas and Propagation, IEEE Transactions on*, vol. 56, no. 8, pp. 2150–2166, Aug 2008.

[58] R. F. Harrington, *Field Computation by Moment Methods.* Wiley-IEEE Press, 1993.

[59] S. Rao, D. Wilton, and A. Glisson, "Electromagnetic scattering by surfaces of arbitrary shape," *Antennas and Propagation, IEEE Transactions on*, vol. 30, no. 3, pp. 409–418, May 1982.

[60] F. Vipiana, P. Pirinoli, and G. Vecchi, "A multiresolution method of moments for triangular meshes," *Antennas and Propagation, IEEE Transactions on*, vol. 53, no. 7, pp. 2247–2258, July 2005.

[61] F. Vipiana and G. Vecchi, "A novel, symmetrical solenoidal basis for the mom analysis of closed surfaces," *Antennas and Propagation, IEEE Transactions on*, vol. 57, no. 4, pp. 1294–1299, April 2009.

[62] C. Craeye, A. Tijhuis, and D. Schaubert, "An efficient mom formulation for finite-by-infinite arrays of two-dimensional antennas arranged in a three-dimensional structure," *Antennas and Propagation, IEEE Transactions on*, vol. 52, no. 1, pp. 271–282, Jan 2004.

[63] "Keysight Technologies, EEsof, Momentum," http://www.keysight.com/.

[64] "EMSS - EM Software & Systems Ltd, FEKO," https://www.feko.info/.

[65] "Ansoft Corporation, HFSS," http://www.ansoft.com.

[66] "CST - Computer Simulation Technology," http://www.cst.com.

[67] P. Pathak, "High frequency techniques for antenna analysis," *Proceedings of the IEEE*, vol. 80, no. 1, pp. 44–65, Jan 1992.

[68] M. Bass, C. DeCusatis, J. Enoch, V. Lakshminarayanan, G. Li, C. Macdonald, V. Mahajan, and E. Van Stryland, *Handbook of Optics. Volume I: Geometrical and Physical Optics, Polarized Light, Components and Instruments(Set). Third Edition*, 3rd ed. New York, NY, USA: McGraw-Hill, Inc., 2010.

[69] J. B. Keller, "Geometrical theory of diffraction," *J. Opt. Soc. Am.*, vol. 52, no. 2, pp. 116–130, Feb 1962.

[70] R. Hansen, *Geometric Theory of Diffraction*, ser. IEEE Press selected reprint series. John Wiley & Sons Australia, Limited, 1981.

[71] R. Kouyoumjian and P. Pathak, "A uniform geometrical theory of diffraction for an edge in a perfectly conducting surface," *Proceedings of the IEEE*, vol. 62, no. 11, pp. 1448–1461, Nov 1974.

[72] S.-W. Lee and G. A. Deschamps, "A uniform asymptotic theory of electromagnetic

diffraction by a curved wedge," *Antennas and Propagation, IEEE Transactions on*, vol. 24, no. 1, pp. 25–34, Jan 1976.

[73] P. Ufimtsev, "Method of edge waves in the physical theory of diffraction," *from Russian: Medthod Krayevykh voin v fizicheskoy teorii difraktsii, 1962. Translation prepared by the U.S. Air Force Foreign Technology Division, Wright-Patterson AFB, Ohio, Sept. 1971.*

[74] ——, *Fundamentals of the Physical Theory of Diffraction*. Wiley, 2007.

[75] "GRASP - TICRA," http://www.ticra.com/.

[76] B. Guenther, *Modern Optics*, ser. Wiley international edition. Wiley, 1990.

[77] H. Gross, *Handbook of Optical Systems, Aberration Theory and Correction of Optical Systems*, ser. Aberration theory and correction of optical systems. Wiley, 2007.

[78] "Radiant Zemax - Zemax," https://www.zemax.com.

[79] "LAMBDA Research Coorporation - OSLO," http://www.lambdares.com/oslo.

[80] "Synopsys Optical Solutions - CODE V," http://optics.synopsys.com/codev.

[81] "Breault Research - ASAP," http://www.breault.com/software/about-asap.

[82] "Synopsys Optical Solutions - LightTools," http://optics.synopsys.com/lighttools.

[83] "LAMBDA Research Coorporation - TracePro," http://www.lambdares.com/features.

[84] S. Maci, Z. Sipus, A. Freni, A. Mazzinghi, and S. Skokic, *Advanced Mathematics for Antenna Analysis*. Class notes for European School of Antennas Course, Dubrovnik, Croatia, May 14-19, 2012.

[85] A. Nagamune and P. Pathak, "An efficient plane wave spectral analysis to predict the focal region fields of parabolic reflector antennas for small and wide angle scanning," *Antennas and Propagation, IEEE Transactions on*, vol. 38, no. 11, pp. 1746–1756, Nov 1990.

[86] E. Wolf, "Electromagnetic diffraction in optical systems. I. an integral representation of the image field," *Proceedings of the Royal Society of London. Series A. Mathematical and Physical Sciences*, vol. 253, no. 1274, pp. 349–357, 1959.

[87] L. Ferrari, A. M. Baryshev, J. J. A. Baselmans, G. de Lange, P. Diener, J. W. Kooi, J. J. Lankwarden, and S. J. C. Yates, "Kinetic inductance detectors (KIDs) for the SAFARI instrument on SPICA," in *SPIE, Space Telescopes and Instrumentation 2010: Optical, Infrared, and Millimeter Wave*, vol. 7731, 2010, pp. 77 314H–77 314H–

9.

[88] W. S. Winfield, "Absorbent body for electromagnetic waves," US Navy Patent US2 599 944 A, Jun. 10, 1952, uS Patent 2,599,944.

[89] R. Fante and M. McCormack, "Reflection properties of the Salisbury screen," *Antennas and Propagation, IEEE Transactions on*, vol. 36, no. 10, pp. 1443–1454, Oct 1988.

[90] H. G. Leduc, B. Bumble, P. K. Day, B. H. Eom, J. Gao, S. Golwala, B. A. Mazin, S. McHugh, A. Merrill, D. C. Moore, O. Noroozian, A. D. Turner, and J. Zmuidzinas, "Titanium nitride films for ultrasensitive microresonator detectors," *Applied Physics Letters*, vol. 97, no. 10, pp. –, 2010.

[91] J. Baselmans, S. J. C. Yates, R. Barends, Y. J. Y. Lankwarden, J. R. Gao, H. Hoevers, and T. M. Klapwijk, "Noise and Sensitivity of Aluminum Kinetic Inductance Detectors for Sub-mm Astronomy," *Journal of Low Temperature Physics*, vol. 151, pp. 524–529, 2008.

[92] J. Bueno, P. C. J. J. Coumou, G. Zheng, P. J. de Visser, T. M. Klapwijk, E. F. C. Driessen, S. Doyle, and J. J. A. Baselmans, "Anomalous response of superconducting titanium nitride resonators to terahertz radiation," *Applied Physics Letters*, vol. 105, no. 19, pp. –, 2014.

[93] K. Rozanov, "Ultimate thickness to bandwidth ratio of radar absorbers," *Antennas and Propagation, IEEE Transactions on*, vol. 48, no. 8, pp. 1230–1234, Aug 2000.

[94] E. Knott and C. Lunden, "The two-sheet capacitive Jaumann absorber," *Antennas and Propagation, IEEE Transactions on*, vol. 43, no. 11, pp. 1339–1343, Nov 1995.

[95] B. A. Munk, *Frequency Selective Surfaces - Theory and Design.* Wiley, 2000.

[96] N. Engheta, "Thin absorbing screens using metamaterial surfaces," in *Antennas and Propagation Society International Symposium, 2002. IEEE*, vol. 2, 2002, pp. 392–395.

[97] D. J. Kern and D. H. Werner, "A genetic algorithm approach to the design of ultrathin electromagnetic bandgap absorbers," *Microwave and Optical Technology Letters*, vol. 38, no. 1, pp. 61–64, 2003.

[98] A. Zadeh and A. Karlsson, "Capacitive circuit method for fast and efficient design of wideband radar absorbers," *Antennas and Propagation, IEEE Transactions on*, vol. 57, no. 8, pp. 2307–2314, Aug 2009.

[99] F. Costa, A. Monorchio, and G. Manara, "Analysis and design of ultra thin electromagnetic absorbers comprising resistively loaded high impedance surfaces," *Antennas*

and Propagation, IEEE Transactions on, vol. 58, no. 5, pp. 1551–1558, May 2010.

[100] A. Monti, J. Soric, A. Alu, F. Bilotti, A. Toscano, and L. Vegni, "Overcoming mutual blockage between neighboring dipole antennas using a low-profile patterned metasurface," *Antennas and Wireless Propagation Letters, IEEE*, vol. 11, pp. 1414–1417, 2012.

[101] M. I. Kontorovich, V. P. Y. Petrunkin, N. A. Yesepkina, and M. I. Astrakhan, "The coefficient of reflection of a plane electromagnetic wave from a plane wire mesh," *Radio Engineering and Electronic Physics*, vol. 7, no. 2, pp. 222–231, 1962.

[102] V. Yatsenko, S. Tretyakov, S. Maslovski, and A. Sochava, "Higher order impedance boundary conditions for sparse wire grids," *Antennas and Propagation, IEEE Transactions on*, vol. 48, no. 5, pp. 720–727, May 2000.

[103] O. Luukkonen, C. Simovski, G. Granet, G. Goussetis, D. Lioubtchenko, A. Raisanen, and S. Tretyakov, "Simple and accurate analytical model of planar grids and high-impedance surfaces comprising metal strips or patches," *Antennas and Propagation, IEEE Transactions on*, vol. 56, no. 6, pp. 1624–1632, June 2008.

[104] M. I. Kontorovich, "Averaged boundary conditions at the surface of a grating with square mesh," *Radio Engineering and Electronic Physics*, vol. 8, no. 9, pp. 1446–1454, Sep 1963.

[105] Z. S. Agranovich, V. A. Marchenko, and V. P. Shestopalov, "Diffraction of a plane electromagnetic wave from plane metallic lattices," *Sov. Phys. Tech. Phys.*, vol. 7, pp. 277–286, 1962.

[106] F. Costa, A. Monorchio, and G. Manara, "Efficient analysis of frequency-selective surfaces by a simple equivalent-circuit model," *Antennas and Propagation Magazine, IEEE*, vol. 54, no. 4, pp. 35–48, Aug 2012.

[107] S. Maci, M. Caiazzo, A. Cucini, and M. Casaletti, "A pole-zero matching method for EBG surfaces composed of a dipole FSS printed on a grounded dielectric slab," *Antennas and Propagation, IEEE Transactions on*, vol. 53, no. 1, pp. 70–81, Jan 2005.

[108] S. A. Tretyakov and C. R. Simovski, "Dynamic model of artificial reactive impedance surfaces," *Journal of Electromagnetic Waves and Applications*, vol. 17, no. 1, pp. 131–145, 2003.

[109] M. Pasian, S. Monni, A. Neto, M. Ettorre, and G. Gerini, "Frequency selective surfaces for extended bandwidth backing reflector functions," *Antennas and Propa-*

gation, IEEE Transactions on, vol. 58, no. 1, pp. 43–50, Jan 2010.

[110] A. Kazemzadeh and A. Karlsson, "On the absorption mechanism of ultra thin absorbers," *Antennas and Propagation, IEEE Transactions on*, vol. 58, no. 10, pp. 3310–3315, Oct 2010.

[111] D. Cavallo, A. Neto, and G. Gerini, "Green's function based equivalent circuits for connected arrays in transmission and in reception," *Antennas and Propagation, IEEE Transactions on*, vol. 59, no. 5, pp. 1535–1545, May 2011.

[112] A. Neto, D. Cavallo, G. Gerini, and G. Toso, "Scanning performances of wideband connected arrays in the presence of a backing reflector," *Antennas and Propagation, IEEE Transactions on*, vol. 57, no. 10, pp. 3092–3102, Oct 2009.

[113] A. Neto and J. Lee, "Ultrawide-band properties of long slot arrays," *Antennas and Propagation, IEEE Transactions on*, vol. 54, no. 2, pp. 534–543, Feb 2006.

[114] A. Tennant and B. Chambers, "A single-layer tuneable microwave absorber using an active FSS," *Microwave and Wireless Components Letters, IEEE*, vol. 14, no. 1, pp. 46–47, Jan 2004.

[115] N. Marcuvitz, *Waveguide handbook*. Iet, 1951, no. 21.

[116] "Core science requirements for the european SPICA instrument," http://sci.esa.int/.

[117] L. Novotny and B. Hecht, *Principles of Nano-Optics*, 2nd ed. Cambridge University Press, 2012, cambridge Books Online.

[118] A. Brahm, S. Döring, A. Wilms, G. Notni, S. Nolte, and A. Tünnermann, "Laser-generated broadband antireflection structures for freeform silicon lenses at terahertz frequencies," *Appl. Opt.*, vol. 53, no. 13, pp. 2886–2891, May 2014.

[119] N. Llombart, K. Cooper, R. Dengler, T. Bryllert, and P. Siegel, "Confocal ellipsoidal reflector system for a mechanically scanned active terahertz imager," *Antennas and Propagation, IEEE Transactions on*, vol. 58, no. 6, pp. 1834–1841, June 2010.

[120] Y. Imaizumi, Y. Suzuki, Y. Kawakami, and K. Araki, "A study on an onboard ka-band phased-array-fed imaging reflector antenna," in *Antennas and Propagation Society International Symposium, 2002. IEEE*, vol. 4, 2002, pp. 144–147 vol.4.

[121] C. Dragone, "A first-order treatment of aberrations in Cassegrainian and Gregorian antennas," *IEEE Transactions on Antennas and Propagation*, vol. 30, pp. 331–339, May 1982.

[122] K. Cooper, N. Llombart, G. Chattopadhyay, B. Dengler, R. Cofield, C. Lee,

S. Filchenkov, and E. Koposova, “A grating-based circular polarization duplexer for submillimeter-wave transceivers,” *Microwave and Wireless Components Letters, IEEE*, vol. 22, no. 3, pp. 108–110, March 2012.

[123] Y. Lo, S. Lee, and S. Lee, *Antenna Handbook: Antenna Theory*, ser. Antenna Handbook. Springer, 1993.

[124] B. Blazquez and N. Llombart, “Study of range refocusing techniques for a terahertz imaging radar,” in *Infrared, Millimeter, and Terahertz Waves (IRMMW-THz), 2012 37th International Conference on*, Sept 2012, pp. 1–2.

[125] N. Llombart, B. Blazquez, K. Cooper, and R. Dengler, “Range refocusing in a terahertz imaging radar,” in *Microwave Integrated Circuits Conference (EuMIC), 2012 7th European*, Oct 2012, pp. 227–229.

List of Related Publications

Journal Contributions

J1. B. Blázquez, K.B. Cooper, and N. Llombart, "Time-Delay Multiplexing With Linear Arrays of THz Radar Transceivers," *IEEE Transactions on TeraHertz Science and Technology*, vol. 4, no. 2, pp. 232-239, Mar. 2014.

J2. N. Llombart, and B. Blázquez, "Refocusing a THz Imaging Radar: Implementation and Measurements," *IEEE Transactions on Antennas and Propagation*, vol. 62, no. 3, pp. 1529-1534, Mar. 2014.

J3. B. Blázquez, N. Llombart, D. Cavallo, A. Freni, and A. Neto "A rigorous equivalent network for linearly polarized THz absorbers," *IEEE Transactions on Antennas and Propagation*, vol. 62, no. 10, pp. 5077-5088, Oct. 2014.

J4. N. Llombart, B. Blázquez, A. Freni, and A. Neto "Fourier Optics for the Analysis of Distributed Absorbers under THz Focusing Systems," *IEEE Transactions on TeraHertz Science and Technology*, accepted for publication, 2015.

International Conference Contributions

C1. J. Bueno, B. Blázquez, A.G. Taboada, J.L. Costa-Kramer, and N. Llombart, "Progress in the development of lens coupled LEKIDs for submm and FIR astrophysics," *14th International Workshop on Low Temperature Detectors*, Heidelberg University, Heidelberg, Germany, Aug. 1-5, 2011.

C2. B. Blázquez, A. Neto, N. Llombart, and J. Bueno, "Electromagnetic analysis of lens coupled LEKID detectors for THz astronomical applications," *36th International Conference on Infrared, Millimeter and TeraHertz Waves (IRMMW-THz 2011)*, Houston, TX, USA, Oct. 2-7, 2011.

C3. B. Blázquez, N. Llombart, J. Bueno, and A. Neto, "Development of lens-coupled LEKID detectors arrays for THz radiation," *6th European Conference on Antennas and Propagation (EuCAP 2012)*, Prague, Czech Republic, Mar. 26-30, 2012.

C4. B. Blázquez, and N. Llombart, "Study of range refocusing techniques for a terahertz imaging radar," *37th International Conference on Infrared, Millimeter and TeraHertz Waves (IRMMW-THz 2012)*, Wollongong, Australia, Sep. 23-28, 2012.

C5. B. Blázquez, N. Llombart, and J. Bueno, "Theoretical study of the THz absorption efficiencies of antenna coupled and lumped element KIDs," *37th International Conference on Infrared, Millimeter and TeraHertz Waves (IRMMW-THz 2012)*, Wollongong, Australia, Sep. 23-28, 2012.

C6. M. Parra, I. Lorite, B. Blázquez, J.L.Costa-Kramer, N. Llombart, and J. Bueno, "Characterization of lens-coupled TiN LEKIDs at 215μm," *37th International Conference on Infrared, Millimeter and TeraHertz Waves (IRMMW-THz 2012)*, Wollongong, Australia, Sep. 23-28, 2012.

C7. N. Llombart, B. Blázquez, K. Cooper, and R.J. Dengler, "Range refocusing in a terahertz imaging radar," *6th European Microwave Week (EuMW 2012)*, Amsterdam, The Netherlands, Oct. 28 - Nov. 2, 2012.

C8. B. Blázquez, N. Llombart, and A. Neto, "Lens Coupled LEKIDs: Theoretical Characterization and Measurements," *7th European Conference on Antennas and Propagation (EuCAP 2013)*, Gothenburg, Sweden, Apr. 8-12, 2013.

C9. B. Blázquez, and N. Llombart, "Quasioptical Time-Delay Multiplexing of a Linear Array for a Terahertz Imaging Radar," *7th European Conference on Antennas and Propagation (EuCAP 2013)*, Gothenburg, Sweden, Apr. 8-12, 2013.

C10. A. Neto, N. Llombart, O. Yurduseven, B. Blázquez, and A. Freni, "On the Use of Antenna Engineering Tools for the Optimization of the Focal Plane Sampling in Direct Detection of Distributed Sources," *IEEE Antennas and Propagation Society International Symposium (APS 2013)*, Orlando, FL, USA, Jul. 7-13, 2013.

C11. B. Blázquez, N. Llombart, and A. Neto, "Theoretical Characterization And Measurements Of Lens-Coupled LEKIDs," *38th International Conference on Infrared, Millimeter and TeraHertz Waves (IRMMW-THz 2013)*, Mainz on the Rhine, Germany, Sep. 2-6, 2013.

C12. N. Llombart, B. Blázquez, O. Yurduseven, A. Freni, and A. Neto, "On the Optimization of the Imaging Speed in Broadband THz Focal Plane Arrays of Kinetic

Inductance Detectors," *38th International Conference on Infrared, Millimeter and TeraHertz Waves (IRMMW-THz 2013)*, Mainz on the Rhine, Germany, Sep. 2-6, 2013.

C13. B. Blázquez, A. Freni, N. Llombart, and A. Neto, "Distributed Power Absorbers in General Focusing Systems," *8th European Conference on Antennas and Propagation (EuCAP 2014)*, The Hague, The Netherlands, Apr. 6-11, 2014.

C14. A. Neto, N. Llombart, B. Blázquez, and A. Freni, "Imaging Speed of Antenna Coupled Kinetic Inductance Detectors in the SAFARI/SPICA Scenario," *8th European Conference on Antennas and Propagation (EuCAP 2014)*, The Hague, The Netherlands, Apr. 6-11, 2014.

C15. B. Blázquez, N. Llombart, A.Neto, and A. Freni, "Analytical Model for Distributed Power Absorbers under a Focusing System," *IEEE Antennas and Propagation Society International Symposium (APS 2014)*, Memphis, TN, USA, Jul. 6-11, 2014.

C16. A. Neto, N. Llombart, B. Blázquez, and A. Freni, "Impact of the Antenna Bandwidth in the Imaging Speed of Kinetic Inductance Detectors Focal Plane Arrays," *IEEE Antennas and Propagation Society International Symposium (APS 2014)*, Memphis, TN, USA, Jul. 6-11, 2014.

C17. N. Llombart, B. Blázquez, A. Freni, and A. Neto, "Coherent Fourier Optics for the Analysis of THz Antennas under Focusing Systems," *39th International Conference on Infrared, Millimeter and TeraHertz Waves (IRMMW-THz 2014)*, Tucson, AZ, USA, Sep. 14-19, 2014.

C18. N. Llombart, E. Gandini, B. Blázquez, A. Freni, and A. Neto, "Coherent Fourier Optics Representation of Focal Plane Fields," *9th European Conference on Antennas and Propagation (EuCAP 2015)*, Lisbon, Portugal, Apr. 12-17, 2015.

Acknowledgements

At this point, I would like to acknowledge the work, collaboration and friendship of many people during these four years, both in my working and personal life. Without them, this experience would not have been possible.

First of all, I would like to thank my promotor, Prof. Andrea Neto, head of the Terahertz Sensing Group at TU Delft, for kindly welcoming me on his team. It has been exciting working with him and experience the passion and enthusiasm he brings to his work as a researcher and educator.

The other person that has made this thesis possible is my daily supervisor and copromotor, Dr. Nuria Llombart Juan, currently associate professor at TU Delft. She gave me the opportunity to enter into this research world. Since the first time we met, at Universidad Complutense de Madrid, in Spain, she has had confidence on me. I would like to express my gratitude for all her time and patient with me during all these years. She is one of the most knowledgeable persons I have ever met and has always tried to teach me as much as possible about electromagnetism and antennas.

There has been other people whose collaboration has been fundamental to carry forward this work. I would like to thank Prof. Angelo Freni for his invaluable assistance in Chapters 2, 3 and 4 of this thesis. In this first part, there are also another two people whose collaboration has been very important: Dr. Juan Bueno from the Netherlands Institute for Space Research (SRON), thanks for all your time not only in the Netherlands, but also at Centro de Astrobiologia (CAB) in Madrid; and also thanks to Dr. Jochem Baselmans from SRON-TU Delft for his priceless discussions about the design of KIDs within the SPACEKIDs project and for being part of my PhD. committee. Regarding the second part of this thesis, I would like to specially thank Dr. Ken Cooper from the NASA Jet Propulsion Laboratory for allowing me to work on their THz Imaging Radar and providing me with the measurements of the quasioptical sub-systems that we designed, that are included on this thesis.

On a more personal side, I would like to express my gratitude to my colleagues at Universidad Complutense de Madrid, in Spain. Thank you to Javi, Fran, Darwin, Alfonso and specially to Alex, not just a colleague but a friend. It was great to spend those months there. I have really good moments with you all that will stay in my memory forever. *Gracias por esos grandes momentos en la Escuela de Óptica, me llevo recuerdos imborrables.*

One of the nice things of doing a PhD. in two different places, is the amount of people you meet. Therefore, I also want to thank my fellow colleagues at TU Delft: Waqas, Alessandro, Ozan, Erio, Giorgio, Danielle, Sven and Shahab. They are all great, specially my office mates with whom I had great time and were an important support in good moments, but specially in the bad ones. Thanks to Waqas for helping me with the PhD. defence process from the distance. Thank you all guys!.

Thanks to our invaluable secretary, Xandra Tober, she really makes things easier.

A special mention to Maria Alonso. We met in my first conference in Houston and, since then, she became a friend. She has been the most important support inside TU Delft for the last year of my PhD. *Tu apoyo ha sido fundamental y lo sabes. Gracias por todo.*

I am really grateful to all the people I have met in the Netherlands but specially those three girls from Bastiaansplein, 23, with who I have felt like at home: Emmakaki, Marokio and Monikaki. Thank you for being my family in the Netherlands.

I leave for the end the most important part on the personal side: my family. My mother Maria Jose, my father Juan Carlos and my sister Laura. Thank you for everything you have always given to me without asking anything in return. I am happy to know that every goal I reach makes you feel proud of me. I love you and we will always be together, no matter the physical distance. I want to give a warm thanks to my biggest fan, my hubby Raúl. It is exciting to be with you and I am really looking forward to start our American adventure after finally close this stage of our life, that has been difficult, but it was well worth the effort!

Dejo para el final la parte mas importante a la que agradecer en el ámbito personal: mi familia. Mi madre Maria Jose, mi padre Juan Carlos y mi hermana Laura. Gracias por todo lo que siempre me habéis dado sin pedir nada a cambio. Me hace feliz saber que cada meta que alcanzo os hace sentir orgullosos de mi. Os quiero y siempre estaremos juntos, no importa la distancia. Quiero agradecer de forma especial a mi recien estrenado marido, mi mayor fan, Raúl, por todos estos años juntos. Es apasionante estar a tu lado y estoy deseando comenzar nuestra aventura americana tras cerrar esta etapa de nuestras vidas

que ha sido dura pero que, sin duda, ha merecido la pena.